Electro-Acoustic Coupling in a Plasma Gas

Thesis

UNRESTRICTED

Electro-acoustic coupling in a plasma gas

Thesis submitted by

Yvonne Sutton B.Sc.

for the degree of

Doctor of Philosophy

September 2011

Department of Physical Sciences

Faculty of Science

The Open University

Milton Keynes

United Kingdom

MK7 6AA

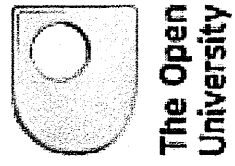

B&W
Bowers & Wilkins

Date of Submission: 30 September 2011
Date of Award: 30 January 2012

ProQuest LLC.
789 East Eisenhower Parkway
P.O. Box 1346
Ann Arbor, MI 48106 – 1346

Abstract

Sound emission using an ionised medium has been the subject of research since the beginning of the 20th century. The mechanism involves modulation at an audio frequency of an electrically sustained plasma discharge. In a similar effect to lightning, the charged particles in the plasma respond to the varying energy input. With this comes gas heating, molecular excitation, light emission from relaxation of excited molecular states and acoustic emission resulting from thermal expansion within, and external to, the discharge volume. Despite being the subject of research, there is scope for a deeper understanding of these kinetic processes within the plasma that transforms the input electrical energy into acoustic energy.

In this thesis, experimental measurements on an atmospheric pressure, radio frequency (RF) plasma are devised to explore the electro-acoustic mechanism that leads to sound generation. These measurement methods include: i) **nitrogen spectroscopy** for measurement of the species temperatures and emission intensities, ii) **optical imaging** of the visible emission for determining the discharge dimensions, iii) **schlieren imaging** for measuring the refractive index gradients within the discharge resulting from temperature and density variations and iv) **electrical characterisation** of the RF discharge. The work in this thesis builds on that reported previously by making direct measurements of the plasma itself to understand the dynamics of the plasma while under modulation. The work develops time-resolved measurement and non-invasive plasma diagnostic tehniques.

Under modulation the plasma behaves as a uniform sound emitter with the level of sound being dependent on the discharge size. A modulation of 15% on an rms conduction current produces a sound pressure level of approximately 67 dB at 3 kHz with around 4% distortion, based on an assessment of the harmonic content of the acoustic signal. In the steady-state , the RF plasma's electrical and optical characteristics show a close correlation to several equivalent DC plasmas and to the results calculated from an adapted model of a DC glow discharge. For an rms conduction current

range of 11-30 mA, the rotational temperature varies between 2800-3200 K; the vibrational temperature shows a change of 3500-4000 K with near equilibrium conditions to the rotational state occuring in the central region of the discharge. Spatial measurements identify the changes in the temperatures and dimensions along the vertical z-axis as well as the spatial dependence on the atomic and molecular species generated in the discharge. The widely acknowledged assumption of equilibrium between the rotational and translational states in nitrogen is challenged based on direct measurement of both parameters through spectrocopy and schlieren imaging. Similarly, the plasma dimensions provide contrasting behaviour depending on the spectral emission region used for measurement. Measurement of the discharge under modulation identifies the timescales for the various kinetic processes in the plasma; at 3 kHz the power leads the vibrational temperature by 34μs with a further delay of 70μs between vibrational and rotatational temperatures and relate to the timescales for electron-vibration excitation and vibrational-translational relaxation in nitrogen. The source of the acoustic emission due to modulation is identified (and seen) within the central ionised channel.

Contents

List of Figures

List of Tables

Nomenclature

The following nomenclature and terminology describes the parameters used in this thesis. Unless stated SI units have been used throughout.

RF - radio frequency

SPL - sound pressure level, dB

THD - total harmonic distortion

N_2FP - nitrogen first positive system

N_2SP - nitrogen second positive system

N_2^+FN - nitrogen first negative system

T_r - nitrogen rotational temperature, K

T_v - nitrogen vibrational temperature, K

T_g - translational or kinetic gas temperature, K

V-T - vibrational-translational

T-R - translational-rotational

V-R - vibrational-rotational

e-V - electron-vibrational

u_a - standard type A (random) uncertainty

u_b - standard type B (systematic) uncertainty

u_c - standard combined uncertainty

U - combined expanded uncertainty (subscript refers to measurement system)

n - refractive index

$(n-1)$ - fractional change in light velocity going from a gas to a vacuum

ε - deflection angle of light, mrad

a - image width

Uncertainties

The uncertainties expressed in this thesis are calculated from statistical variation of the measurements and from systematic evaluations of the measurement system. The type

B (systematic) uncertainty was derived from a combination of manufacturer's specifications, evaluation of the instrumentation and the methods used for data analysis. Unless stated, a rectangular probability distribution has been assumed with the combined, expanded uncertainty calculated to a 95 % confidence level [2]. Details of the systematic evaluation have been given in the appendices.

Acknowledgements

I would like to express my gratitude to my supervisors, Prof. Nicholas Braithwaite and Dr. David Sharp in all aspects of this work. Their patience, enthusiasm and encouragement was never lost on me. I also thank them for giving me the opportunity to be a student again! My gratitude extends to Dr. Gary Geaves at Bowers & Wilkins Group Ltd. for his support and enthusiasm in my work and for its funding.

I greatly appreciated the contributions of Dr. Peter Johnson and Prof. George Naidis for their guidance on the experimental and theoretical aspects of plasmas. Their involvement helped me take this research significantly further than I had expected and I thank them both for working with me on this project.

There are many people behind the scenes at the OU who have helped me along the way. They include Fraser Robertson and his colleagues in the Electronics Engineering Dept, Martin Percy and Roger Bence (retired) in the Physics workshop and Sandra Mills. I thank my colleagues in the Dept. of Physical Sciences especially Drs. Mark Bowden, Blagovest Bhanev and Vladimir Samara for their help in getting me up and running at the start of my research. My thanks also goes to Dr. Chris Barrett for his help with various side projects and for numerous scientific discussions. Also, to my office mates Bartlomiej Barc, Andrew Carter, Ros Hopwood and Aga Stypczynska and to Tracy Moore and the adminstrative staff in the department.

I acknowledge the contribution of Dr. Kari Niemi and Lucas Schaper of the Plasma Physics Group at Queen's University, Belfast for their assistance in the initial spectroscopic measurements and to Dr. Felipe Iza of Loughborough University for the loan of the Ocean Optics white light source used for calibration of the monochromator and Andor camera combination. Also, special thanks go to Jon Moore at Bowers & Wilkins Ltd. for our discussions on this work and for building a very fine Tesla coil for me to work with.

I thank the 20 housemates with whom I have lived in Padstow Palace, Fishermead and who have enriched my life enormously as well as providing me with plenty of holiday destinations for the future! I would especially like to thank Farah Huzair, Alex Borda and Hong Chen for their friendship and support during my time in MK. And not

forgetting old friends in Brighton especially Fiona Harrison, Simone and Nick Westoby, Lisa Dalglish and her family, Neil Gunner and Chrissy Smith for their continued friendship. Finally, thanks to Paul, Liz and Charlie and especially to my parents, David and Christa, for their love and support since $t_{ys} = 0$ s.

This thesis is dedicated to the memory of Claire Ashing (1973-2008)

'The day which we fear as our last is but the birthday of eternity' Seneca

'There are worse things in life than death. If you've ever spent an evening with an insurance salesman, you know what I'm talking about' Woody Allen

Chapter 1

Introduction

1.1 Plasma acoustics

This project investigates the electro-acoustic coupling mechanism by which an atmospheric pressure plasma generates sound. An electro-acoustic coupling mechanism is most familiar in the form of a hi-fi loudspeaker where audio frequency current through a coil oscillates a cone attached to a magnet. The oscillations cause displacement of the air at the cone with the resulting pressure variations propagating away from the source as sound. The same effect can be achieved if the mechanical system is replaced with an ionised gas. The charged particles within the plasma readily respond to electrical modulation and, through a process of energy transfer to the surrounding air molecules via a number of mechanisms within the plasma, pressure waves can be generated. This thesis explores some of the details.

There are two acknowledged mechanisms by which a plasma can be made to produce sound. The first relies on the transfer of momentum from charged particles to neutral gas molecules during collisions between the two and is commonly referred to as a *forcing* mechanism. An example of a point-to-plane DC corona discharge can be used to explain this effect. This configuration uses two electrodes, one a point electrode where the driving potential is applied and the other a plane metal surface which is grounded. When a DC potential is applied to the point electrode, a region of high ionisation is generated from which charged particles are emitted. Depending on the electrode bias, positive or negative charged particles are accelerated along the electric field towards

the grounded plane. In the *drift* region that lies between the point and plane, the charged components are accelerated and collisions occurs between charged species and neutral gas component. The heavier ion species are dominant in this mechanism; the near equivalence of their mass to the mass of the neutral species provides the most efficient means of energy transfer through elastic collision. Applying modulation to the electric field causes the charged species to follow the variation, gaining energy which is subsequently transferred to the neutral particles. The forcing effect that results is akin to the front face of a mechanical loudspeaker cone, with pressure fluctuations resulting from forcing the air. This has been described in literature as an 'ionic wind' and the effect has been the most investigated, usually through the use of corona or DC glow sources [3, 4, 5, 6]. Although these will be referenced further in the literature review, it is the second mechanism that is most relevant to this project.

In the second mechanism, commonly known as the *thermal* mechanism, the pressure fluctuations are caused by expansion within an ionised column. As with a lightning strike, the charged species transfer energy to neutral gas components through elastic collisions and through inelastic collisions via excitation of internal energy states (where the neutral components are molecular). The rapid heating in the ionised column results in thermal expansion, where the dimensions of the plasma expand and contract as the charged species respond to the applied modulating electric field. This leads to pressure variations within and external to the column. For this mechanism, adiabatic conditions within the column are required as the rate of energy transfer relative to the conduction of heat out of the system is critical in establishing pressure variations; this will be discussed in more detail later in this thesis.

The pressure variation generated through the mechanisms described above can be expressed using the ideal gas law as follows,

$$\Delta P = \Delta n_g k T_g + n_g k \Delta T_g \tag{1.1}$$

where ΔP is the change in pressure, ΔT_{g}, T_{g} are the changing and steady-state gas temperature, k is Boltzmann's constant and $n_{\mathrm{g}} = N/V$ is the number density where N is the particle number and V is the gas volume. The first term describes an isother-

mal system where localised density variations result from the ion collisions and are accompanied by a negligible change in gas temperature or gas volume; this reflects the behaviour of the forcing mechanism. For the adiabatic system that is described by the second term, the pressure variation results from the changing gas temperature that occurs as a result of collisions between the high energy electrons and neutral gas components. The energy transfer results in gas heating and, while volumetric changes are present, the variation in the temperature is the dominant effect in producing the pressure variations.

There are several advantages to using direct electro-acoustic coupling via a plasma. Mechanical loudspeakers are strongly directional, particularly at higher audio frequencies, and the transfer of mechanical energy to acoustic energy is generally inefficient, mainly due to the poor impedance matching between cone and air. In addition, the natural resonance of the cone structure causes certain frequencies to be optimised at the expense of others and so a desired broadband, flat-frequency response using a single emitter is difficult to achieve. In theory, the use of a plasma source can overcome many of these restrictions. Due to its negligible mass, the plasma responds quickly to changing electric fields and is able to reproduce a desired broadband response while faithfully reproducing an input electrical signal. This chapter gives an overview of plasma acoustics from initial investigation to commercial realisation and attempts to put a theoretical basis to experimental results. The origins are presented and an overview of research into plasma loudspeakers is reviewed. Based on the conclusions, the arguments for the research in this project will are given.

1.2 Literature review

In this section, the history of plasma acoustics is presented. This area of research dates back to the end of the 19th century and follows through to the present day where plasma tweeter speakers are commercially available. The key developments over this period are reviewed and discussed.

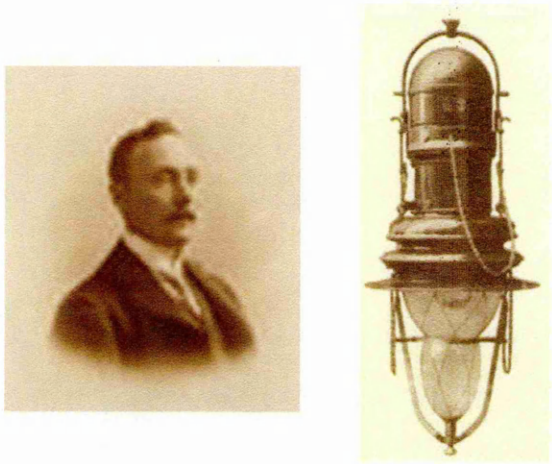

Figure 1.1: William Duddell and an arc lamp.

1.2.1 Initial investigations

The first investigations into plasma acoustics followed the best traditions of experimental physics in that they were concerned with trying to find a solution to a problem. During the Victorian period, arc lamps sat alongside gas lamps and the earliest electric lighting systems as a form of street lighting. Operating on the same principle as the welding arc, two electrodes were connected to a battery or generator and brought initially in contact. With a very small separation, the low voltage applied across them initiated the breakdown of air required for arc formation. The electrodes were then drawn further apart by a few millimetres to form an extended light source that was sustained by the current flowing through it. Quick depletion of the battery, erosion of the electrodes and arc instability were a few of the problems associated with this form of lighting. Another side-effect was the constant humming that accompanied its operation.

An investigation of the hum was carried out in around 1899 by William Duddell, a British electrical engineer and inventor (figure 1.1) whose inventions included an oscillograph that could record time-varying waveforms and a thermo-galvanometer for measuring low currents [7, 8]. In his experimental set-up, he applied time-varying voltages to the arc lamp and observed that a change in the frequency of the voltage resulted in a variation in the audible frequency of the hum. Duddell extended his investigation by attaching a keyboard with external resonant circuitry that applied specific frequen-

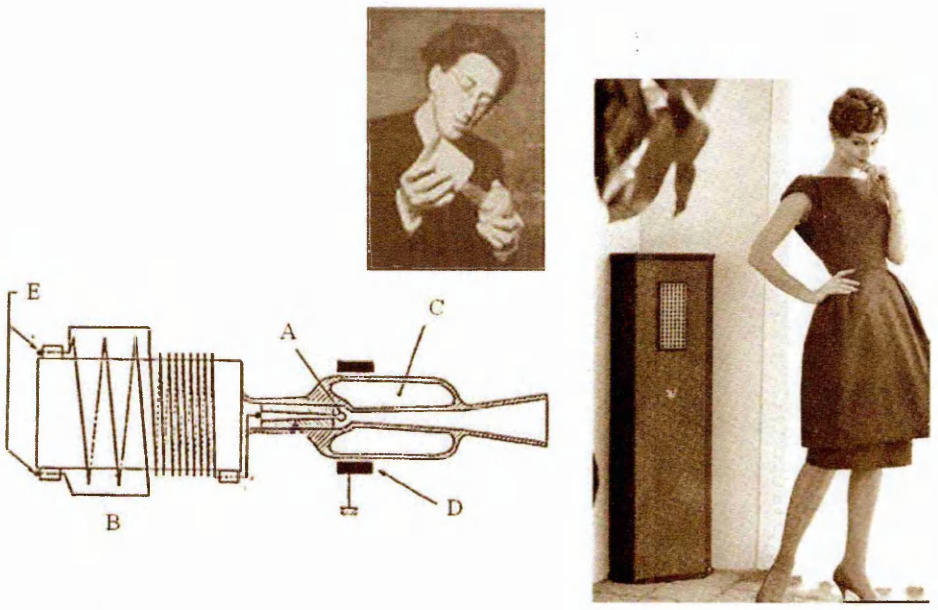

Figure 1.2: Sigfried Klein with a cross-section of the Ionophone (left) and mounted in a cabinet (right).

cies to the discharge, leading to the invention of the 'singing arc'. Duddell exhibited the singing arc at gatherings and exhibitions and a report of his work was published in Nature [9]. At one such exhibition, when modulation was applied to the arc, the lamps that were operated on the same ring circuit in the auditorium also modulated and emitted sound. Therefore, it could be argued that Duddell was a pioneer of surround sound.

Despite its appeal, Duddell never pursued any formal commercialisation of the device and little known research or development was undertaken in the years immediately after. It is likely that, as plasma physics was in its infancy around this time, the necessary diagnostics required to gain a basic understanding of the sound generation mechanism were not available thereby hindering further innovation.

1.2.2 Commercial realisation

The commercial potential was seen by French engineer Siegfried Klein who picked up the research on plasma acoustics in the mid-1940s [10, 11]. His work led to the production of the *Ionophone* (in conjunction with DuKane Inc), the first commercially available plasma loudspeaker (figure 1.2), in around 1954. Although the type of dis-

charge is not specifically named, it is essentially a corona discharge operated in air and utilises the forcing mechanism to generate sound. A spherical, platinum driving electrode is positioned at the entrance of a horn (A) and is driven with an RF voltage applied through a transformer (B). This driving electrode is mounted in a quartz insulator that in turn is surrounded by a grounded housing (C) that acts as the second electrode (D). The electrode requires a voltage of around 700 V to form a region of high ionisation. When the voltage is modulated (E), pressure variations occur from collisions between the charged species and neutral molecules.

With the Ionophone, Klein made the association between the charged particles and their role in sound generation. Although this was only presented from an experimental point of view (i.e. no real analytical explanation is given regarding the interactions of the discharge components), the investigations extended to predicting the relationships between the modulating voltage, current, temperature and pressure. Klein also acknowledged one of the main limitations of plasma loudspeakers. While the frequency response of the Ionophone was on a par or superior to that of a mechanical loudspeaker at the high frequency end, the low frequency operation was poor, which Klein attributed to the size of the plasma itself. Hence, the mechanical adaptation of lengthening the housing which, in combination with the horn structure, extended the low frequency limit to around 200 Hz; this will be returned to in the next chapter. The high frequency response was reported to extend to 3 MHz though only the results for the response up to 20 kHz were presented.

The developments beyond this initial design are sketchy but it is known that Klein continued his work in plasma loudspeakers and filed further patents for plasma tweeter speakers up to 1984 [12, 13, 14]. For information, the Ionophone was also marketed outside of the USA under the names of Ionovac and Ionofane [15].

1.2.3 Recent developments

Since the Ionophone, the production and development of plasma sound sources have been limited and those that are available tend to be confined to more specialist markets. For example, the *Plasmatronic* invented by Hill [16] is a large volume, multi-element

source sustained in helium where sound generation occurs through temperature modulation of the source. The use of helium significantly reduces ozone generation, which is common in colder, corona-type discharges. However, there are significant practical problems associated with the helium usage as well as large cost implications. Finally, the T1WS tweeter is currently available from Acapella [17]. There is little information regarding the type of discharge but the product specification suggests an ion source, similar in operation to the Ionophone.

1.2.4 Experimental aspects

The paper of Bastien [18] reviews much of the work regarding acoustics in gas discharges up to its publication in 1987. The key points of this review are presented here and put into the context of this project. Also, the research carried out in the field since 1987 are reviewed. The main discussions revolve around the performance of a plasma as a sound emitter, the factors that affect the sound quality and the analytical methods used to describe the discharge behaviour. Reference is made throughout to the *sound pressure level* (SPL) which is a measure of the level of sound from a source and a detailed description is given of this in section 2.4.1.

As stated previously, there has been little innovation in the experimental configuration of plasma sources used for sound production since the Ionophone. The majority of research has been carried out on corona-type discharges, sustained with both DC or RF voltages [3, 4, 6, 19, 20, 21, 22, 23]. A DC glow discharge has also been investigated [5, 24] and flame sources, where the charged component is generated through combustion of a seed chemical, have also been researched although not in recent years [25, 26, 27]; aspects of the mechanisms involved in flame sources are still useful in the context of an electrically sustained discharge and hence reference is still made to them in this section. As will be described in Chapter 3, the plasma under investigation in this project is an arc-type plasma where the highly collisional nature and high degree of ionisation mean that thermal mechanism is assumed to be dominant. This provides a different set of conditions from that of the colder plasmas investigated previously and

requires initial measurement of the acoustic characteristics to determine the plasma's capability as a sound source.

It is difficult to compare the acoustic characteristics of the other plasma sources reported previously. This is mainly due to inconsistencies in their modulation settings and differences in the experimental configurations, making 'scaling' to an equivalent plasma condition unreliable. However, the low frequency drop-off (as experienced in Klein's Ionophone) is a common effect. Through the use of helium and argon as the source gas, Mazzolla [5] found that the frequency range could be manipulated. Use of gases other than air would not affect the modulation frequency but, in an adiabiatic system such as the DC glow, the rate of thermal diffusion determines the containment of heat within a system. The higher diffusivity of helium means that heat will be more easily conducted away from the gas in comparison with argon which has a lower diffusivity. The resulting frequency response shows that the cut-off frequency for argon can be extended to 10 kHz lower than in helium. Mention was made previously of the inconvenience and expense of using non-air gas feeds but this configuration may find a use in more specialist applications or controlled environments.

Manipulation of sound emission levels was also explored mechanically by Ackerman [20] who, like Klein, used a horn in combination with a small corona discharge to increase the sound level. This produced a high SPL of 132 dB over 10-40 kHz though details of the source dimensions are absent. The lowest was the corona discharge of Bequin [6] which emitted a barely audible 33 dB (@ 3 kHz) at 0.1 m; for reference, the SPL from a TV at average volume form a distance of 1 m is around 55-60 dB. Generating a larger volume source also increases the SPL as demonstrated by Burchard [26]. In Burchard's system, the charged particles are thermally generated from a source of readily ionisable potassium nitrate fed into an oxygen/acetylene flame. This method proved effective as a sound source with a controllable, high sound emission level of up to 40 kHz measured. Burchard's example of a 15 mm flame and a 10 mm electrode separation extends the low frequency response down to 1 kHz. Below 1 kHz, the frequency response drops off rapidly but modulation can still be detected through the variation of the optical emission. When plotted, the frequency response shows an increase in

the SPL with frequency from the modulating flame but it is shown that varying the flame size, AC/DC potentials and the flame impedance, also affects the SPL (though it is unclear in Burchard's analysis about the relative contribution of each independent variable). The supporting theory, however, provides the first concise analysis of the energy transfer mechanism. This describes the effect on the charged particles from the time-varying electric field and its relation to the emitted acoustic field.

The dependence of the sound generation on the plasma size can be seen (but is not discussed explicitly) in Bequin et al [6]. Measurements of a multiple element source constructed from 55 ballasted electrodes are presented. Unlike a single needle electrode configuration, which produces a barely audible sound emission, the use of multiple ballast needles acts like a circular piston with the emissions from each individual source summed to produce a greater acoustic level. A change in the electrode separation from 3 mm to 8 mm produces an approximate 6 dB increase between 500 Hz - 2 kHz. It is likely that changing the electrode separation in this corona discharge leads to an increase in the drift region and a subsequent increase in particle collisions.

While the low frequency drop-off is seen in all the plasma sources where the frequency response has been presented, it is reported that the response at high frequencies is very good. Ultrasonic frequency emission (here defined as greater than 20 kHz) is reported initially by Klein and also measured from a corona source by Lim [4]. The frequency range extends to 100 kHz but the previously uniform radial response of the plasma is badly perturbed as a result of diffraction around the electrode structure. For a flame discharge, a measurable acoustic output has been reported up to 840 kHz (though no results presented) [26].

There has been limited reporting in the literature regarding the 'quality' of the sound emission. Quality in this case is defined as the acoustic emission measured at frequencies other than those that would be expected from the input modulating signal. Harmonic distortion (the generation of harmonics in the acoustic signal) is one metric of quality and is measured by finding the amplitudes of the harmonic components relative to the fundamental (section 2.5.2). In a conventional loudspeaker, harmonic distortion occurs due to a non-linear response of the driving system or if the loudspeaker is driven

to produce a large amplitude oscillation, causing a non-linear relationship between the driving force and the displacement of the driving surface. For a plasma it is advantageous when trying to obtain a faithful reproduction of the input electrical signal, to find the limits of non-linear behaviour. For several plasma sources the modulation depths, calculated relative to the steady state current, have been reported as ranging from around 0.03 to 0.50 [6, 21], although no specific measurements of acoustic distortion are presented. A limit of modulation depth to avoid distortion is mentioned briefly by Ackerman [20] where the amplitude relative to the direct current amplitude is recommended to be restricted to 25% and preferably less than 10% to minimise distortion levels. It is unclear if this limit scales with increasing direct current levels (i.e. would 5 mA AC modulation on 50 mA direct current give the same distortion level as 1 mA AC modulation on 10 mA direct current?). That said, Fransson et al [24], in studying a glow discharge, found the harmonic distortion to be largely dependent on the modulation degree, expressed as the ratio of the modulating current amplitude to the direct current. A 10% modulation depth produces acceptable levels of distortion whereas increasing to a 50% modulation depth seriously impacts on the sound quality.

Without modulation, corona discharges are known to be sources of ambient noise or hissing which results from instabilities in the charge flow. Bequin [6] found that the electrode polarity has a strong effect on this with a negative point-to-plane configuration being optimal. Other methods for further reducing this effect include mechanical adaptations such as using sharper electrodes and precise alignment in the case of point-to-point configurations [3].

1.2.5 Theoretical analysis

The work of Duddell and Klein investigated the sound generation mechanism through experimentation though this lacked the analysis to account for the role of the plasma components during modulation. With the assumption of an adiabatic system, several theoretical approaches have been presented to describe the relationships between charged particles, temperature and pressure fluctuations. A common approach treats the plasma thermodynamically, relating the energy inputs and dissipation to sound gen-

eration. The approach of Ackerman [20] defines a simple energy balance relationship where the energy input to a corona discharge is RI^2, where R is the effective corona resistance and I is the modulating current. Energy dissipation is defined as the rate of heat transfer from the discharge to the surrounding ambient air and the expression for it includes variables for the plasma size and a rate constant for discharge cooling, though the source of this term is unclear. The final derivation calculates a proportional relationship between acoustic pressure and the discharge temperature variation. The equation gives a global approximation to the acoustic pressure as verified through experiment (though not presented in Ackerman's paper) and identifies the temperature variation as key to sound production. But there is no detail provided regarding the specific processes within the plasma that result in the temperature variation itself.

A detailed analytical derivation that links the sound generation mechanisms to varying pressure was presented by Ingard [28] and has formed the basis of many of the studies since [6, 22, 26, 27]. Based around the wave equation for pressure variation, it incorporates both sound generation mechanisms within the inhomogeneous term,

$$\nabla^2 p - \frac{1}{c^2}\frac{\partial^2 p}{\partial t^2} = \frac{(\gamma - 1)}{c}\frac{\partial H}{\partial t} - \mathrm{div} F \tag{1.2}$$

where H is the rate of energy transfer, F is the forcing term that can be used for the momentum exchange, γ is the adiabatic term and c is the speed of sound; these source terms are derived from linearised equations for conservation of energy, momentum and motion. This approach appears to work well as the source terms can be adapted to reflect the dominant processes within a specific discharge. In an example of Ingard, the thermal term in an equation that describes a weakly ionised plasma is calculated by considering the heating of neutral gas molecules through elastic collisions by electrons with the relationship between the rate of energy transfer and electrons expressed as,

$$H = (\frac{4m_e}{m_n})(\frac{m_e v_e^2}{2}) n_e n_n(\sigma) \tag{1.3}$$

where v_e is the electron velocity, m is the particle mass, n is the number density with the subscripts, e and n, being electrons and neutral respectively. While this

provides the first direct link between the plasma process and pressure variation, the proportional relationship between the rate of energy transfer, H, and the electron density, n_e (hence conduction current) implies that a discharge does not follow the expected power relationship, $H = I^2R$ where R is a resistance, in this case, across the discharge. While not discussed explicitly, this implies that the discharge region exhibits non-linear relationship between the equivalent electrical parameters.

Another example in Burchard [26] utilises only the thermal term in the analysis of a flame speaker, taking the energy input from joule heating. No SPL results are presented in Ingard but Burchard's comparison of the modelled and measured SPL results shows a reasonable correlation, though a large spread in the measured results occurs due to difficulties in obtaining accurate acoustic measurements. Although this analysis has been applied to weakly ionised media, further adaptations exist for the modelling of a highly ionised (thermal) plasma [29]. While equation 1.2 provides a direct relationship between the charged components and acoustic pressure this is still achieved only on a global level. The analysis assumes uniformity within the discharge volume whereas in reality the plasma will be non-uniform in nature, with sheath regions, volume variations and non-uniform response over the length of the plasma to the applied electric field. The acoustic pressure will be dependent on the dimensions of the source; it is possible that the non-uniform nature of a plasma may produce a number of source regions leading to interference effects and subsequent variations in the acoustic field structure.

Spatial variations of the plasma parameters (specifically gas temperature) were discussed by Mazzolla [5]. The analysis returns to a direct pressure and temperature variation (as with the Ackerman approach) though based around the ideal gas law. A temperature decay constant, τ, determines when the DC glow discharge turns from non-adiabatic to adiabatic conditions and when the acoustic emission starts. The heat transfer out of the column is dependent on the temperature gradient between the source and the ambient air and will influence the time constant. The spatial variation of temperature within the plasma means the temperature gradients will vary, as will the time constant that determines the onset of adiabatic conditions. This implies that multiple emission sources will be present in the plasma with individual frequency

bandwidths but, when summed together, these form a continuous broadband source.

The approach of Bequin [6, 22] defines two distinct regions for a point-to-plane negative corona discharge, with a region of high ionisation around the needle and a drift region between the needle and plane. In Bequin's formulation, the thermal term used to model the ionisation region, is similar to that of Burchard in that it uses electrical characteristics to define the power per unit volume dissipated by joule heating. The forcing term, used to model the interactions in the drift region, utilises the negative ion and electron currents. However, in solving the equations some of the parameters used in the analysis, such as the negative ion current and the potentials in the ionised region, are unable to be determined from reference values or from measurement. Therefore to determine their values, it is necessary to carry out a fitting between the modelled acoustic field and measurements, which loses the independent evaluation that a model should offer.

1.3 Summary and research question

To summarise, the published literature to date has progressed from initial experimentation to establishing that sound generation occurs through the interactions between the charged particles and neutral gas molecules. The theoretical analysis of these interactions provided good correlation with the predicted pressure levels where a comparison with the measured results was presented. The majority of the studies have focussed on the colder, corona-type discharges which are weakly ionised whereas the plasma used in this project is a warmer, arc-type plasma. As such the acoustic characteristics, in terms of such factors as frequency response, distortion and size dependency, need to be determined.

In a highly ionised discharge that exhibits arc-like behaviour, it is the thermal mechanism that dominates during sound emission. The adiabatic process, that is the basis for the thermal mechanism, would see a change in gas temperature directly resulting from the energy into the system. The results from previous experiments show electrical and acoustic measurements but no direct measurements of the plasma parameters have been completed. The ability to see how the gas temperature and other parameters vary,

both temporally and spatially, would provide direct evidence of the plasma's behaviour under modulation which in turn would give further insight into the electro-acoustic coupling.

The experimental aspects and theoretical analysis discussed in the existing studies examine the mechanism on a macroscopic level and neglect the spatial dependence of the plasma, where different regions may lead to different responses to a time-varying electric field. The energy input into the plasma is described in terms of power variation using the electron density and electrical characteristics. However, the analysis does not discuss all the energy transfer paths that can eventually lead to heating of the neutral gas molecules. As well as the joule heating and elastic collisions between electrons and neutral gas molecules, the use of molecular gases will result in a broader range of internal energy (rotational, vibrational) states being part of the energy transfer mechanism. Understanding the influence of these mechanisms would aid future innovation as well as the fundamental understanding of the plasma's behaviour under modulation.

1.4 Thesis plan

This thesis takes an experimental approach to answering the research question presented above. Several non-invasive diagnostic techniques are developed and validated in order to measure the characteristics of an atmospheric pressure, RF plasma which is sustained in air. These methods utilise the electrical characteristics and optical emission from the plasma with measurements made through methods such as spectroscopy and schlieren imaging to identify the plasma characteristics of interest. In conjunction with experiment, a numerical model (adapted from that used to model an atmospheric DC glow discharge) is introduced and validated in order to provide further understanding of the plasma behaviour down to the molecular level. The limitations of a plasma as an acoustic source are discussed and the possibilities for future research and development of acoustics in a plasma discharge are presented.

Chapter 2

Acoustic characteristics

2.1 Introduction

The previous chapter gave a general introduction to the history of plasma acoustics and the plasma sources that have been the subject of research so far. To complement this, the plasma used for this project is introduced in this chapter. A comprehensive study and discussion of the key characteristics of the plasma will be given in later chapters but, to give a feel for its capabilities as a sound source, the acoustic and the fundamental electrical characteristics will be presented here. In this way, the basic concepts of the electro-acoustic coupling can be appreciated.

2.2 The plasma

The plasma under investigation here is generated in air at atmospheric pressure using a solid state Tesla coil [30]. The solid state design is based on an inverter circuit using four MOSFET power transistors in an H-bridge configuration (figure 2.1). The control stage provides a logic signal (A) that alternately switches the transistors in the power stage and 'chops' the input DC voltage from a standard laboratory supply (B). The inductor, L, prevents damage to the DC supply from the back emf of the Tesla coil. The output signal from the inverter circuit is a low voltage/high current square wave which is sent to the primary coil. The voltage amplitude at this point is equal to the dc input voltage level (C). At the primary coil, the resonant nature of the circuit acts as

a filter, transforming the fundamental frequency of the square wave to the secondary coil and generating a high voltage between the electrodes (D).

An increase from the DC power supply corresponds to an increase in the power dissipated in the plasma. The resonant frequency of the coil is around 325 kHz and is determined by the inductances and capacitance of the coils (L_p, L_s, C_s). Operation at this frequency is beneficial as it lies in a RF region where the breakdown voltage of an air plasma is at its lowest [31]. The overall height of the Tesla coil including the frame is approximately 0.6 m. The primary coil is constructed from 18 turns of 3 mm diameter copper wire with an overall diameter of 107 mm. The secondary coil is constructed from 1250 turns of 0.24 mm diameter copper wire wound on a plastic tube and has an overall diameter of 84 mm. The heights of the coils are 100 mm and 330 mm respectively. The electrodes are milled from brass and secured into two 150 mm diameter dome structures, also made of brass. The driving electrode sits on top of the secondary coil with the top grounded electrode connected to a threaded screw that is adjustable over a 50 mm range. The resolution for adjustment of the top electrode is approximately 0.1 mm. Upon ignition, the discharge is rooted to the electrodes by visible hot spots, producing a flame-like luminous region some 3 to 5 mm in diameter which is stable and silent in ambient air.

2.3 Electrical properties of the plasma

The electrical properties of the plasma are critical with regard to their role in the various reaction processes required to sustain the plasma. In this section, a description of how these properties are measured is provided. In addition, the method of modulating the amplitude of the current (required for sound generation) is described.

2.3.1 Steady-state conduction current

The voltage across the plasma is measured using a Tektronix 6015A high voltage probe. For reference, a voltage of around 25 kV_{p-p} is required across the 15 mm electrode separation to initiate breakdown whereupon the plasma is sustained with a voltage of between 4-5 kV_{p-p}.

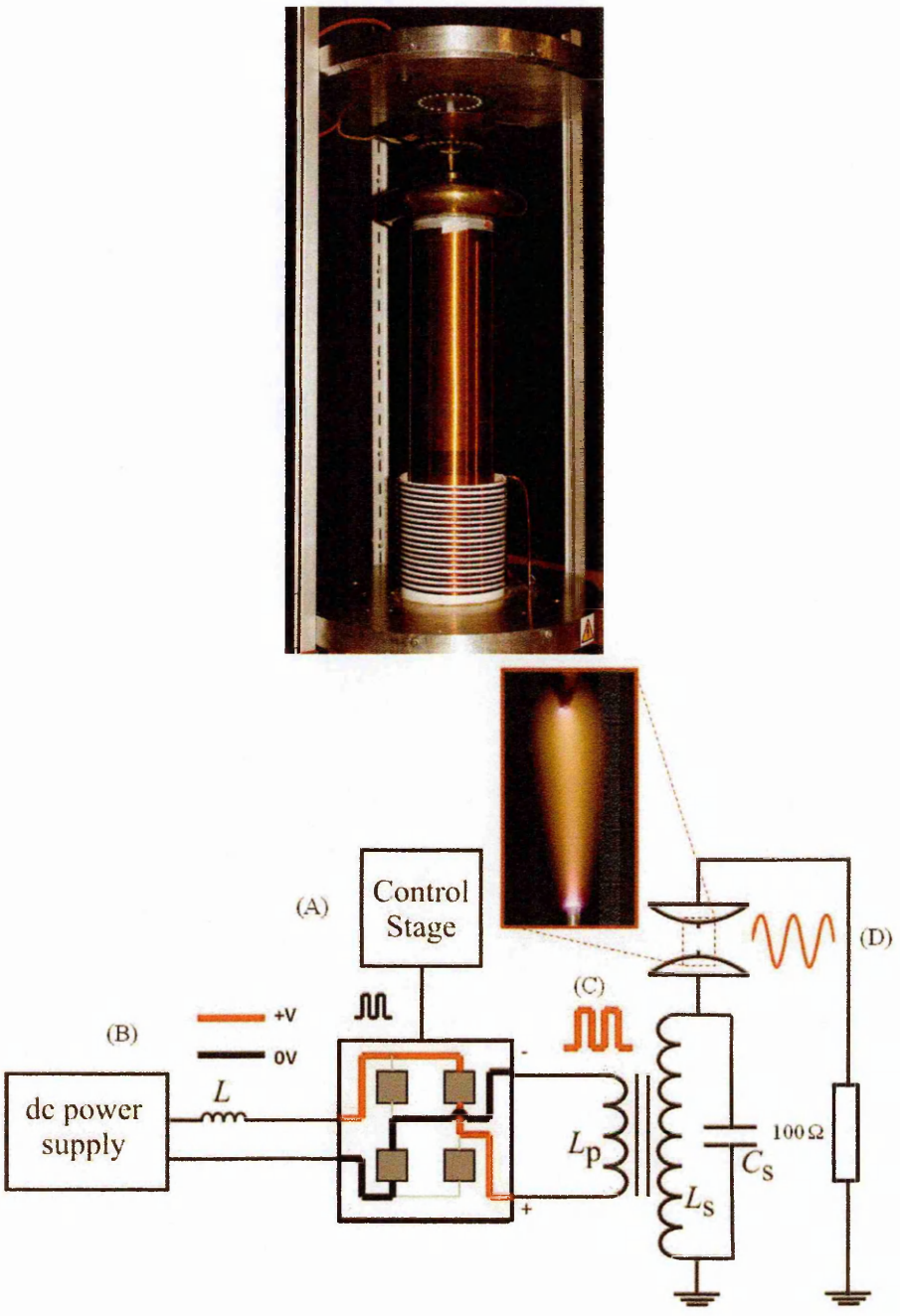

Figure 2.1: The Tesla coil (top) and the schematic diagram of its driving circuit (bottom) with the plasma ignited (inset). Calculations based on the coil dimensions and electrical characteristics estimate the component values at $L_p = 24$ μH, $L_s = 28$ mH, $C_s = 5$ pF.

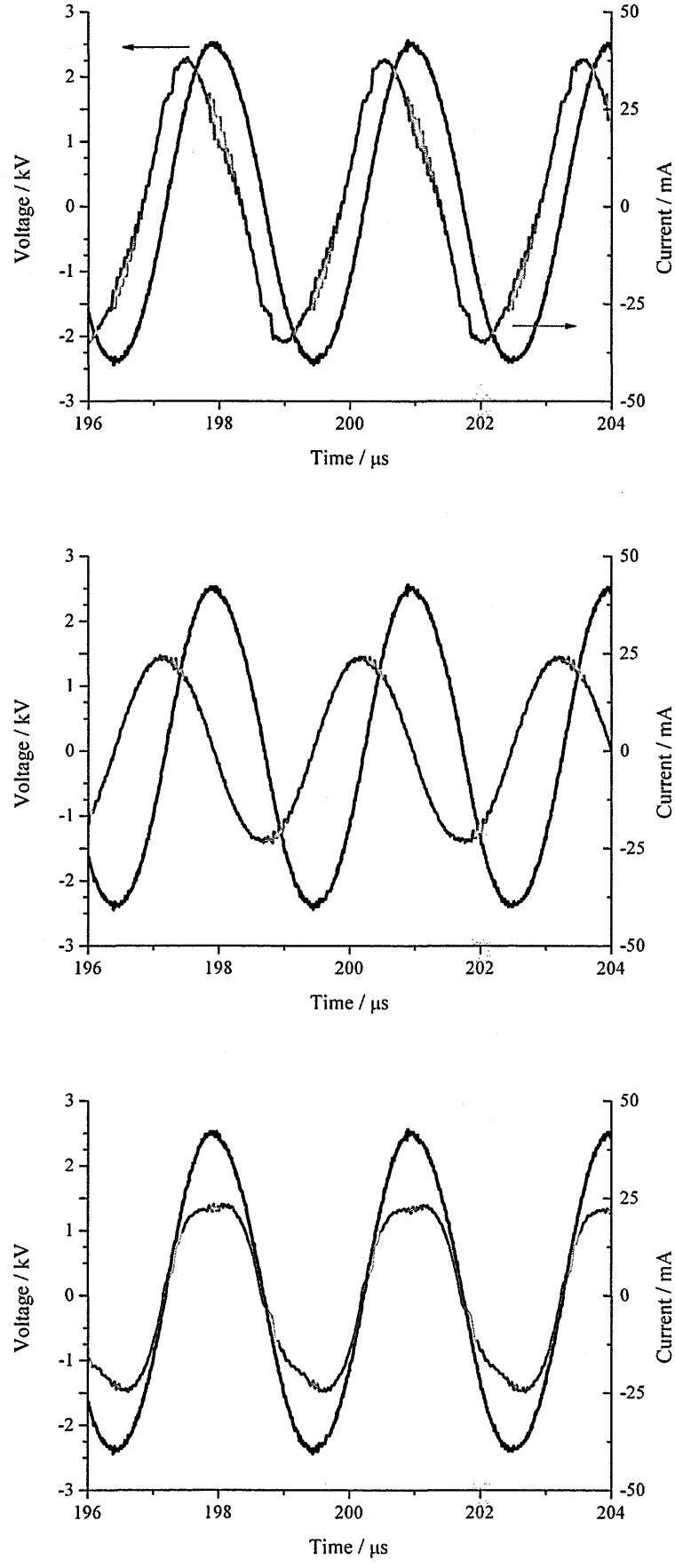

Figure 2.2: The total (top), displacement (middle) and conduction current (bottom) waveforms for a 15 mm electrode separation of the plasma; voltage (black), current (red).

Meanwhile, using Ohm's law, the total current is calculated from the voltage drop across the 100 Ω resistor in series with the top electrode and ground as measured using a standard oscilloscope probe. Due to the RF voltage sustaining the plasma, the total current consists of both displacement and conduction current components. The conduction current is obtained by making a point-by-point subtraction of the displacement current from the total current. For a given total current (figure 2.2 - top), the displacement current is measured by increasing the voltage between the electrodes with no plasma present (i.e. at pre-breakdown levels) to a voltage level equivalent to that measured with the plasma present. The displacement current can be readily identified from its $\pi/2$ phase difference with respect to the voltage (figure 2.2 - middle). The measured data set for the displacement current is then subtracted from the total current data set to leave the conduction current (figure 2.2 - bottom). Results can then be expressed in terms of the rms conduction current so as to have a comparable input setting to that used for the numerical model (to be described in the next chapter) and are calculated using the standard formula;

$$f_{rms} = \sqrt{\frac{1}{b-a}\int_a^b [f(t)]^2 dt} \tag{2.1}$$

where f_{rms} = rms function (voltage/current), a and b are respectively the lower and upper limits of the integral (in this case, the upper and lower time points of one period of the waveform) and $f(t)$ = general function for the measured waveform (voltage/current).

2.3.2 V-I curve

The voltage amplitude as a function of the conduction current amplitude is given in figure 2.3. The current range represents the stable region of operation. For a 15 mm electrode separation (used for most measurements), initial measurements show that below a conduction current amplitude of 13 mA, it is not possible to sustain the plasma. Above a conduction current amplitude of 45 mA, the plasma becomes increasingly unstable between the electrodes owing to gas heating and turbulent convection. The

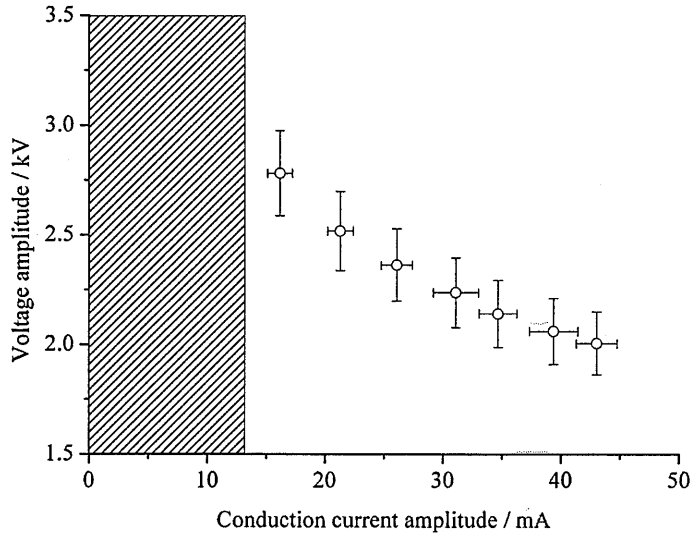

Figure 2.3: The voltage-current (V-I) curve for the plasma.

decrease in voltage as the current increases is similar to the behaviour near glow-to-arc transition in a DC glow discharge [32]. However, in contrast to the runaway ionisation associated with the DC glow, the RF cycle itself restricts the level of ionisation over the period of the cycle, keeping the plasma stable.

2.3.3 Amplitude modulation

The common method of sound generation in a plasma is through *amplitude modulation* of the conduction current and it is this method that is utilised here. Amplitude modulation (AM) is a form of signal transmission where the amplitude of a generally high frequency carrier wave is varied by a lower frequency signal. Mathematically, this combination of two sinusoidal signals is expressed as follows:

$$AMsignal = [A + f(t)]\cos(\omega_c t) \tag{2.2}$$

where A and ω_c are the amplitude and angular frequency of the carrier respectively and *f(t)* is a general function for an arbitrary signal used for modulation [33]. To produce amplitude modulation, the 'steady-state' configuration described in figure 2.1 is adapted by connecting an audio source across the DC power supply into the power stage (figure 2.4) in order to modulate the DC input signal (A). The audio source con-

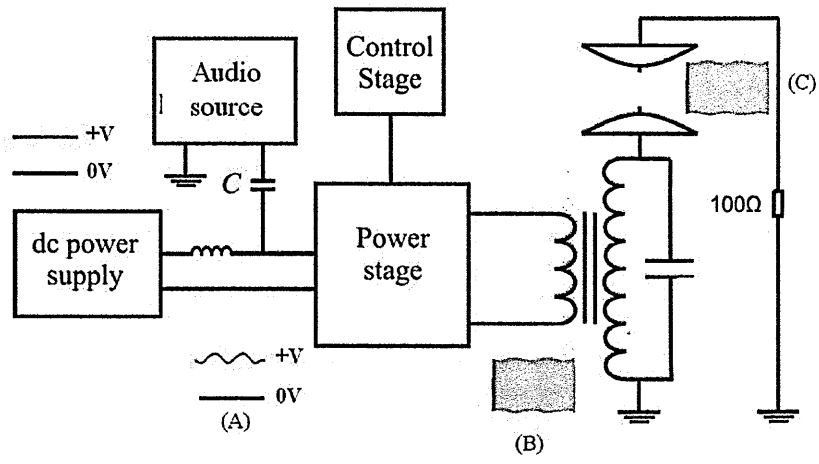

Figure 2.4: An amplitude modulation of the input RF signal.

sists of a Thurlby Thandar TG1304 function generator connected to a power amplifier with a bandwidth of 0.1 Hz-100 kHz.

A capacitor, C, placed in series with the amplifier output blocks the DC signal from the power supply and prevents damage to the amplifier. The fast switching of the power stage creates modulation on both peaks of the output square wave (B). As described previously, the fundamental frequency is filtered by the primary coil, transferring an amplitude modulated signal to the plasma between the electrodes on the secondary coil (C). An example of the amplitude modulated total current, consisting of a carrier frequency of around 322 kHz and a modulation frequency of 3 kHz, is given in figure 2.5 along with its Fourier spectrum. The relative amplitudes of the carrier and sideband components correspond to the steady state and modulation current amplitudes in the time domain and highlight the inefficency of the AM method for data transmission. Here, though, since the carrier maintains the plasma, it is not appropriate to consider its energy as being 'wasted'. The magnitudes of the sidebands lie significantly below the main carrier component indicating that the majority of the electrical energy goes into the carrier signal.

The effect of the current modulation on the voltage can be seen in figure 2.6. The voltage modulation should follow the current modulation along the curve. Small amplitude modulation will remain in a linear regime whereas larger amplitude modulation may result in non-linear distortions in both the electrical waveforms and/or the acous-

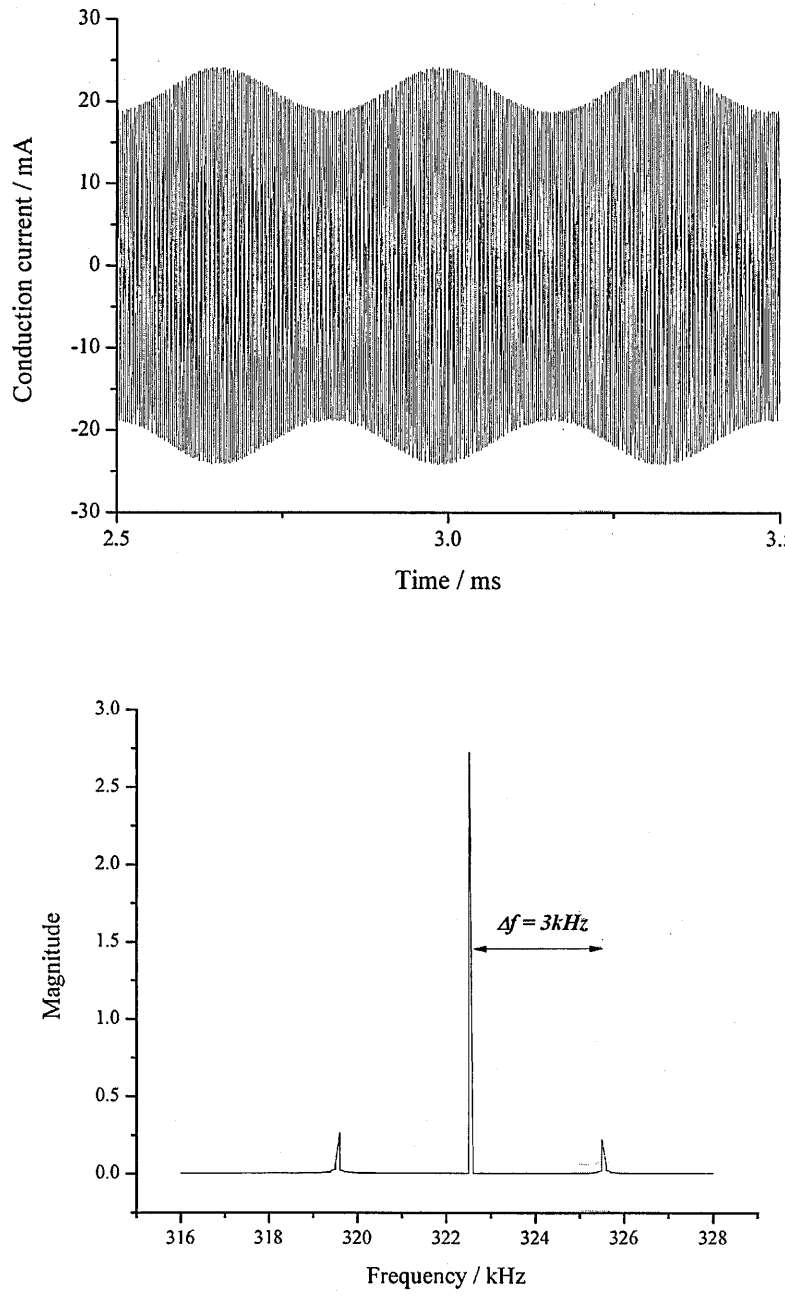

Figure 2.5: Amplitude modulation of the total current with modulating frequency of 3 kHz (top) and its corresponding FFT (bottom).

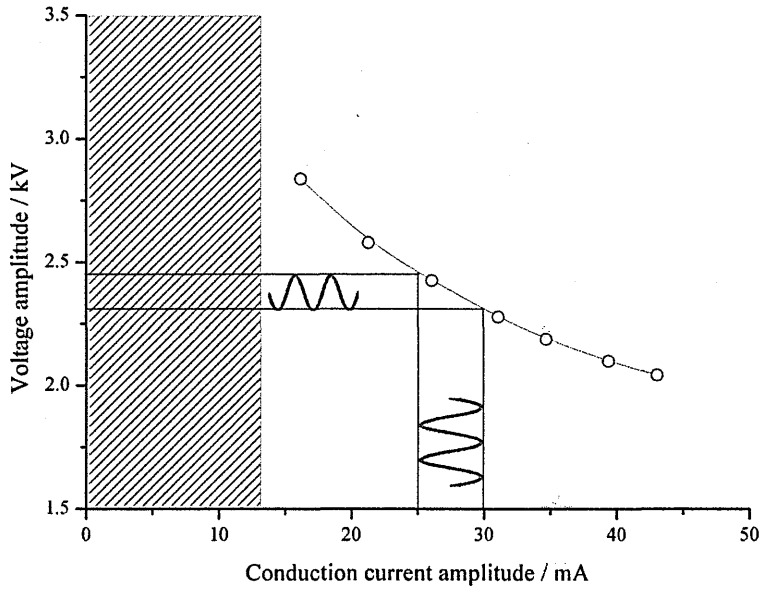

Figure 2.6: Modulation of the current results in a modulation of the driving voltage that follows the V-I curve.

tic signal; this relationship between the electrical and acoustic signals will be explored later in this chapter.

2.3.4 Modulation depth

The general way of describing the level of amplitude modulation on a steady state signal is to calculate the *modulation depth* (figure 2.7). The modulation depth is defined as the ratio of the modulation amplitude (B) to the steady-state amplitude (A). For clarity, in this thesis the modulation depth is calculated with respect to the modulation on the conduction current (rather than the modulation on the voltage signal).

2.3.5 Demodulation

The modulating components of the voltage and current waveforms are recovered using a diode detector circuit. In one possible configuration, a Tektronix high voltage probe is fitted with additional circuitry designed to adjust its response to give a uniform sensitivity over a wide frequency range. However, the combination of this with a passive type filter leads to underestimation of the voltage amplitude due to the low input impedance of the circuit. As an alternative, an active second-order Sallen-Key

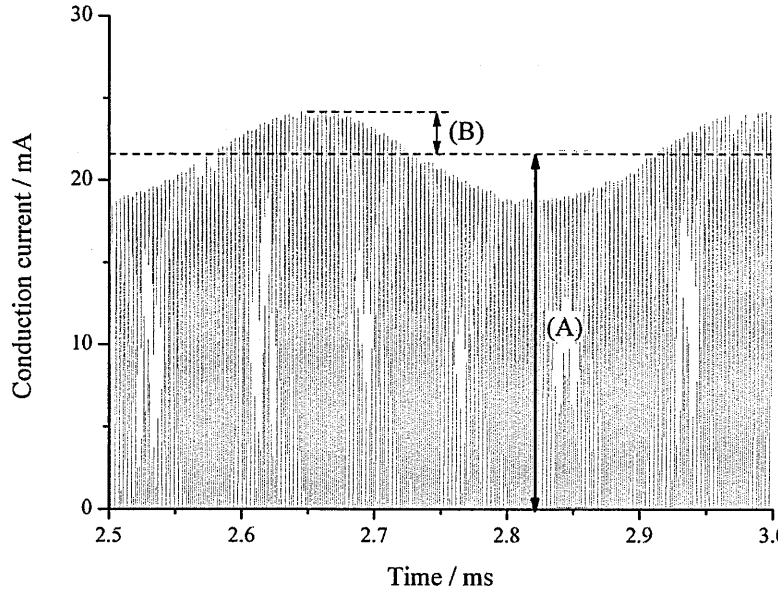

Figure 2.7: The definition of modulation depth.

filter is used (figure 2.8 - top). The diode at the circuit input rectifies the AM signal (A) and the high resistance across the input (B), together with the high input impedance of the op-amp (C), avoids significant loading of the probe circuit. The filter has unity gain and the resistance and capacitance values determine the high cutoff frequency.

The frequency response of the filter and probe combination was measured using an amplitude modulated input signal of known amplitude with the output connected to the high impedance, DC input of the oscilloscope. The response of the filter was measured at several frequencies up to 100 kHz (figure 2.8 - bottom). The frequency response is unity up to 10 kHz. The resistor and capacitance values used in the filter were chosen to give a -3 dB cutoff at 50 kHz and this is seen in the filter response. The response of the filter drops off completely above 100 kHz. Based on the filter response, no correction was applied to the amplitude of the demodulated electrical signals below 10 kHz. Where necessary, a correction was applied (based on a value calculated from a best-fit) to the drop off region above 10 kHz. The phase response of the filter was also measured by fitting the demodulated signal to the original amplitude modulated signal from which it was extracted. Measurements at several frequencies show that the filter induces a phase shift of approximately 0.28 radians for all frequencies measured. Consequently, this was applied as a correction to all electrical signals where the filter

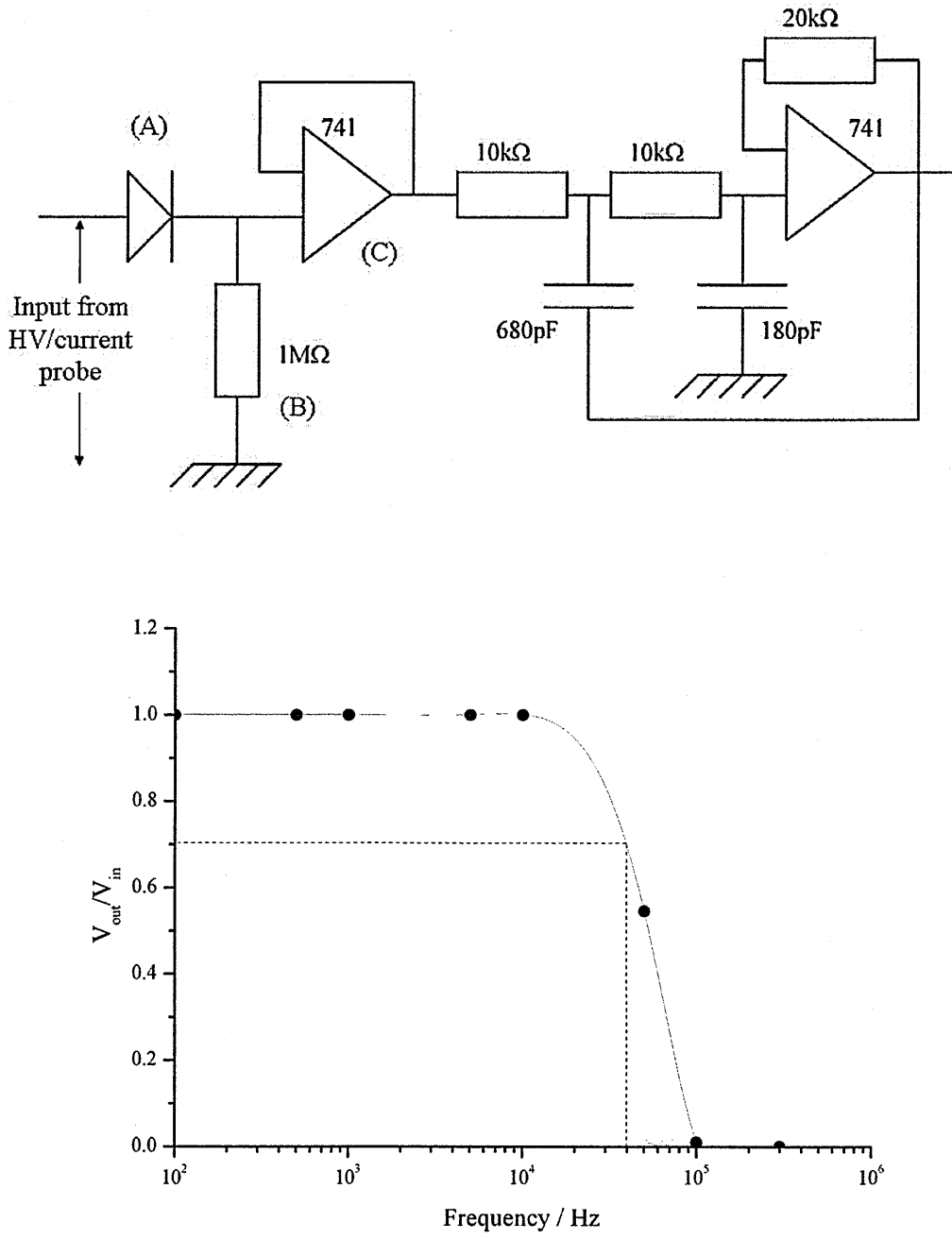

Figure 2.8: The circuit diagram for a diode detector circuit with an active Sallen Key filter (top) and its frequency response curve (bottom).

was used.

2.3.6 Modulated conduction current

The point-by-point subtraction method described in section 2.3.1 requires a sufficient number of sampled data points over the RF period in order to obtain an accurate evaluation of the conduction current. This method becomes problematic when applied to an amplitude modulated (AM) signal, in particular where there is a large difference in frequency between the two time-varying signals used to form it. Through point-by-point subtraction of a steady-state signal it was found that a minimum of 20 points was required over the RF period for calculation accuracy. However, if a 300 Hz modulation signal is applied, and the modulated signal is then measured using a time window of 5 ms from an oscilloscope, 33000 samples points must be acquired for calculation accuracy. Although oscilloscopes are available with this resolution, the long acquisition times involved make them impractical to use. Therefore, to determine the modulation on the conduction current, an algorithm was developed that calculates the AM conduction current from measured electrical characteristics. Using equation 2.2, an AM voltage waveform was constructed in MathCad using the measured steady-state and modulating voltage signals. A continuous cosine function was fitted to the measured signal which gave a sufficient number of points for accurate calculation. The simulated modulated voltage function, V_{mod}, was used to calculate a modulated displacement current as follows,

$$I_{dmod} = C\frac{dV_{mod}}{dt} \tag{2.3}$$

where C is the capacitance between the electrodes of the Tesla coil (calculated from the measured electrical characteristics to have a value of 5.0 pF $\pm$ 0.2 pF). The total modulated current was calculated in a similar fashion to the voltage function using the measured steady-state and modulating current components. The modulated displacement current was subtracted from the total modulated current to give the modulated conduction current alone, from which the modulating component was extracted.

2.3.7 V-I relationship under modulation

The expected relationship between the current and voltage under modulation is given in figure 2.6. To confirm this relationship, a 3 kHz modulation signal was applied to the conduction current. The plasma in its unmodulated state was operated with a conduction current amplitude of 23 mA. This value was chosen as it lies in the mid-point of the stable operating region of the V-I curve and allows sufficient modulation depth on the current for it to remain above the minimum level required to sustain the plasma; 3 kHz is chosen as a representative 'mid-range' audio modulation frequency. The expected variation in voltage was calculated by fitting a second order polynomial function to the V-I curve and calculating the expected voltage variation from the modulating current. The predicted and measured modulation voltage values given in figure 2.9 show a good correlation for the range of modulation amplitudes on the conduction current. The range of modulation depths given here relative to the steady-state conduction current ($< 10\%$) is considered low and well within the range that linear behaviour would be expected. However, an interesting effect occurs as the modulation level is increased. Figure 2.10 shows the normalised demodulated current and voltage waveforms taken from a 33 % modulation on a steady-state conduction current of 25 mA. At this greater modulation depth the voltage starts to deviate significantly from the sinusoidal behaviour observed at lower modulation depths. The increasing distortion in the voltage waveform results from the non-linearity of the V-I curve (figure 2.3). The conduction current remains sinusoidal in contrast to the distorted voltage; an FFT of the current shows the fundamental 3 kHz signal is dominant over an insignificant first harmonic component. Given the relationship between the conduction current and the acoustic signal described in chapter 1, it is expected that the harmonic-free modulating current should produce a near distortion free acoustic signal.

2.4 Acoustic measurements of the plasma

The background of the acoustic measurements is described in this section. The relevant terminology will be explained and the equipment and experimental set-up used to

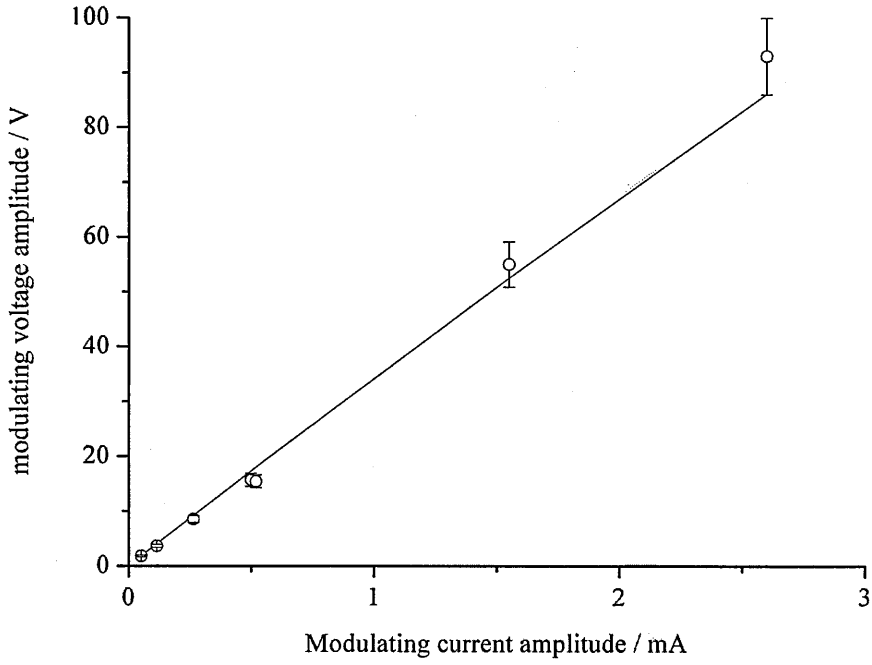

Figure 2.9: Predicted (line) and measured (circles) modulating voltage as a function of the modulating current amplitude.

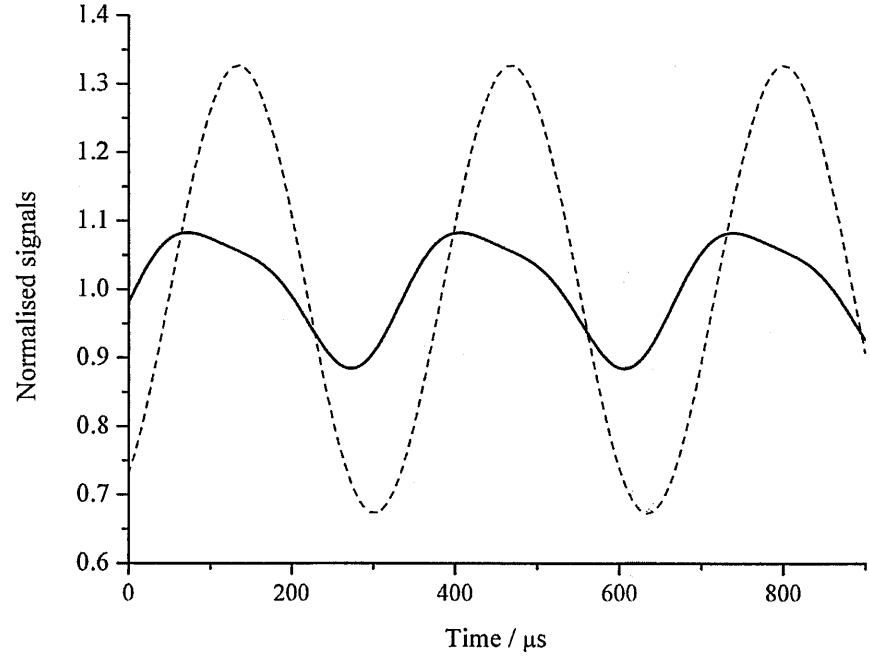

Figure 2.10: Measured modulating voltage (solid) and current (dashed) for a modulation depth of 33 %.

measure acoustic emission will be presented.

2.4.1 Sound Pressure Level

The *sound pressure level* (SPL) is the most common way of expressing the level of acoustic emission from a source. The human ear is capable of detecting pressure variations as small as 20 μPa and as large as 20 Pa; above this, damage is induced. Therefore the SPL from a source is expressed on a logarithmic (decibel) scale and is calculated using the following equation:

$$SPL = 20 \log \frac{P_e}{P_{ref}} \tag{2.4}$$

P_e is the rms amplitude of the measured pressure level and P_{ref} is a reference rms pressure level generally taken as the aforementioned threshold of human hearing (20 μPa). For reference, typical SPL values in an everyday environment are the background level of a library (30 dB/630 μPa), a domestic vacuum cleaner at 3 m (70 dB/63 mPa), a jet aircraft on takeoff from 25 m (140 dB/200 Pa) and a Saturn V rocket at lift-off from 300 m (200 dB/200 kPa) [1].

2.4.2 Anechoic chamber

The measurements of the acoustical characteristics of the plasma were carried out in an anechoic chamber (figure 2.11). The chamber is lined with wedges made from a foam material which has an impedance matched to air so it absorbs the incident sound wave effectively. The shape of each wedge is such that any sound that is reflected (rather than absorbed) is directed on to other wedges until it is eventually absorbed. This structure provides the 'free field' environment that is needed for acoustic measurements where the sound waves propagate with negligible perturbations. In addition, it ensures acoustic isolation and prevents the measuring device from being influenced by external noise.

2.4.3 Microphone set-up

For all measurements, the Tesla coil was placed in the centre of the chamber and the acoustic signal measured using a Bruel and Kjaer (B&K) 1/2" type 4165 condenser

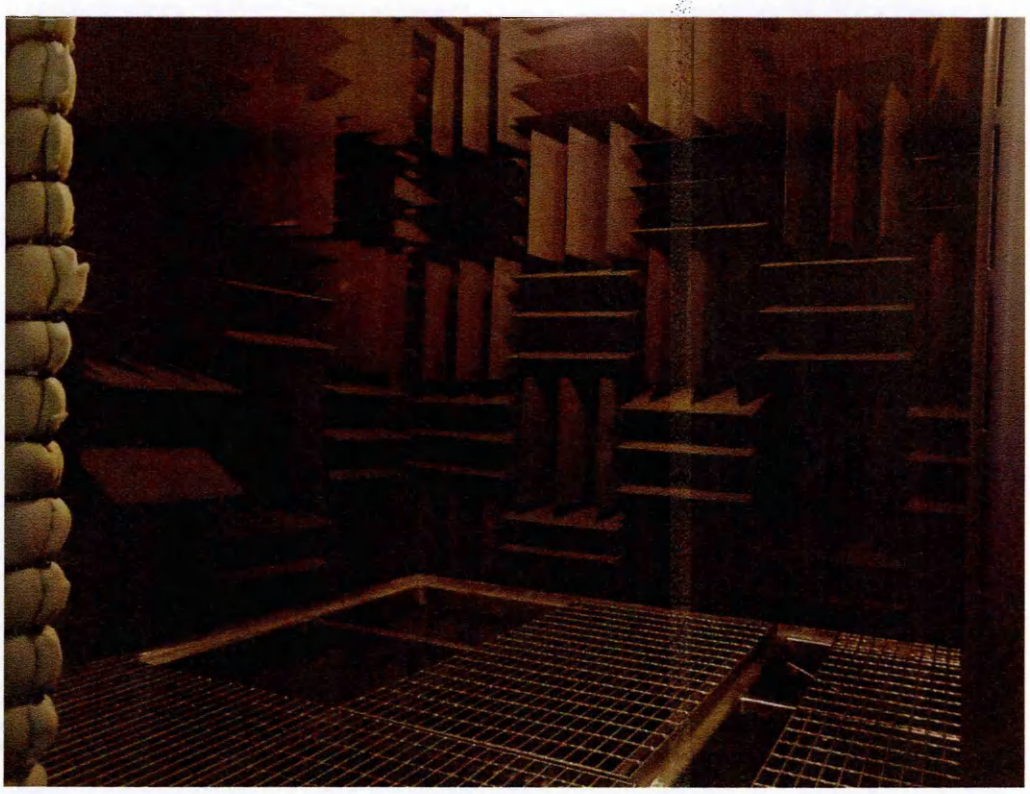

Figure 2.11: The anechoic chamber used for the acoustic measurements.

microphone connected to a B&K type 2619 preamplifier (figure 2.12). This diameter of microphone ensures minimal perturbation of the acoustic field relative to the wavelengths of the signals of interest. The preamplifier was connected to a B&K measuring amplifier (type 2608) which indicates the SPL on an analogue dial. Initial measurements with the plasma ignited showed the microphone set-up to be susceptible to electromagnetic interference generated by the Tesla coil. The source of this interference was a high frequency ring down effect during the switching at the chopping circuit. This effect was overcome by adding an external bandpass filter into the circuit of the B&K measuring amplifier to eliminate the high frequency signals. The resultant microphone/amplifer and filter combination provides a near flat frequency response between 20 Hz and 50 kHz, although the emphasis of this work is on the audio frequency range up to 20 kHz. The output from the measuring amplifier was connected to an oscilloscope, providing an electrical signal with an amplitude proportional to that of the incident acoustic pressure. All measuring and drive equipment was positioned outside the chamber to avoid introducing reflecting surfaces and background noise. The sound measurement system in its entirety was calibrated using a 1 kHz sound calibrator (B&K

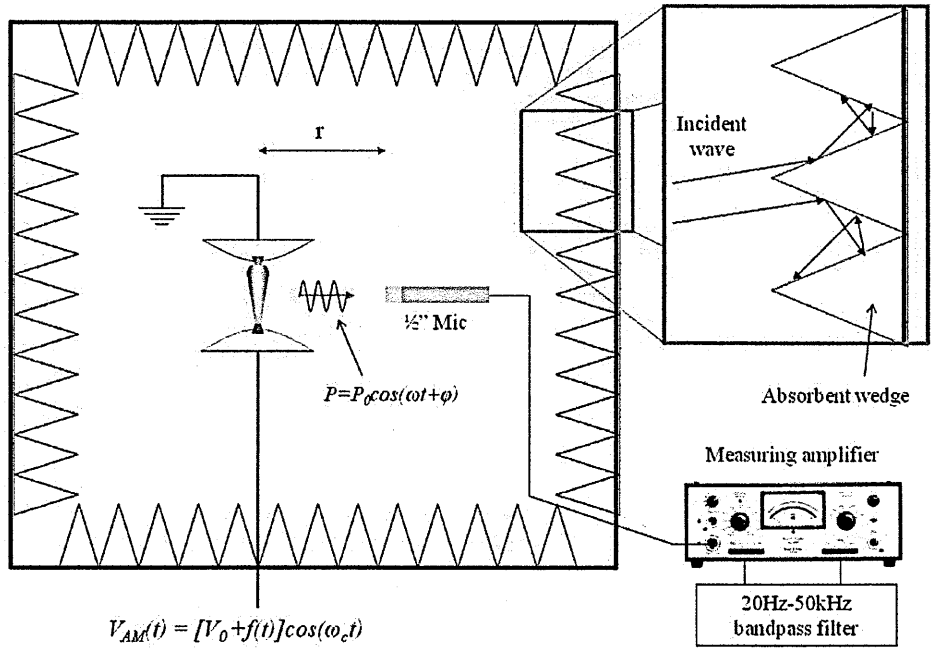

Figure 2.12: The set-up for measurement of the plasma using the microphone.

type 4320) which emits two known SPL levels of 94 dB and 114 dB, equivalent to 1 Pa_{rms} and 100 Pa_{rms}. Then with the plasma ignited (but not modulated) to replicate actual measurement conditions, the calibrator was reattached to the microphone and measurements were made at both reference settings and were found to be within $\pm$ 1 dB of the calibrated values. Environmental effects such as humidity and temperature may also affect the long term stability of the microphone. Based on the 'day to day' variation of temperature and humidity, and using the manufacturer's specification for such effects, an additional uncertainty of $\pm$ 1 dB has been added to account for this.

2.4.4 Evaluation of the chamber

Both a fully anechoic and a hemi-anechoic chamber were used for the acoustic measurements. A hemi-anechoic chamber differs from an anechoic one in that part of the chamber remains uncovered for use as a controlled reflecting surface. The choice of chamber in this instance was dependent on availability. When the fully anechoic chamber was unavailable, the hemi-anechoic chamber was adapted with additional absorber on most of the floor area in order to recreate near fully-anechoic conditions (though

part of the door and floor region were left uncovered). An evaluation of the chamber was carried out to determine the effectiveness of these adaptations in reducing the noise and reflection. The quality of the noise isolation can be assessed by monitoring the background SPL measured using the microphone placed in the chamber. For the fully anechoic chamber, the background was around 20 dB while for the 'adapted' hemi-anechoic chamber it was around 26 dB. This can be considered sufficiently low for the measurements required here and, according to the typical SPL values quoted in section 2.4.1, this is quieter than a library.

The amount of reflection occurring in the chamber can be assessed by measuring the response at the microphone position to a short acoustic pulse emitted by the plasma. The sources of reflection can be identified through a time of flight calculation between the initial electrical pulse and the detection of acoustic signals at the microphone. Figure 2.13 shows the initial electrical pulse at time 0 ms followed some time later by the acoustic pulse arriving at the microphone and then a series of smaller amplitude signals resulting from multiple reflections. The time elapsed between the initial electrical pulse and the measured acoustic pulse is approximately 3.31 ms which corresponds to the electrode/microphone separation in this instance. A number of other sources are identified using this approach and correspond to reflections from the door and floor regions. Moving the door results in movement of the later reflected signal. The signals that immediately follow the initial acoustic pulse are most likely caused by the structure of the Tesla coil itself. Its curved electrodes and metal frame provide multiple surfaces for reflection which leads to increased uncertainty in the SPL due to interference. Normally, this could be reduced through the use of absorbent material on the surfaces but, due to the significant amount of heat generated from the plasma during its operation, it is hazardous to apply combustible foam material in such a region. Multiple reflections such as these may lead to large variations in the SPL due to interference at the microphone. A simple method for evaluating the effect is to measure the SPL at several different plasma/microphone separations and then apply a correction to adjust the signal amplitude for that expected at a common reference distance. The results show a spread of around $\pm$ 3 dB and this has been applied as an uncertainty to best

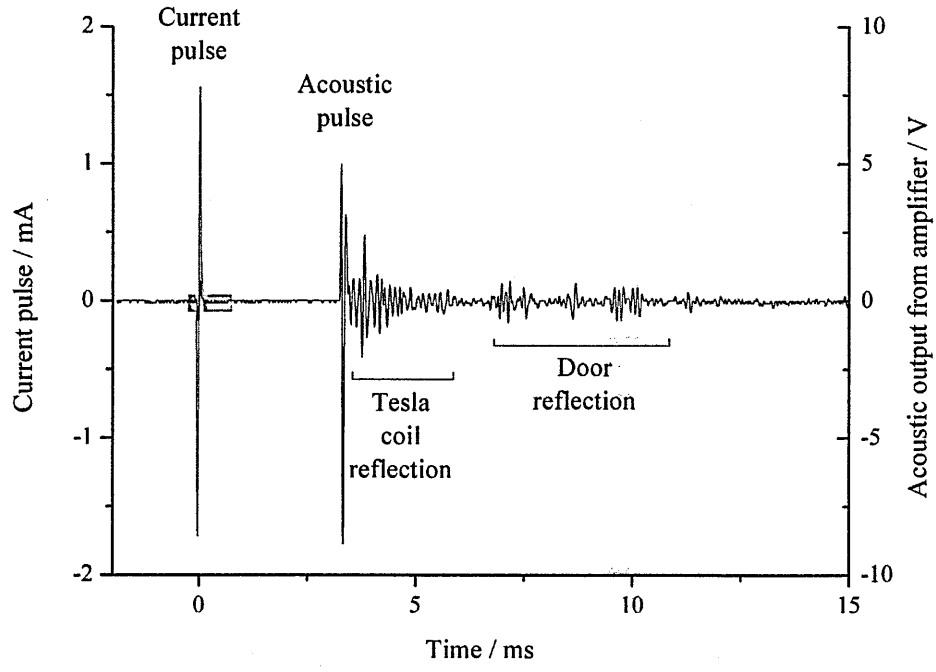

Figure 2.13: A single pulse applied to the current (red) shows the performance of the hemi-anechoic chamber through the measurement of the acoustic signal (black)

accommodate the influence of reflection on the SPL.

2.5 Results of the acoustic measurements

The acoustic characteristics of the plasma were measured and are presented in this section. The measurements completed are typical of those used in acoustic measurement and are designed to determine the acoustic field over a number of frequencies. Reference will be made to other plasma sources that were established in Chapter 1. Unless stated, the electrode separation was set to 15 mm.

2.5.1 Pulsed response

The pulsed response presented previously in the evaluation of the acoustic chamber also shows the relationship between current and the acoustic signal. Figure 2.13 has been expanded over the time period t = -0.5 to 4 ms (figure 2.14). The additional pulse present in the microphone signal at 0 ms is electrical pickup measured by the micro-

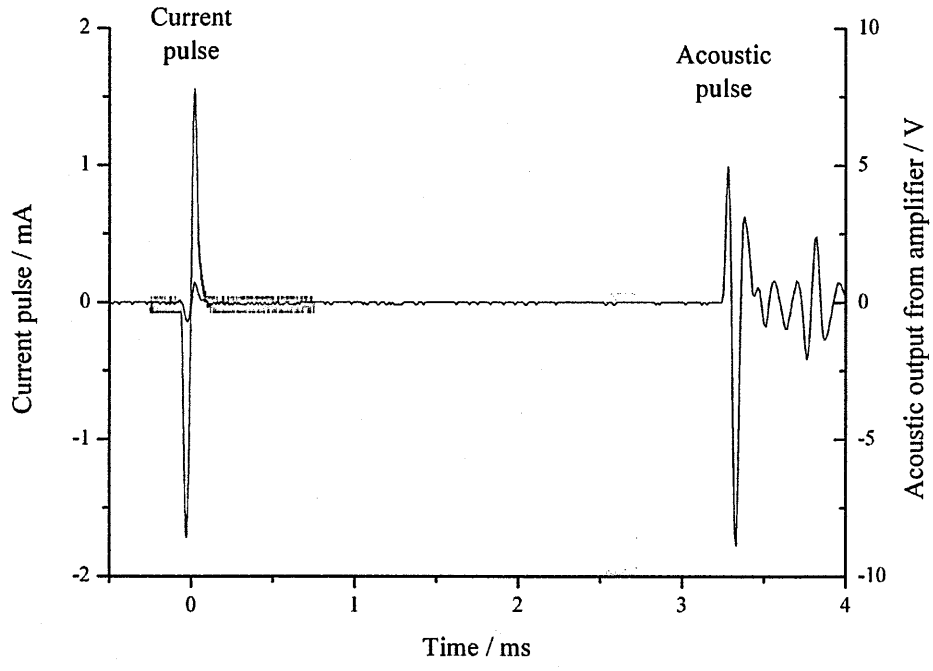

Figure 2.14: A close up of the current (red) and acoustic pulses (black) from figure 2.13

phone set-up. The plot shows the acoustic pulse to be proportional to the derivative of the modulating current but this is contrary to the theory of Ingard [28, 29] which is expressed in equation 1.2. The response of the measured acoustic signal implies that, as with the response of a conventional mechanical loudspeaker, there is a delay in the response between the input electrical signal and the output acoustic signal. This will be explored later in this chapter.

2.5.2 Modulation depth, SPL and distortion

The loudness of the source can be altered through the level of modulation applied to the current. The effect of altering the modulation depth on the SPL is explored in this section. The plasma was sustained at a current of 23 mA and a 3 kHz audio signal was applied to the current. Several modulation amplitudes were applied to the current and the SPL measured with the microphone positioned at a distance of approximately 0.96 m from the electrodes.

Figure 2.15 shows a near linear increase in the SPL as a function of the modulating current amplitude, with the highest modulation amplitude of 2.6 mA corresponding to

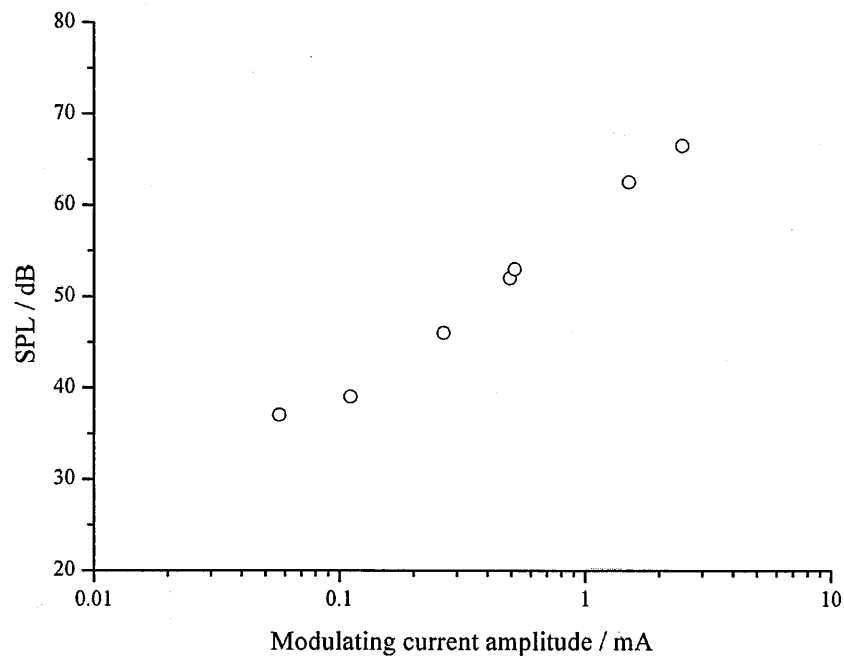

Figure 2.15: The SPL as a function of the modulation depth on the conduction current; electrode/microphone separation = 0.97 m.

a SPL level of around 67 dB. Further measurements were completed with a constant 1 mA modulation amplitude applied to several steady-state conduction currents. The SPL remained constant at approximately 54 dB for all conduction current settings. Hence, it can be concluded that the SPL is independent of the steady state current and dependent only on the modulation level. The 'quality' of an acoustic signal can be ascertained by the level of distortion present and indicates how well an input signal is reproduced. Ideally, a pure sinusoidal electrical input signal will be replicated as an output sinusoidal acoustic signal. The detection of harmonics above the fundamental in the acoustic signal can indicate distortion in the signal. The total harmonic distortion, or THD, for an acoustic waveform gives a quantitative measure of this effect and is calculated as follows,

$$THD = \frac{\sqrt{(\sum_{(i=1)}^{n} V_i^2)}}{V_0} \tag{2.5}$$

where V_i is the rms voltage of the ith harmonic component and V_0 = rms voltage of the fundamental component. As a guide, the limit for detectable distorted sound by the human ear in terms of THD is 1 % [34]. To determine the harmonic content,

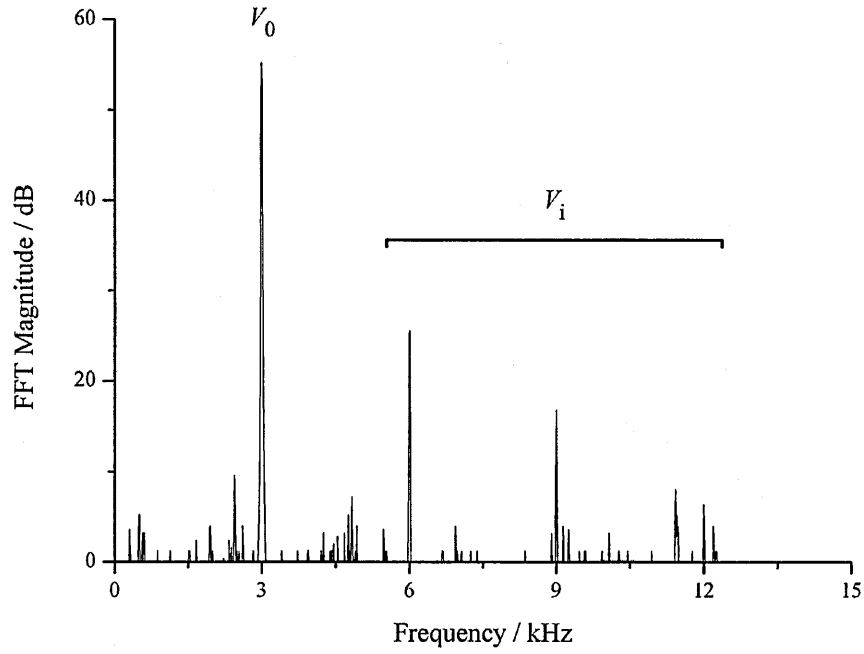

Figure 2.16: FFT of an acoustic signal with 3 kHz modulation frequency; conduction current amplitude = 26.4 mA, modulation amplitude = 0.27 mA.

Fourier transforms (FFT) of the acoustic signal and demodulated electrical signals for the current modulation levels given in figure 2.15 were taken from the oscilloscope; a sampling rate of 25 kHz and the Hanning window function were used. Figure 2.16 gives an example of an FFT of the acoustic signal with a 3 kHz fundamental frequency. The background levels, resulting from ambient noise and a small level of electrical pickup of the microphone, were subtracted for each FFT and the THD calculated from the magnitudes of the fundamental and harmonic components using equation 2.5. Figure 2.17 shows the THD determined from the acoustic signal and the modulating components for the voltage and current for several modulating amplitudes. While the THD for the acoustic waveform exceeds the 1% limit, it stays below 4 % and tends to follow the equivalent THD determined for the modulating current. The THD for the voltage reflects the distortion that occurs for increased modulation depths (figure 2.10).

2.5.3 Frequency response

An ideal source has a flat frequency response to a constant modulating current amplitude but the known constraints of mechanical loudspeakers make this near impossible

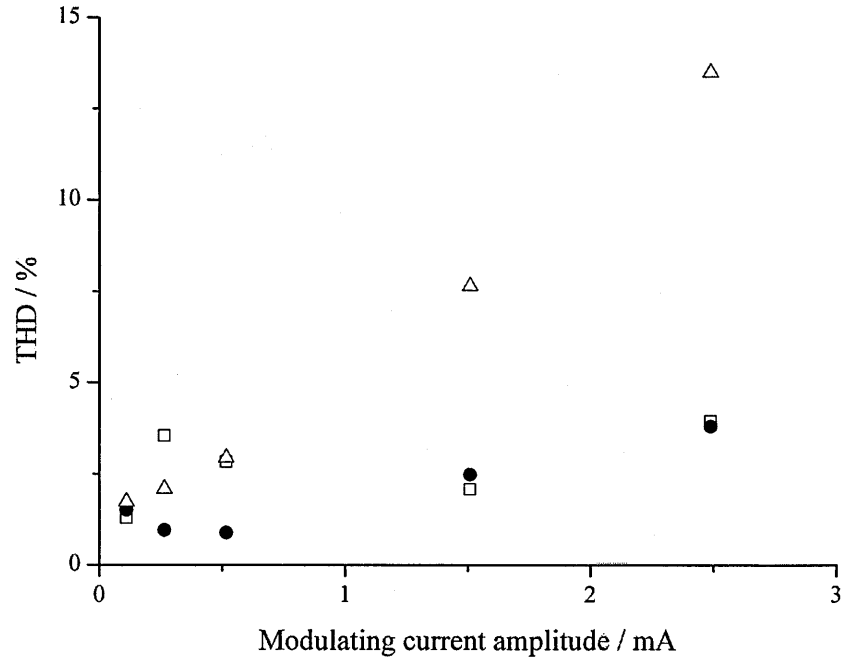

Figure 2.17: The total harmonic distortion levels of the acoustic (square), current (circle) and voltage (triangle).

without the use of several drivers. The frequency response of the plasma was measured by sustaining it with a steady conduction current amplitude of 23 mA and applying a constant amplitude modulating signal at several discrete frequencies between 300 Hz and 20 kHz. The microphone was positioned at a distance of 0.5 m away from the electrodes and the background level in the anechoic chamber was 23 dB. Figure 2.18 gives the response of the plasma in terms of SPL as a function of frequency. It can be seen that the SPL above 4 kHz increases steadily at a rate of 1 dB/octave. Below 4 kHz, the SPL shows a sharp drop down to 35 dB at 300 Hz. Despite this decrease, the acoustic emission is still audible in the anechoic chamber. The frequency limitations of the plasma source have been documented and relate to the physical characteristics of the plasma itself such as its thermal conduction, gas diffusion and the radiation impedance of the air into which the acoustic wave propagates [5, 18]. Thermal expansion in sound reproduction relies on adiabatic conditions within the plasma volume during modulation and a negligible thermal conduction away from the source. Such conditions are achieved at high modulation frequencies (usually in the kilohertz range)

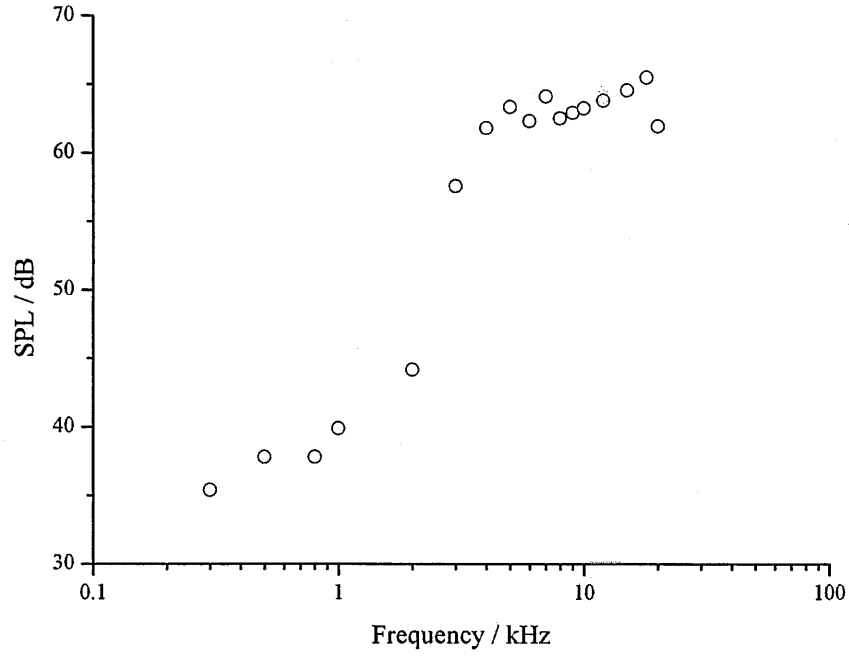

Figure 2.18: SPL as a function of frequency; Electrode/mic separation = 0.5 m.

where the thermal conduction of the gas molecules is a much slower process than the energy input to the plasma, resulting in thermal energy being contained within the volume. Under slow modulation, the time taken to transfer energy into the volume is comparable to the rate of thermal conduction out of the volume. An approximate value for a thermal time constant, τ_{TD}, can be determined from the following:

$$\tau_{TD} = \frac{L^2}{\alpha_{air}} \tag{2.6}$$

where the thermal diffusion coefficient, $\alpha_{\mathrm{air}} = \kappa_{\mathrm{air}}/\rho_{\mathrm{air}}C_{\mathrm{air}}$, is calculated from reference values for the specific heat capacity (C_{air}), air density (ρ_{air}) and thermal conductivity (κ_{air}) of an air plasma at 2500 K [35]. Only diffusion in the radial direction has been considered with the length scale, L, representing the plasma radius. This will be evaluated in a later chapter but a nominal value of 1.5 mm is used here. Using these values, the thermal diffusion time constant is around 2.2 ms which is comparable to the period of a waveform at 450 Hz. Applying a modulation frequency below this limit can lead to a number of effects; the energy gained will produce an eventual steady increase

in gas temperature but will be accompanied by a proportional decrease in gas density with the pressure remaining constant throughout. At low frequency, the heat gained by the neutral gas molecules will be quickly conducted away within the modulating cycle resulting in a negligible change in gas temperature or pressure. Another factor in low frequency drop off is the *radiation impedance* of the air into which the pressure wave propagates. With a conventional mechanical loudspeaker, the loading of the medium into which the driver oscillates contributes to the overall impedance of the device. This radiation impedance is strongly dependent on the frequency, the driver's surface area and the properties of the medium to which the driver is coupled and can be illustrated using the impedance of a pulsating sphere,

$$Z_r = \rho_0 c S \cos\theta_a e^{j\theta_a} \tag{2.7}$$

where ρ_0 is the air density, c is the speed of sound in air, S is the surface area of the sphere and $\cot\theta_a = ka$ with k = wavenumber and a = source radius [1]. Equation 2.7 has been used to calculate the reactive and resistive components of the radiation impedance for two different radius sources and the plots for both components are given in figure 2.19. An analogy can be made to electrical impedance where the reactance results in energy storage while the resistive impedance leads to energy transfer. Where the radiation resistance is approaching or at unity, the energy generated at the surface is transferred into the medium and propagates as acoustic energy. The comparison between the two radii of 7.5 mm and 75 mm shows that for larger surface area, the resistance at lower frequencies increases and the drop-off in SPL occurs lower down in the frequency range. The plasma used in the present work has comparable dimensions to that of a 7.5 mm radius sphere, indicating that a drop off in the resistance can be expected at around 10 kHz leading to negligible emission at 0.1 kHz.

Despite the limitations described above, sound from the plasma studied here can, in fact, be measured (and heard) down to 300 Hz. This may result from a 'forcing' mechanism as described in Chapter 1. In a similar way to thermal diffusion, this effect will be influenced by *gas* diffusion from the plasma column and relates to the forcing effect between the heavier particles in the plasma. Using equation 2.6 and a

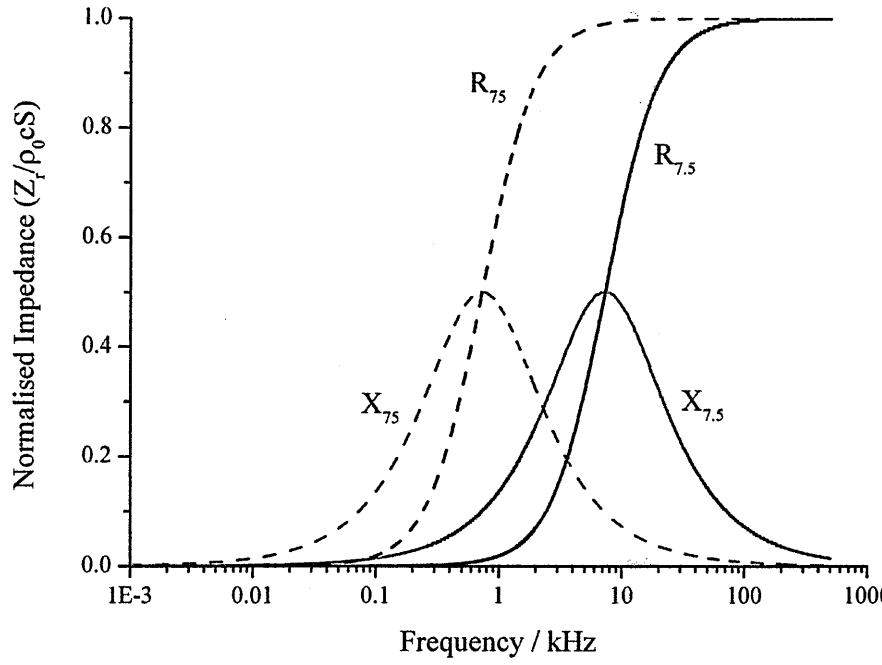

Figure 2.19: The resistive and reactive components (R, X) of the radiation impedance for a pulsating sphere with radius $r = 7.5$ mm (solid) and $r = 75$ mm (dashed).

calculated value for the gas diffusion rate of nitrogen [35, 36] shows the time taken for the charged ions to diffuse out of the plasma is comparable to the period of an audio signal in the lower audio frequency region and this may indicate some contribution to sound generation from this mechanism. While the forcing mechanism may contribute to sound generation, one other factor that may enhance the low frequency emission is the shape of the electrode structure itself. Figure 2.20 shows a photograph by Francis Barraud of 'Nipper' looking into the horn of a cylinder phonograph. As for Klein's Ionophone, the curved structure of the horn (which is similar in shape to the electrode structure of the Tesla coil) acts as a mechanical transducer turning a large pressure amplitude generated over a small area (from the vibration of the phonograph diaphragm attached to the needle) into a small pressure variation covering a much larger area at the end of the horn and improving the impedance matching at low frequencies. Typical impedance plots for an exponential horn have been given along with those for a circular piston mounted in an infinite baffle (figure 2.20). While the piston shows a similar response to the pulsating sphere calculated previously, the resistive impedance of the

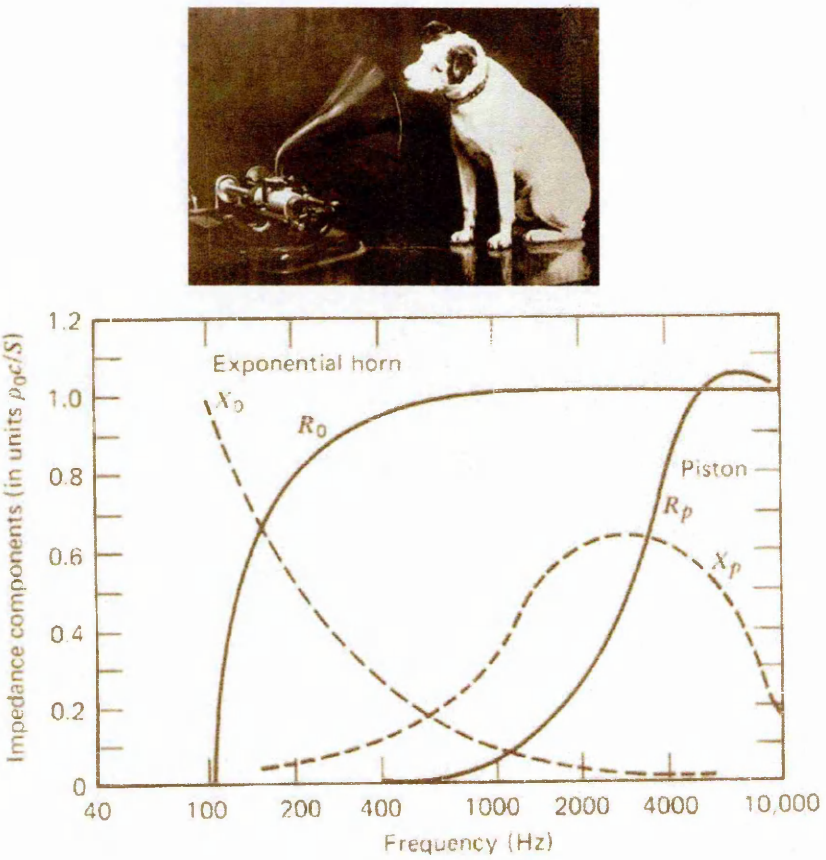

Figure 2.20: 'Nipper' looking into the horn of a cylinder phonograph (top) and the calculated impendance from a circular piston mounted in an infinite baffle (R_p, X_p) and an infinite exponential horn loudspeaker (R_0, X_0) (plot reproduced from [1]).

horn extends down to lower frequencies and again leads to an increased SPL in this region. The physical attributes of the Tesla coil have not been explored further in this project. Altering the electrodes will impact on the electrical environment so it would be difficult to keep the plasma conditions constant but the manipulation of the sound field through controlled boundaries may benefit from further investigation.

2.5.4 SPL and electrode separation

The dependence of the SPL on the source size was explored in the previous section through modelling of a pulsating sphere. This can also be investigated experimentally by changing the dimensions of the plasma (by varying the electrode separation) and then measuring the SPL for a known modulation amplitude on the current. The amplitudes applied to the current were the same as those used in section 2.5.2 and the SPL was measured for electrode separations of 5, 10 and 15 mm. Figure 2.21 gives

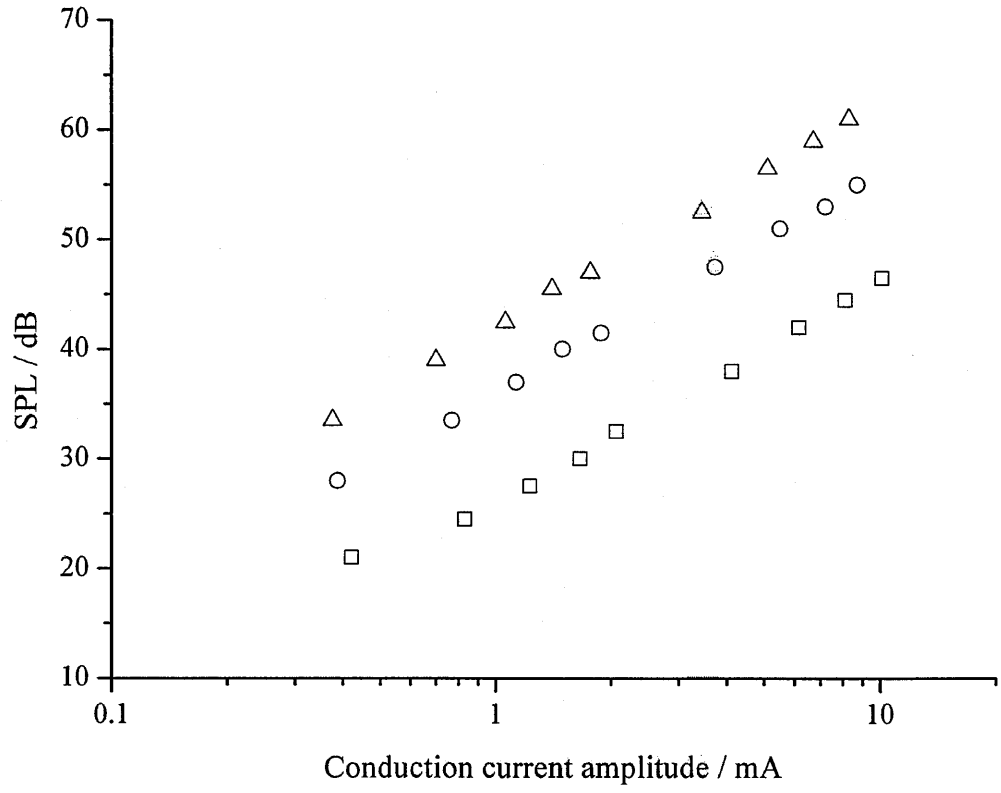

Figure 2.21: SPL as a function of electrode separation for 5 (square), 10 (circle) and 15 mm (triangle) electrode separations.

the measured SPL as a function of modulation current amplitude for the three electrode separations and shows a clear dependence on the plasma dimensions, although the increase in SPL between electrode separations is greater than expected. As an example, if the surface area of a cylinder is doubled this translates to a 6 dB increase in SPL. The equivalent increase from a 5 mm to a 10 mm electrode separation results in a 10 dB increase, though the plasma plume is not a cylinder. The plasma pictured in figure 2.1 spreads outwards moving further up the column and these non-uniform dimensions will require more precise calculation of the surface area to determine its influence on the SPL; this will be returned to in the next chapter. However, the results show that the main body of the plasma makes a significant contribution to the audio reproduction in the plasma. While there are inherent difficulties in producing a large volume plasma at atmospheric pressure [31], large area sources have been developed and studied previously and show that high SPLs can be achieved [20, 26].

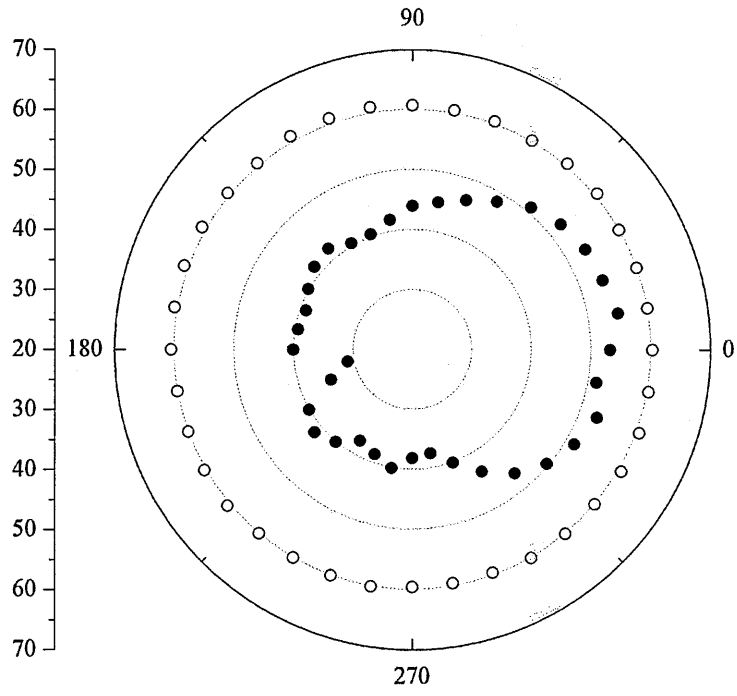

Figure 2.22: The polar response of the plasma for a 2 kHz signal (open) and a reference measurement made with a mechanical loudspeaker (black); $r = 0.96$ m.

2.5.5 Directivity

Directivity is a useful measure of the nature of a source and identifies the regions where the acoustic emissions are strongest. Deviations from a constant level of emission can be explained by interference from an object in the acoustic field or by a characteristic of the source itself. Here, the polar response of the plasma and the radial dependence of the SPL level are measured. The Tesla coil was placed onto a rotating table with the microphone positioned at a distance of $r = 1$ m away from the electrodes. The Tesla coil was rotated in equal increments and, with a constant modulation level applied to the current, the SPL was measured at each position. For a comparison, the radial response of a conventional cabinet loudspeaker was measured using the same procedure. To determine the distance dependence of the plasma, several microphone/electrode separations were set up and, with a constant modulation level on the current, the SPL was measured at 10° increments. Figure 2.22 gives the radial response of a 120 mm diameter mechanical loudspeaker and the radial response of the plasma for a 2 kHz modulation frequency. The loudspeaker was positioned so that the front face radiates at the 0° radial position. The emission from the loudspeaker is characterisic

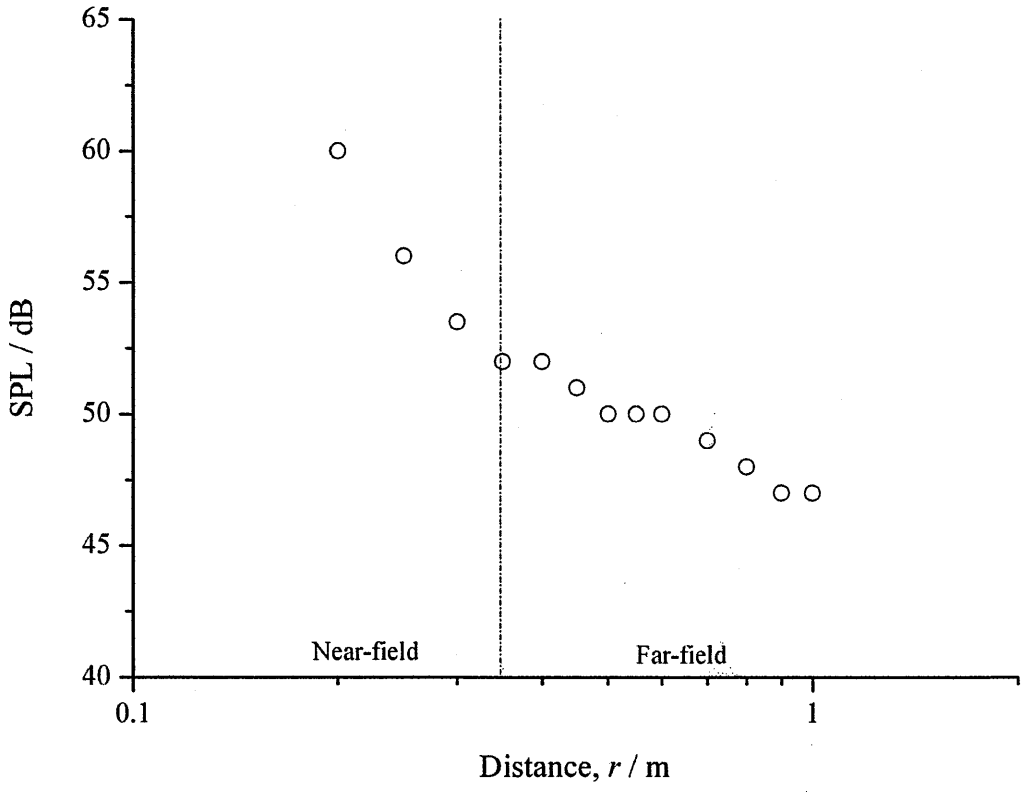

Figure 2.23: The SPL measured as a function of the distance from the plasma. The near- and far-field regions have been identified for the 2 kHz modulation frequency.

of a piston-like radiator mounted in an enclosure, where the SPL is highest on axis at the front face. The directional nature of the acoustic field is a result of the relative values of the wavelength relative to the diameter. In addition, the large drop off in SPL of around 20 dB that occurs toward the rear of the loudspeaker, is a result of energy being absorbed by the cabinet. By contrast, the radial response of the plasma shows behaviour typical of a spherical or cylindrical source, with a near constant SPL of around 60 dB $\pm$ 0.5 dB. Figure 2.23 shows the measured SPL level as a function of distance from the plasma, again with a 2 kHz modulation frequency. For electrical safety reasons, measurements within 200 mm of the plasma were not done. The near- and far-field regions are evident. The far-field is taken to be the region beyond two wavelengths from the electrodes which, for 2 kHz, is approximately 0.35 m. Applying a least-squares fit to the results in the far-field shows that the SPL decreases by 3.6 dB per doubling of distance. The length of the plasma source relative to the distance at which the SPL was measured suggests that the expected response would be similar to that of a point source where a drop-off of 6 dB per doubling of distance would be measured.

The calculated decrease lies significantly below this and implies a more complicated field structure due to the structure of the Tesla coil itself. This complicated behaviour extends to the near-field. The drop off in SPL, particularly in the region closest to the plasma, is greater than would be expected for both cylindrical and spherical sources and is most likely complicated by a combination of the more complex near-field structure and the effects of inteference as discussed previously.

2.6 Correlation of electrical and acoustic waveforms

The phase relationships between the modulated conduction current and the acoustic signals at 300 Hz, 1 kHz and 3 kHz are given in figure 2.24. The acoustic signal is corrected for the time of flight between the electrodes and the microphone and an uncertainty of around $\pm 14\mu s$ is applied based on this correction. As for the pulsed response in figure 2.14, the current leads the acoustic signal for all frequencies though the phase shift between them is inconsistent. Again, this is contrary to the relationship presented by Ingard in equation 1.2 which would result in a constant phase shift between the pressure and the modulating current. The measured results imply that the response of the plasma is more complicated than a general approach used by Ingard and that the kinetic processes within the plasma have a frequency dependent element associated with them. This will be returned to in a future chapter.

2.7 Summary

This chapter described an RF plasma generated in atmospheric pressure air and which acts as a sound source when the current is modulated. A number of acoustic characteristics and electrical properties have been presented and show the plasma to behave as a uniform radiator when measured in the far field. For a modulation depth of 10 % on a conduction current amplitude of 25 mA, the measured sound pressure level is 67 dB at 3 kHz with distortion levels lying above the generally accepted limit of 1% with a maximum value of 4% determined. However, the distortion determined from the acoustic signal appears to follow the distortion determined from the modulating conduction

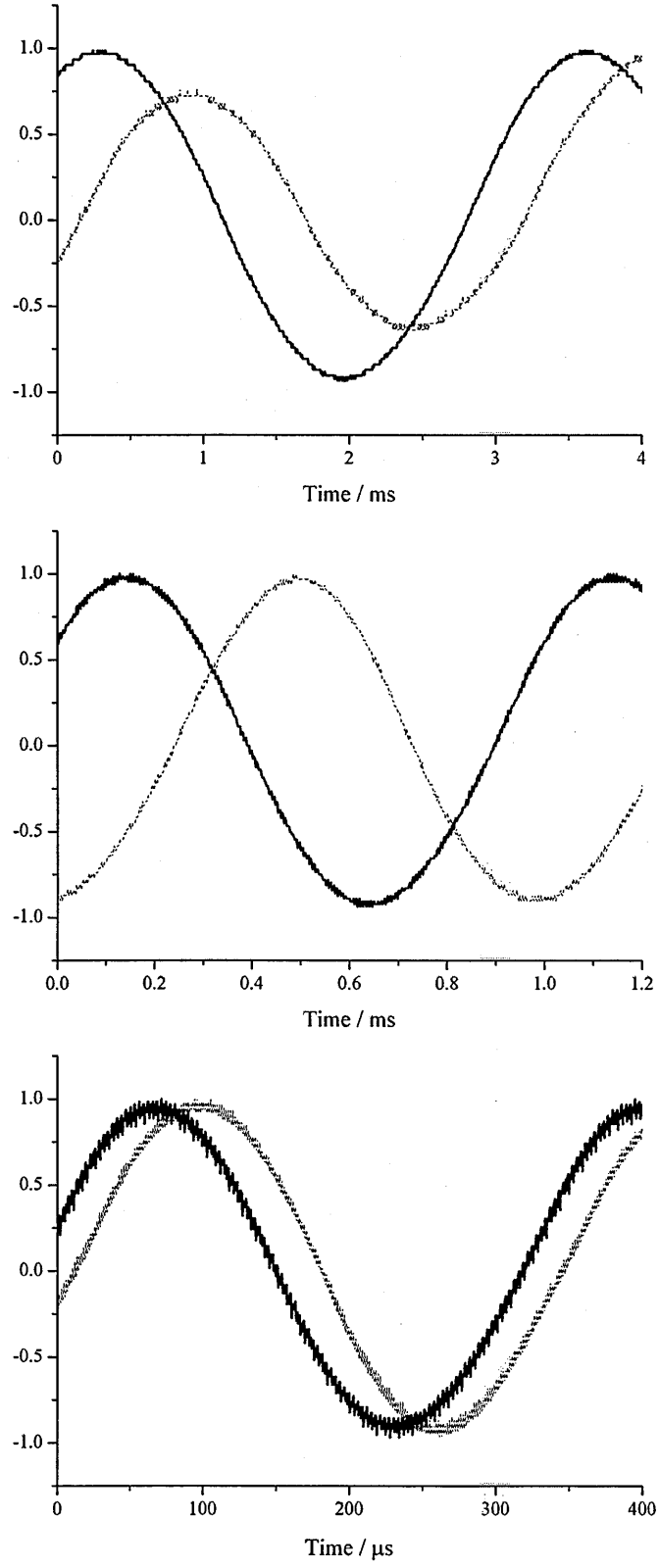

Figure 2.24: The phase relationship between the acoustic (dashed) and current (solid) signals for a modulation frequency of 300 Hz (top), 1kHz (middle) and 3 kHz (bottom).

current and reducing this may be one method of controlling the signal quality. Varying the electrode separation, and therefore the plasma size, also has influence on the SPL. However, the frequency response shows limited bandwidth with the SPL dropping off from around 3 kHz; this effect has been well documented in other plasma sources and is a result of the mechanical limitations due to the plasma's size and from the properties of the plasma itself. Both pulsed and continuous signals identify a delay between the input modulating conduction current and the output acoustic signal though this is inconsistent with previous theoretical explanations and requires a more detailed approach that includes frequency dependence. The coupling mechanism between electrical and acoustic components is explored in the next chapter.

Chapter 3

Steady-state characteristics of the plasma

3.1 Introduction

The acoustic characteristics of the plasma presented in the previous chapter give a feel for its capability as a sound source. While an elementary understanding has been gained regarding the relationship between the input electrical signal and output acoustic signal, the intermediate transduction mechanism can only be properly understood by measuring the plasma processes that cause the energy conversion. This chapter describes the measurement of several key plasma characteristics that provide a basis for explaining electro-acoustic coupling. The development and validation of the experimental systems used to measure these characteristics are also discussed.

3.2 Background

The investigation into how a plasma emits sounds begins with understanding the processes occuring within the plasma itself. As described in the introductory chapter, the basic mechanism involves expansion of the gas column in response to a significant energy input. Therefore, a quantitative assessment of the dimensional and gas temperature variations should provide a direct measure of this effect. To do this, non-invasive methods should be employed to avoid electrical and acoustical perturbations. The

optical emission of the plasma provides a good source of information on a number of discharge characteristics.

Aside from their sound generating capabilities, atmospheric pressure air plasmas are finding an increasing number of uses in a wide range of industrial and bio-medical applications. Operation at atmospheric pressure eliminates the need for vacuum systems but the plasma becomes more susceptible to instabilities that lead to arc formation; the main cause of instability is increasing current density which, if not controlled through suitable driving conditions, leads to a near thermal equilibrium plasma as used in welding. Using air eliminates the need for specific gas supplies but results in the production of additional molecular species from nitrogen and oxygen. This may be beneficial or a hindrance, depending on the application. In addition, higher breakdown and sustaining voltages are required for air than say for atomic species.

A common method for determining the temperatures in an air plasma is through measurement of the spectral emission of the so-called nitrogen second positive system. The fast relaxation time between rotational and translational stages in molecular nitrogen means that the rotational temperature can be taken to represent the kinetic gas temperature [37]. The rotational temperature is obtained through fitting of a modelled rotational line emission to that measured. Spectroscopy can also identify the various species that are formed in the plasma. Another useful parameter that can be obtained from the nitrogen spectrum is the vibrational temperature. Generally in molecular gases, the dominant gas heating mechanism occurs through electron excitation of the vibrational states followed by relaxation to the translational state [31] and in an air plasma this occurs almost exclusively through nitrogen [37]. Although this will be of more significance in the results for the plasma under modulation, this temperature provides a measure of the energy available for a number of chemical processes within the plasma. Comparing the temperatures in a plasma gives an indication of its state of equilibrium. Differences between the electronic, vibrational, rotational and translational temperatures are typical of a non-thermal, cold plasma whereas more equal temperatures are characteristic of a thermal arc plasma.

The measurements that are presented in this chapter focus on the characteristics of

the plasma while operated in its unmodulated 'steady-state'. The non-invasive method of spectroscopy and a more conventional optical set-up will be used to measure both the plasma temperatures and the dimensional changes in the plasma, which in turn will give an understanding of their influence on the sound emission (as well as establishing the plasma's properties in relation to other atmospheric pressure air plasmas).

3.3 Experimental set-up and procedure

The experimental set-ups used for measuring the discharge characteristics are described in this section. In addition to measurements of the plasma characteristics, a numerical model, adapted from one designed to predict the characteristics of a DC glow arc, is introduced. The model results are validated against the experimental data and assist in understanding the processes occurring within the plasma.

3.3.1 Gas temperatures

The rotational and vibrational temperatures of the plasma can be determined from the spectral emission of the nitrogen second positive system (N_2SP) between 300 to 400 nm. The intensity of the rotational line structure in a spectrum is directly proportional to the rotational temperature. Meanwhile, the vibrational temperature can be calculated from the relative intensities of two separate vibrational band transitions from within the system. In order to carry out the measurements presented here, the plasma was imaged using two spectrometer systems. The first system used was an OceanOptics HR4000 spectrometer fitted with a fibre optic and 5 mm diameter collimating lens to image the region of the plasma onto the entrance slit. The grating resolution of this system is 2400 lines/mm and the entrance slit width is 6 μm. Although a direct measurement of the spatial resolution was not made at the time, a measurement made subsequently with a comparable fibre optic set-up showed that, for a 40 mm separation between the fibre optic and plasma, the fibre optic acquired light from a cylindrical chord that is approximately 1 mm in diameter. The axial and current dependent measurements of the temperature were made using this system. The second system used was a Triax HR320 monochromator coupled with an Andor DH534 iCCD camera

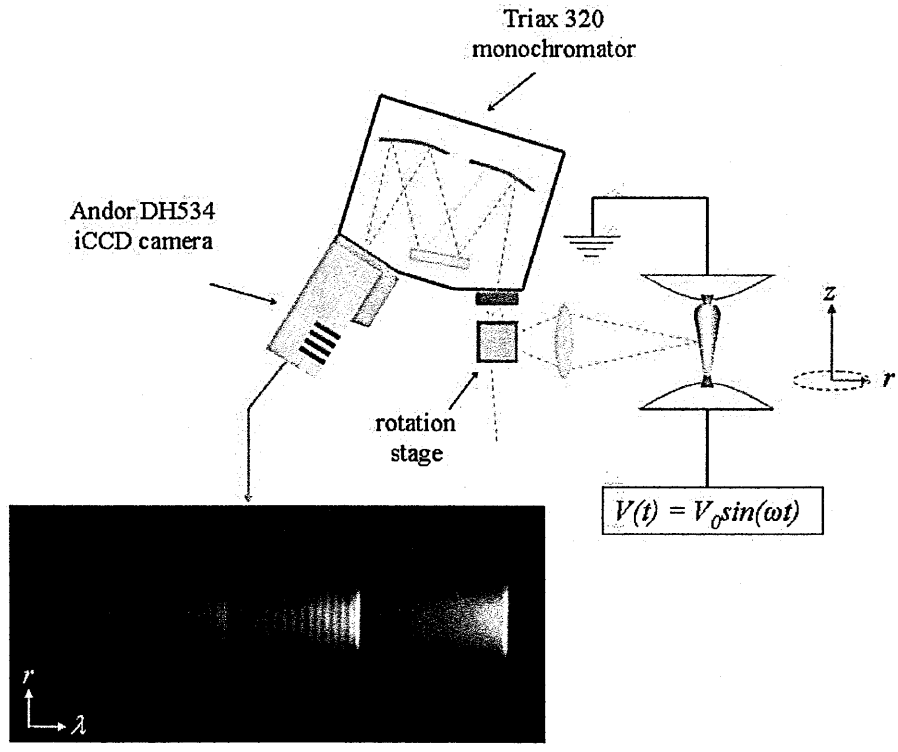

Figure 3.1: The Triax HR320 monochromator and Andor iCCD camera set up for measurement of the radial distribution of spectral intensity.

(figure 3.1). The monochromator is a Czerny-Turner double pass type with a path length between entrance and exit slits of 320 mm. Light is imaged onto an entrance slit of width 0.15 mm using a 50 mm diameter bi-convex lens of focal length 75 mm which is optimised for UV transmission. Between the lens and entrance slit, a dual mirror arrangement is positioned in order to rotate the image by 90° to enable the intensity in the radial direction to be captured. The light incident on the entrance slit is dispersed with an 1800 lines/mm grating. The linear dispersion of the monochromator, calculated from the path length and the wavelength of interest, is around 1.5 nm/mm of the CCD array length. The algorithm used to calculate the temperatures does not require a slit function input to account for the spectral line broadening but, for reference, measurement through imaging the emission of a green laser gives a nominally trapezoidal slit function with a full-width, half-maximum (FWHM) of around 0.25 nm; the convolution of the entrance slit width and the CCD pixel width produces a similar value. Additional broadening effects of the plasma have been found to be negligible relative to the spectrometer response and therefore it is not necessary to apply

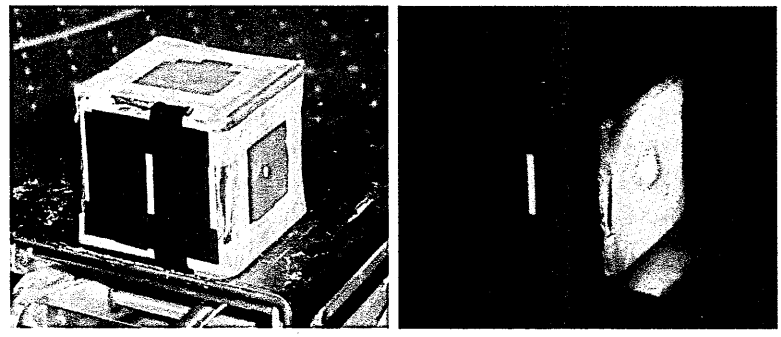

Figure 3.2: The light box used to determine the spatial resolution of the monochromator.

additional compensation. During setting up, the external optics and monochromator are aligned using a laser. The Tesla coil is mounted on a vertical travel stage to adjust the axial position and is accurate to within $\pm$ 0.2 mm. The monochromator and camera set-up is calibrated using a white light source of known power output between 300-800 nm and corrections are applied to the spectral line intensity in order to compensate for the wavelength dependence on the quantum efficiency of the camera CCD. Additionally, a flat-field correction and a background correction is applied to the data to correct for variations in pixel sensitivity of the CCD array; the flat-field data set used for correction was acquired by uniformly illuminating the CCD array with a white light source and making a pixel by pixel correction for the variation in pixel sensitivity of the array. Measurement of the background light levels was taken after the monochromator was set-up with all optics but with no spectrum from the plasma present. Measurements of the UV radial intensity and the on-axis spectral scans were made using this system.

For the measurements presented in this chapter, the spatial resolution in the radial direction was calibrated by imaging a source of known dimensions onto the entrance slit. This source was a light box constructed from six square light diffusing plates with a 1 mm diameter input aperture on one side through which a 532 nm green laser was incident (figure 3.2). The multiple internal reflections produce a near-uniform illumination across the exit aperture. During calibration, the aperture was placed at the same position as the plasma and was imaged onto the entrance slit using the rotating optical set-up. Using this method, the spatial resolution in the radial direction was found to be approximately 13 μm/pixel with an accuracy of 0.5 μm/pixel, as

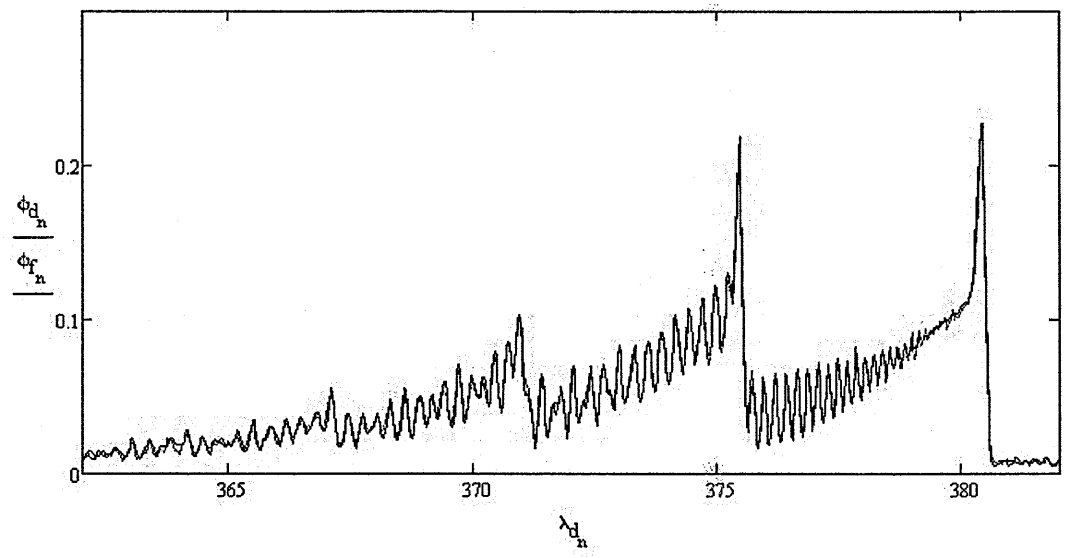

Figure 3.3: The measured (red) and modelled spectrum (blues) for an rms conduction current of 11 mA. A nominal intensity is given as a function of wavelength.

determined from repeat measurements.

The rotational and vibrational temperatures are determined by fitting a modelled spectrum to the measured emission spectrum (figure 3.3). The modelled spectrum is calculated in Mathcad using the Genfit function which applies a Levenberg-Marquardt (L-M) algorithm to calculate the expected spectral line intensity for a given temperature. The function calculates the multiplet splitting of the P, Q and R branches in nitrogen using the rotational terms via the formula from Herzberg [38] with rotational constants taken from Lofthus [39]. For the line intensity, the transition probabilities between $C^3\Pi_g$-$B^3\Pi_u$ electronic states are taken from Hartmann [40] along with the relevant Honl-London factors, again from Herzberg [38]. The modelled spectrum was calculated for the spectral emission lines of the $\Delta v = 2$ transition, with the relative intensities of the 0-2 (380.5 nm) and 1-3 (375.5 nm) band transitions used to determine the vibrational temperature. Prior to the spectral fitting procedure, corrections were applied for inaccuracies of the wavelength assigned to a data set by the measurement acquisition system through an addition pre-analysis program written in MathCad. The fitting function uses four free parameters to fit the modelled spectrum; rotational temperature, vibrational temperature, the background emission level and the N_2C excited state population which is used as a relative measure of the emission intensity. Both

temperatures are determined from the relative intensities of the rotational lines and the vibrational band transitions and are independent of the N_2C population which is itself determined from the spectral line intensity; the line intensity is proportional to the photons detected by the CCD which in turn is dependent on the acquisition timings used. The function optimises the slit function from an initial value to account for spectral line broadening and benefits from greater accuracy in terms of the fitting to measured data. However it is at present optimised for one transition band of the nitrogen system. The function was validated against Specair [41] and against an independently developed fitting algorithm using the Levenberg-Marquardt method [42], the results of which showed an average difference of around 7 % in the calculated rotational temperature when a common test spectrum is analysed. This value has been applied as an uncertainty.

3.3.2 Discharge radius

The discharge radius can be calculated from the optical emissions in various wavelength regions of the plasma. The N_2SP spectrum, used previously for determining the gas temperatures, was further utilised to calculate the radial profile of the UV emission. For a spectrum (such as that in figure 3.1), the intensity of the band transition was integrated along the wavelength axis to give the total intensity of the emission as a function of radius. The half-width, half-maximum (HWHM) of the intensity profile was then calculated and taken as representative of the discharge radius.

The discharge radius was also determined from the visible emission over the wavelength range 400-750 nm. The plasma was imaged with the Andor camera fitted with an optical system typically used for close-up photography (figure 3.4). The optical system consisted of a Tokina 70-200 mm zoom lens combined with a +4 diopter attachment to increase magnification. This combination results in loss of sharpness in the image due to a reduced depth of field so, for accurate imaging, this needed to exceed the dimensions of the plasma. With a lens stop of f/22, the depth of field was measured as approximately 15 mm and therefore adequately larger than the diameter of the plasma being imaged. By imaging a ruler with 1 mm spacings, the spatial res-

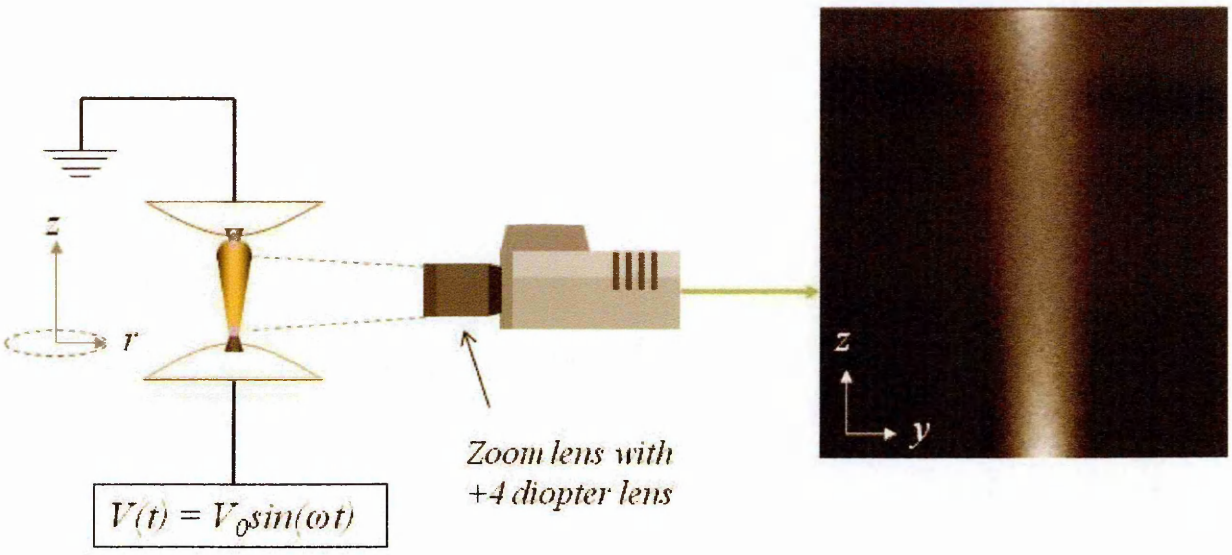

Figure 3.4: The setup for measurement of the visible optical emission using the Andor camera.

olution was determined to be 15 μm/pixel. As with the analysis of a N_2SP spectrum, the HWHM of the intensity extracted from the image was taken as the discharge radius (figure 3.5). Each profile was averaged with the adjacent 10 profiles along the vertical z-axis, limiting the spatial resolution in this direction to approximately 150 μm.

3.3.3 Numerical model

The model employed to predict the behaviour of the plasma under investigation (that is the stationary RF discharge stabilised by natural convection) is an adaptation of one previously developed by Prof. George Naidis of the Institute for High Temperature, Moscow. The modelling was conducted by Prof. Naidis in collaboration with the author; the rms conduction current was taken as the equivalent DC current and used as the input parameter for the model calculations. The original configuration is for a convection stabilised DC discharge with vertical and axial symmetry [43, 44]. The model is 'absolute' in that it is independent of any measured values. A full description of the model is given in Appendix D and a summary of the key features is given here. The adaptation to an RF excited plasma is done on the basis of an equivalent rms current input and averaging of the rate constants of reactions involving electrons (such as ionisation, dissociation, excitation and recombination) over the RF period [45].

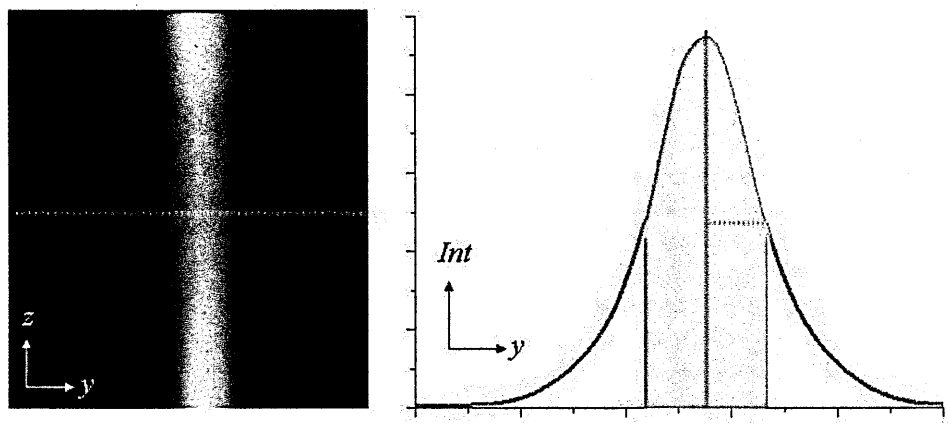

Figure 3.5: The HWHM of an intensity profile is taken as the discharge radius.

The model accommodates non-equilibrium effects which include deviation of the electron energy distribution from a Maxwellian distribution, deviation of the vibrational distribution of molecules from a Boltzmann equilibrium and diffusion of the various plasma species. The distributions of the plasma parameters along the radial and axial coordinates are governed by a system of equations involving Ohm's law, the mass continuity equations and the axial and radial momentum balance equations. These balance equations account for the variation in gas temperature through joule heating, radial thermal conduction and vibrational to translational (V-T) relaxation of N_2 molecules. They also account for the fractional energy transfer that contributes to gas heating and vibrational excitation of N_2 molecules. All the kinetic processes in the discharge are calculated, and balance equations are solved, for multiple atomic and molecular species associated with an air plasma.

In order to compare measurements of the discharge radius, the nitrogen first positive system (N_2FP) emission was calculated through the direct electron excitation to the $B^3\Pi_g$ state from the ground state and compared with the measured radius calculated from the visible emission. Similarly, the measured UV emission has been compared with the calculated emission of the N_2SP system through electron excitation from ground state to the $C^3\Pi_g$. In both cases, the radial distribution of electron density used to model the excitation rate and populations of the excited states is the same as that used to calculate the electric field.

3.4 Results and discussion

The discharge characteristic measurements are presented in this section. In addition to the plasma temperatures and the radii, the electrical characteristics that were introduced in the previous chapter are discussed further. The measured parameters are compared with results obtained from the previously introduced numerical model and their significance is discussed.

3.4.1 Electrical characteristics

The V-I curve presented in figure 2.3 shows similar characteristics to that of the glow-to-arc transition region of a dc glow discharge. Examining the time varying voltage and conduction current waveforms provides further information on the nature of the plasma; figure 3.6 (top) gives the waveforms for an rms conduction current of 18 mA. The trend shows that, though both waveforms are in phase as expected, the current does not follow the voltage around the maxima and minima, indicating a limiting effect on the current flow. The asymmetry between the maxima and minima of the current waveform occurs due to the vertical orientation of the plasma. Owing to convection, a hotter region forms around the top electrode, influencing the current flow. An equivalent measurement, where the electrodes are positioned in a horizontal orientation to make the thermal conditions around the electrode nominally equal, shows that although a constraining effect on the current is still present, the asymmetry between the maxima and minima is much reduced (figure 3.6 - bottom).

The electric field, E, is significant due to its influence on the rate constants used in determining electron (and other species) production. A direct measurement of this using an invasive method such as a Langmuir probe is difficult due to the high kinetic gas temperatures (to be established later) and the highly collisional environment of an atmospheric pressure plasma. Consequently, the electric field was determined by measuring the driving voltage for a 15 mm electrode separation at several conduction current settings. The model neglects the effects of cathode fall regions around the electrode and so, for a direct comparison, the drop across the electrodes in the measured results has also been neglected. To determine this, the driving voltage was measured for

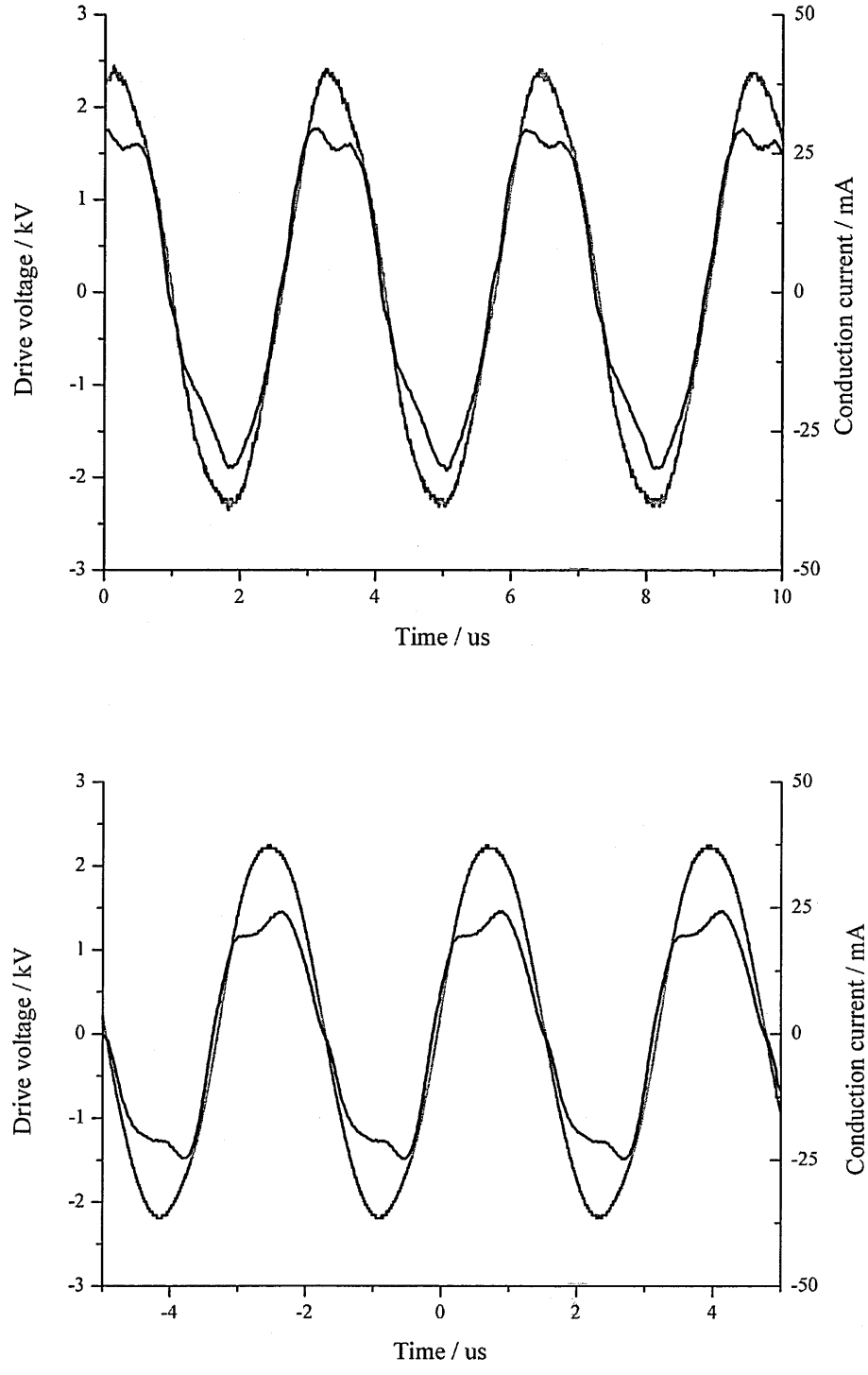

Figure 3.6: The voltage (grey) and conduction current (black) waveforms for a rms conduction current of 18 mA; upper and lower plots show the waveforms for vertical and horizontal electrode orientations respectively.

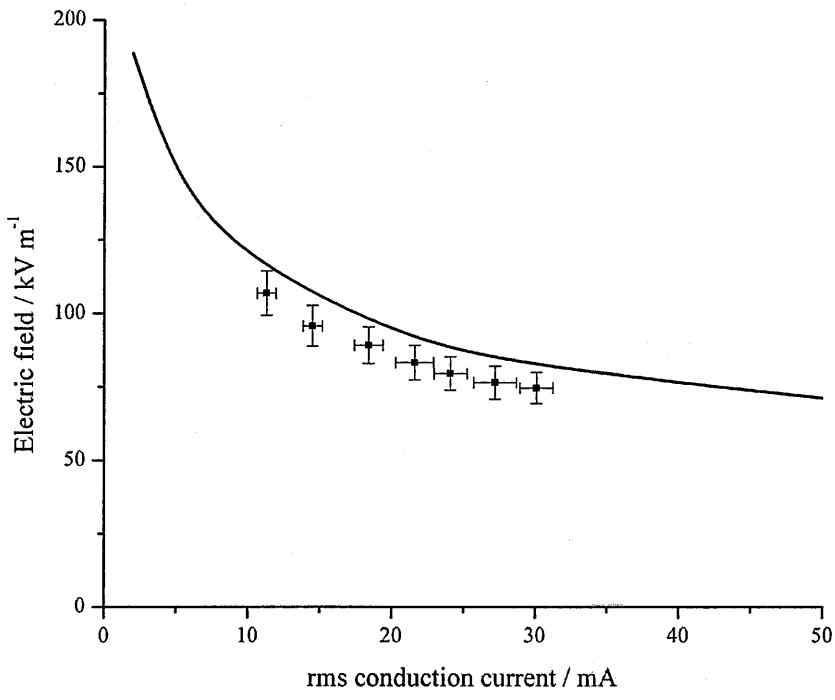

Figure 3.7: The measured (points) and modelled (line) electric field as a function of the rms conduction current for a 15 mm electrode separation.

several electrode separations and a linear extrapolation back to $z = 0$ mm completed to give the voltage drop attributed to the electrode region; this was determined to be approximately 400 V_{p-p}. Figure 3.7 compares measurements of electric field with the modelled values. Examination of figure 3.7 shows that the modelled values lie marginally above, but very close to, the uncertainty of the measured values with both following a near parallel decreasing trend over a range of rms conduction currents. While the overestimation of the modelled values is not severe, it may have further impact on the calculation of other plasma parameters (as the electric field is used to determine the rate constants required in the calculations).

Other information about the plasma can be gained from the electrical values. An approximate global value for the plasma conductivity, σ, can be calculated from,

$$\sigma = \frac{I}{V}\frac{l}{\pi r^2} \tag{3.1}$$

where I is the rms conduction current, V is the rms driving voltage, l is the plasma length (15 mm) and r is the discharge radius [46]. This calculation is simplified in that it assumes the discharge radius is constant as a function of axial position; this will be shown to be inaccurate in the evaluation of the discharge radius. Despite this, when an average radius (calculated from discrete measurements made along the vertical axis) is used, the calculated conductance is comparable to that known for a typical atmospheric pressure air plasma [32]. The value for the conductivity can be used to give a rough approximation of the electron number density, n_e, as follows,

$$n_e = \frac{\sigma m_e \nu}{e^2} \tag{3.2}$$

where e is the magnitude of the electron charge, m_e is the electron mass and ν is the electron collision frequency [47]. Again, the calculation is simplified by taking an estimate of the electron collision frequency from $\nu = v n_g \sigma_N$ where the gas density, n_g, is calculated for atmospheric pressure air using the ideal gas law and the average drift velocity, v, and molecular nitrogen cross-section, σ_N, are calculated from reference values (using a typical average electron energy of 1 eV for an atmospheric pressure air plasma operated under similar driving conditions) [32, 48]. For a rms conduction current of 11 mA, the global electron number density is approximately $2.4\text{x}10^{17}$ m^{-3} which compares well with an equivalent DC driven plasma [49]. The averaged result obtained from the model is approximately $3\text{x}10^{17}$ m^{-3}, comparable to that measured.

The power dissipated by the plasma as a function of the rms conduction current is given in figure 3.8 and varies from 18 W at the lowest measured current up to 34 W at the highest. The expected relationship of $P \propto I^2$ is not followed here due to a varying resistance across the plasma. The efficiency of the system can be calculated for the current range used for measurement. Through determining the total power dissipated in the Tesla coil (summed from the DC input from the power supply and that used to drive the active chopping circuit), the efficiency in power transfer is found to be approximately 65 %.

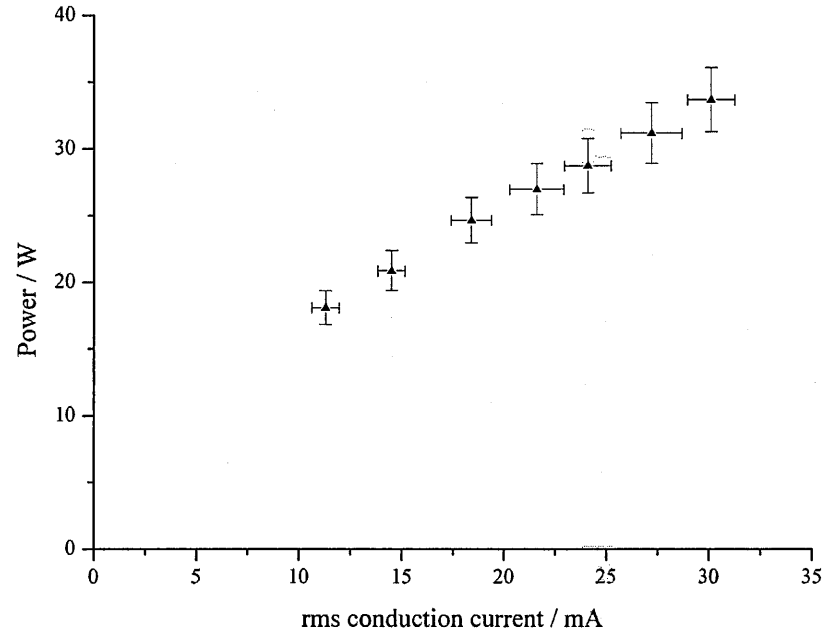

Figure 3.8: The power dissipated in the plasma as a function of the rms conduction current.

3.4.2 Spectral emission

Figure 3.9 presents emission spectra for wavelengths between 200 nm and 850 nm. The spectra are acquired at two axial positions - at the electrode region ($z = 0$ mm) and in the main body ($z = 6$ mm) - and for two rms conduction current settings. Each spectrum is corrected for the wavelength dependence of the pixels of the CCD. Also, for wavelengths greater than 450 nm, a high-pass filter was used to eliminate the second order spectral line (mainly from N_2SP emission), with a correction applied for the attenuation of spectral intensity during insertion.

The dominant feature at both axial positions is the N_2SP system between 300-400 nm. At the electrode, the nitrogen first negative system (N_2^+FN) and several atomic species such as argon, oxygen and nitrogen are also measured. This indicates the electrode region to be a rich source of high energy electrons, due to the electron energies needed to instigate the excitation and molecular dissociation required to produce these emissions. Generally, N_2^+FN emission involves an initial ionisation of the nitrogen molecule where the electron energy required is around 15.6 eV. This is followed by excitation to the $B^3\Pi_g$ excited state of the formed nitrogen ion, after which optical

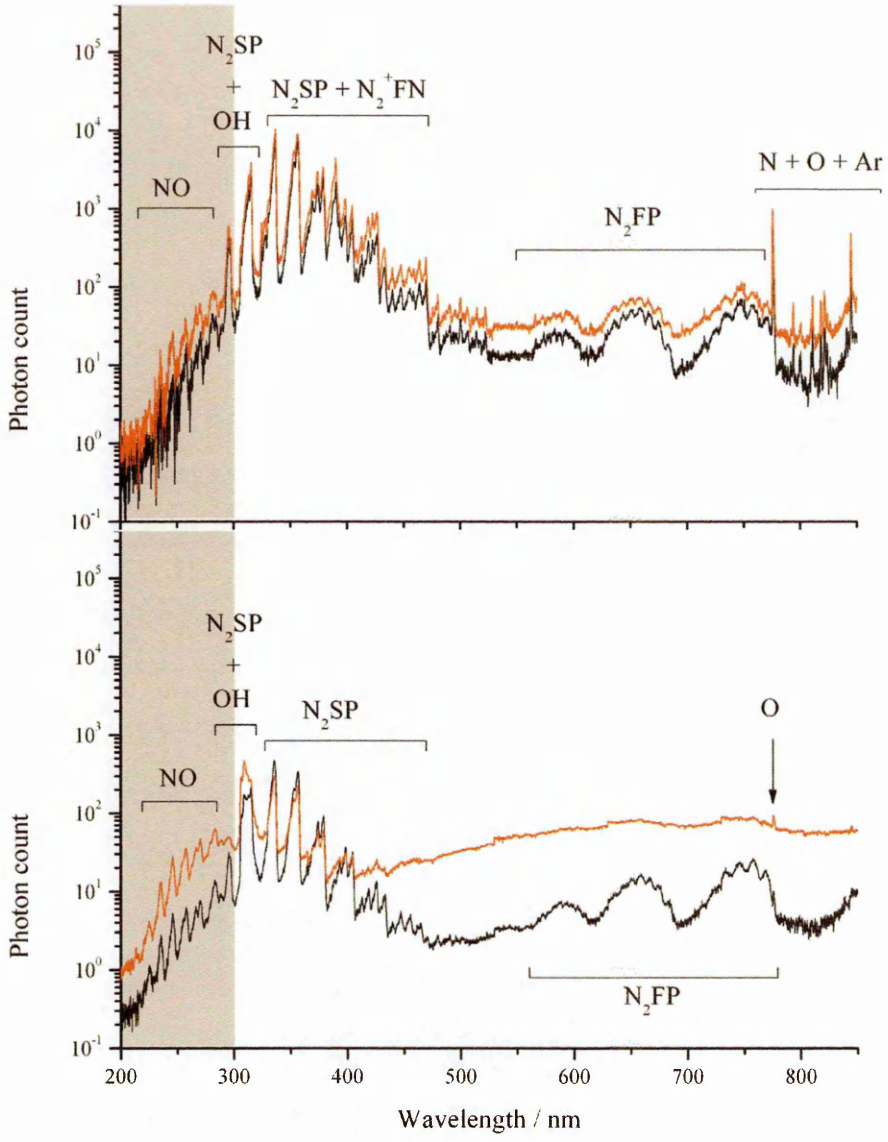

Figure 3.9: Spectral scans (on-axis) over 200-850 nm at two axial positions, $z = 0$ mm (top) and $z = 6$ mm (bottom), and at rms conduction currents of 11 mA (black) and 27 mA (red).

emission occurs through relaxation [38]. Similarly, the energies needed to produce the atomic species through dissociation must exceed 7 eV for oxygen molecules and 12 eV for nitrogen molecules [38]. The steep potential gradients in the cathode fall region around the electrodes produce the higher energy electrons in sufficient numbers to induce these processes. The visible emission consists of the upper wavelength range of N_2SP (375-400 nm) along with the nitrogen first positive system (N_2FP) [50, 51, 52]. The appearance of the hydroxide molecule (OH), which overlaps the $v = 1$-0 N_2SP transition between 300-315 nm, most likely results from the dissociation of water vapour in air. For clarity, the relative humidity in the laboratory for these measurements was

19%; a relative humidity of 57% results in the appearance of atomic hydrogen at 656 nm. At the electrode, an increase in current results in a near-uniform increase in intensity across the entire spectrum.

The spectrum at $z = 6$ mm can be compared with that around the electrode. At the lower current setting, the spectral intensity follows that of the electrode region albeit being an order of magnitude less. The absence of the atomic and N_2FN emission lines indicates that the average electron energy is significantly lower in the column. The N_2SP system still dominates with clearly defined visible emission from this and N_2FP. As the rms conduction current is increased to 27 mA, however, the relative intensities of the spectrum change. The intensity of the nitrous oxide system ($NO\gamma$) around 250 nm increases, possibly from increased recombination rates between N and O atoms which are created more readily in the electrode region. The increase in OH and N_2SP intensities are more modest in comparison. The most apparent change is in the visible range. The N_2FP emission at low current evolves to a near 'continuum' emission as a result of the increase in the intensity of the rotational line emission of the N_2FP band system or further reactions originating from other emission systems in the plasma.

3.4.3 Discharge radius

Figure 3.10 shows the discharge radius as a function of axial position for three rms conduction current settings. The radius calculated from the visible emission was taken at 1 mm increments with several discrete measurements made for the UV emission. The equivalent model results for both optical regions are also presented. At 11 mA, the radii determined from the UV and visible emissions are in close agreement and show a measured steady increase with increasing axial position until eventually sharply decreasing around the top electrode. The modelled results lie within the uncertainty of the measured data in mid-region; the absence of features around the top electrode results from the configuration of the model itself. Unlike the bottom electrode, the finite diameter of the top electrode is not taken into account and therefore the model does not account for current constriction or the expected decrease of discharge radius near this electrode. When the rms conduction current is increased to 27 mA, the radius

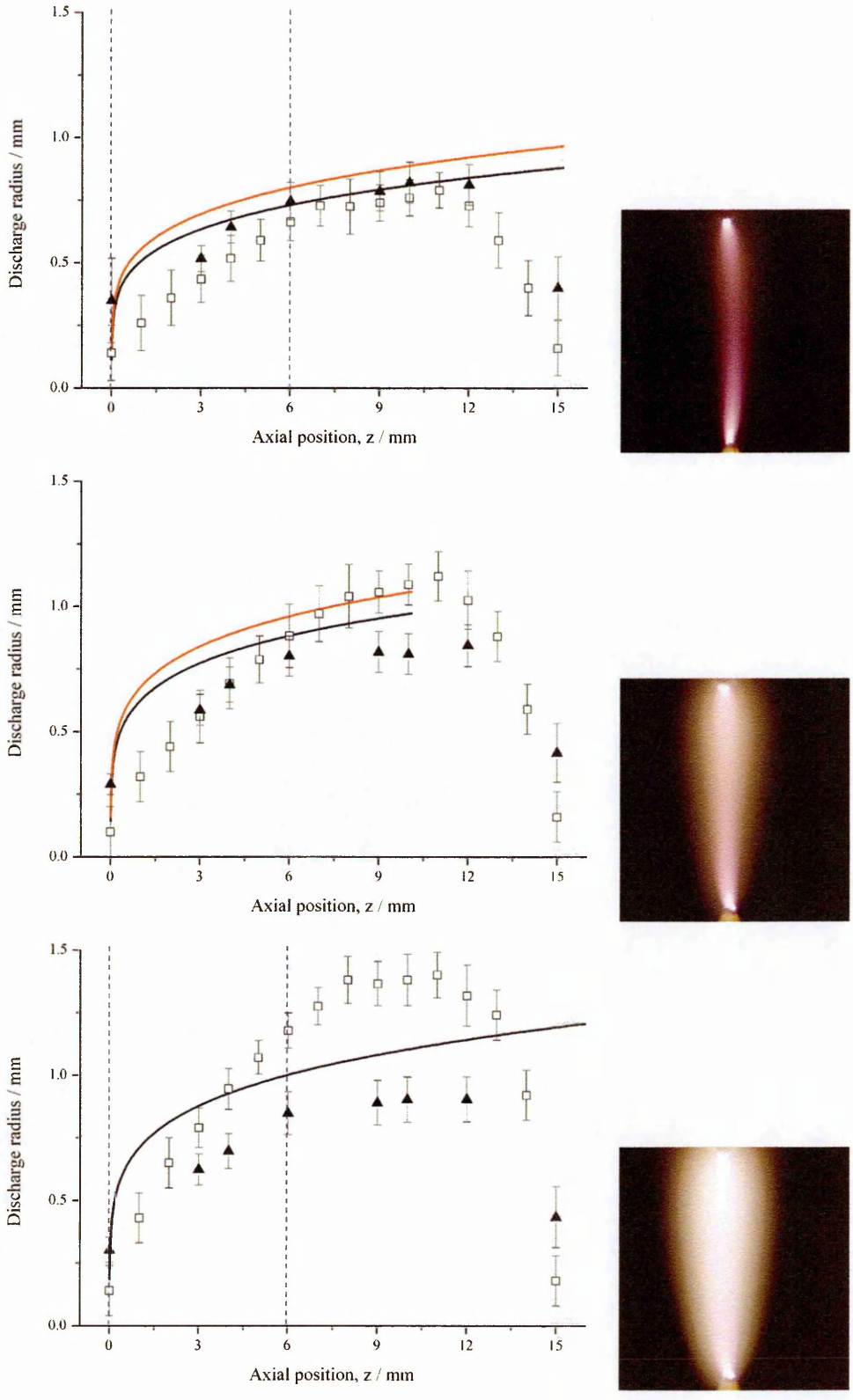

Figure 3.10: The axial variation of the discharge radius for three current setting; 11 mA (top), 18 mA (middle) and 27 mA (bottom) with corresponding images of the plasma at each setting; measured VIS (squares) and UV (triangles), modelled VIS (solid - red) and UV (solid - black).

derived from visible emission shows a significantly greater increase at all axial positions than the increase in the radius determined from UV emissions. At $z = 6$ mm, the visible emission-derived radius increases from 0.65 to 1.2 mm as the conduction current changes from 11 mA to 27 mA compared with an increase in the UV-emission derived radius from 0.75 to 0.8 mm. These different trends are also seen when the discharge radius is plotted as a function of the rms conduction current (figure 3.11). While the UV emission-derived radius shows a modest increase in line with the increasing current, the increase in the visible emission-derived radius is significantly greater; the model results lie between the two.

The plasma images alongside the axial plots in figure 3.10 give a good visual indication of the changing state of the plasma. As the conduction current increases, the previously narrow discharge, which is dominated by emission from the UV/lower visible wavelength range, develops into a source of white light emission. The increased current also broadens the plasma as a result of increased axial and radial convection and diffusion within the plasma. This change in the emission reflects the spectra of figure 3.9 and the axial positions at which the spectra were obtained are marked on the plots for the 11 and 27 mA settings.

Contrary to the assumption in the model that N_2FP emission alone is responsible for the visible emission, additional species may also contribute and can explain the differences between the modelled and measured results. The radiative lifetime of N_2FP is in the low microsecond timescale and significantly shorter than the timescales for gas diffusion (which, for molecular nitrogen, is on the millisecond timescale [35]). This means that N_2FP emission is limited spatially. An alternative path for N_2FP emission through re-excitation of the $A^3\Sigma_u^+$ to the $B^3\Pi_g$ can also be discounted as (i) higher energy electrons are still required for this process and (ii) they will not lie in sufficient number densities outside of the central ionised channel. The length scales of the radius may require reactions from long-lived metastables or other emission systems in the plasma. The formation of NO_2 fits this criterion and has been suggested previously as a possible emission source [53]. In an atmospheric pressure plasma under the electrical driving conditions considered here, NO and NO_2 species densities increase mainly from

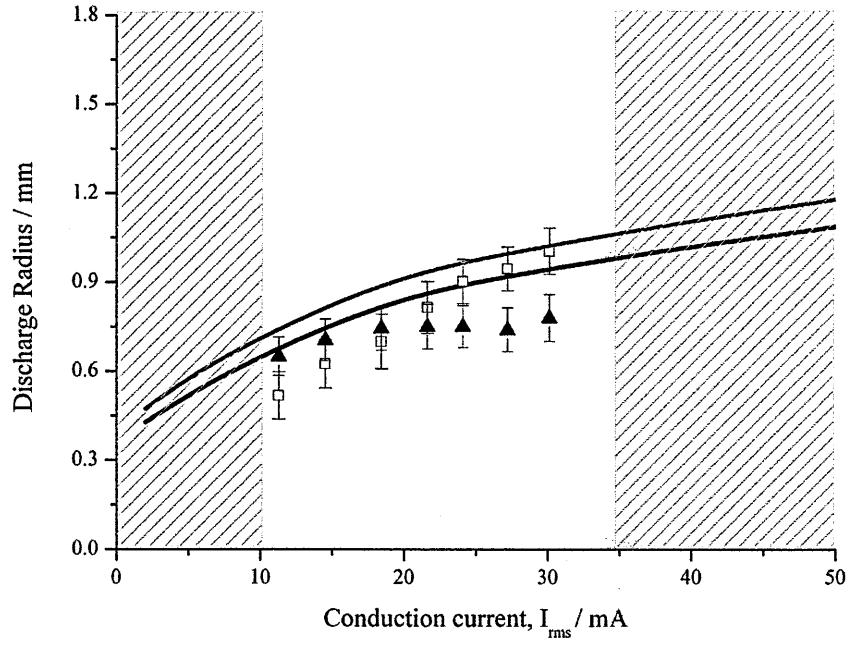

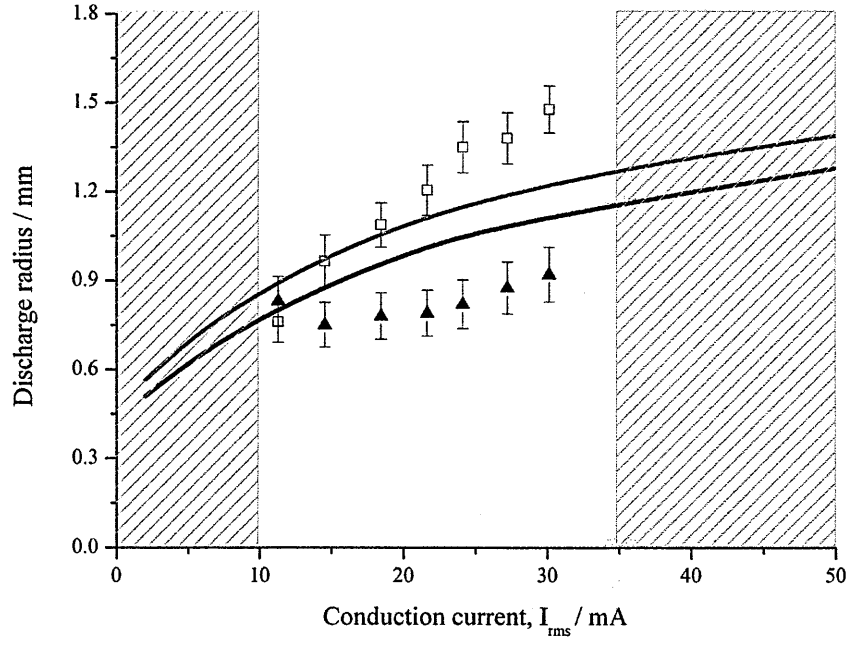

Figure 3.11: The discharge radius, R, as a function of rms conduction current evaluated at two axial distances, $z = 4$ mm and 10 mm; measured VIS (squares), measured UV (triangles) and modelled (solid).

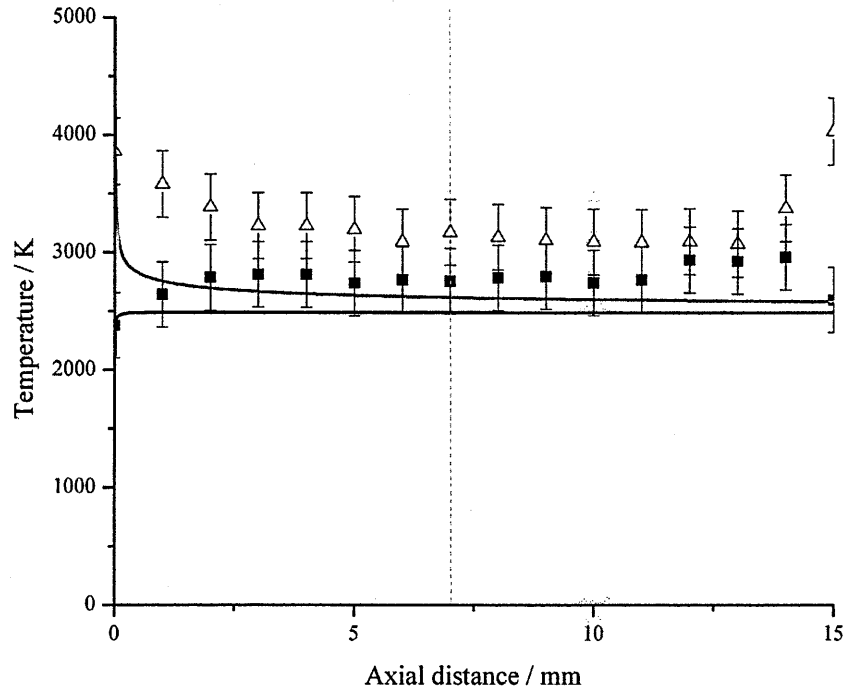

Figure 3.12: The measured rotational (squares) and vibrational temperatures (triangles) with equivalent modelled temperatures as a function of axial position, z, for an electrode separation of 15 mm and a conduction current of 11 mA_{rms} (top). The uncertainty in the axial position is $\pm$ 0.5 mm.

the recombination reactions, NO+O+M $\rightarrow$ NO_2+M and NO+O_3 $\rightarrow$ NO_2+O_2 [54]. Experimental evidence for this lies in the NOγ emission system. If the HWHM radius is determined in a similar fashion to the UV and visible emission-derived radii, it is found to be comparable to the radius derived from the visible emission and may act as the sustaining source of NO_x generation. NO is also a long lived state and may be active at the radial distances measured here. The details of the emission are of lesser importance in this project and further investigation should be undertaken where specific chemical reactions need investigating. However, the results highlight that significantly different discharge radii can be derived depending on the spectral emission region used for analysis.

3.4.4 Gas temperatures

The measured rotational (T_r) and vibrational (T_v) temperatures as a function of axial position are given in figure 3.12 for a rms conduction current of 11 mA. As with the

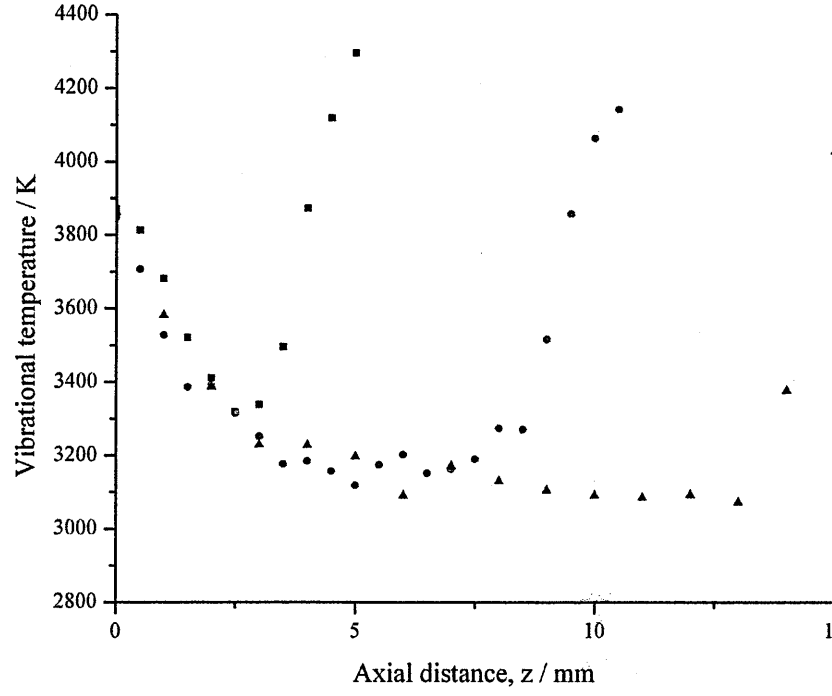

Figure 3.13: The axially-dependent vibrational temperature measured for electrode separations of 5 mm (square), 10 mm (circle) and 15 mm (triangle).

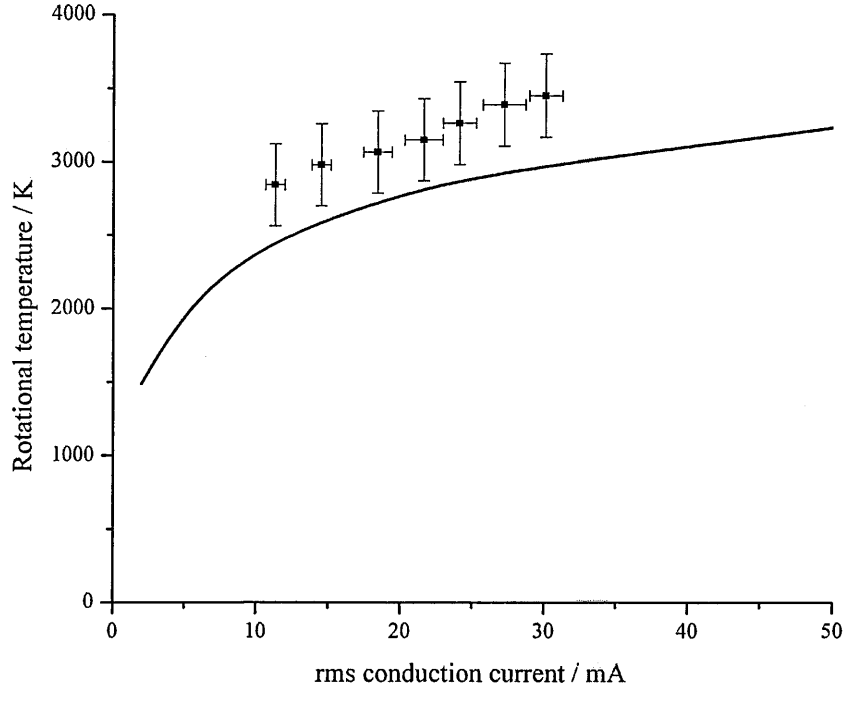

Figure 3.14: The comparison of measured (diamonds) and modelled (solid) rotational temperatures for a conduction current range of 11-30 mA_{rms} at an axial position of z = 7 mm.

discharge radius, the trend on-axis shows two distinct regions forming. Around the electrode, T_r and T_v gradually deviate from each other, indicating that they are not in equilibrium. The temperatures in the main body are more closely coupled and in near thermal equilibrium. T_r ranges from 2300 K to 3000 K and, if taken as being representative of the kinetic gas temperature (T_g), indicates that the plasma can be classified as a warm plasma, but with a lower temperature than expected for the local thermodynamic equilibrium conditions of an arc (where T_g can be in excess of 10000 K). The corresponding T_v decreases from 4000 K to 3200 K so both temperature ranges lie in the region of that measured for equivalent DC driven plasma [49, 55]. The increase in the T_v around the electrode is due to the molecular nitrogen's dependence on the rate of electron impact excitation of the internal vibrational states. The higher electron density leads to an increased collision frequency, increased excitation and hence higher temperatures. The combination of the steep potential gradients and narrowing discharge radius leads to an increase in the electron number density and provides the necessary conditions for the increased T_v around the electrodes. Comparative measurements at three electrode separations show that the T_v profile remains constant around the electrode regions (figure 3.13). A direct relationship can be established between the electric field, E, and the electron collision frequency via the electron energy distribution. It may be possible for the T_v profile to be used as a non-invasive method to determine the electric field variation within the plasma. The dis-equilibrium between T_r and T_v around the electrodes results from the interdependence of the rate of vibrational to translational (V-T) relaxation and the kinetic gas temperature; an increase in gas temperature results in an exponential increase in the V-T relaxation rate [55]. Assuming T_r represents the gas temperature, as it increases so the rate at which energy is transferred the the translational state in nitrogen also increases, resulting in faster equilibrium conditions. Hence an increase in T_r will result in decrease in the T_v.

The effects of vertical convective flow, which have previously been seen in the electrical characteristics and discharge radii, can also be seen in the temperature profiles. The sharper increase in T_v around the top electrode (compared with a shallower gradient increase around the bottom electrode) coincides with an increase in T_r where a

hotter region due to convection has formed. The relative response in the two temperatures again emphasises the interdependence of V-T relaxation and T_g.

The modelled values share many features with the measured results. In the mid-region, the trend in the modelled T_r and T_v values shows close to equilibrium behaviour, albeit around 250-300 K lower than the measured values. While the differences in the central region are modest, the electrode region shows a sharper increase in the modelled values compared with the gradual increase in the measured result. As described in the experimental set-up (section 3.3.1), the spatial resolution of the fibre optic used to obtain the measured results is approximately $\pm$ 0.5 mm which is insufficent to pick out the sharp temperature increases predicted by the model. Figure 3.14 presents the dependence of T_r on the rms conduction current and shows an increase as expected with an increase in power into the plasma. The modelled results lie marginally outside of the measurement uncertainty but follow the trend in the measured results. This discrepancy may follow from the subtle differences seen previously in the electric field comparison which then influence subsequent calculations of the plasma parameters.

3.5 Discussion

The main characteristics of the plasma have been established through measurement of the optical emission. The derived rotational temperature indicates a warm plasma that shows near-equilibrium conditions to the vibrational temperature in the main body. The effects of vertical convective flow can be seen in all results. In addition, spatial variations can be seen in the discharge dimensions and the species temperatures are identified. These spatial variations provide an interesting combination of conditions which could impact on the acoustic emission when under modulation. Key to understanding the coupling mechanism is understanding the spatial and temporal variation of the plasma resulting from a periodically driven thermal expansion of the air in the plume. Unlike the fluid/structural attributes of a mechanical loudspeaker, it is difficult to define a 'boundary' between the plasma and air where the pressure wave originates. The results for the discharge radius complicate this further with two notional boundaries determined for the plasma depending on the optical region used

for analysis. Correlation between the measured and modelled vibrational temperature gives confidence that V-T relaxation is the dominant energy transfer mechanism that leads to gas heating and instigates thermal expansion. Typically, vibrational excitation in the nitrogen molecule is optimal when the electron energies are between 1-3 eV which would be present in sufficient quantities where visible emission occurs. Therefore, it is feasible that the visible emission-derived discharge radius defines the boundary where the pressure wave originates. The asymmetry of the plasma radius may lead to a more complex acoustic field in the near-field region, though this is of lesser importance to a listener as the experimental results indicate that the emission in the far-field is close to a cylindrical source and behaves as a isotropic radiator.

The axial variation of the vibrational temperature and specifically the axial dependence in the rate of V-T relaxation may lead to phase differences, spatially, in the response of the plasma to a time-varying electrical signal (and in the subsequent acoustic signal). However, V-T relaxation times calculated from the temperature results at the electrode and the main body, show a modest difference in the time constants associated with relaxation, which are on the microsecond timescale [56]. This is signifcantly shorter relative to the period of audio modulation and implies that, while a small phase difference would occur along the plasma length, the response of the human ear would not be sensitive enough to detect it. Other practical considerations when using a plasma in a domestic environment can also be addressed. Ozone generation is acknowledged to be a problem for corona-type plasmas with prolonged exposure in a confined area being hazardous to health. Ozone synthesis in air relies on a three body reaction between oxygen, diatomic oxygen and a third body. This process is significantly affected by gas temperature and humidity within the environement. The effects of temperature are twofold; firstly, NO_x production is increased at elevated gas temperatures where faster reactions between O and NO_x (NO and NO_2) use up the oxygen atoms necessary for ozone synthesis. Secondly, ozone is naturally unstable at elevated temperatures. As an example a DBD discharge operated at a gas temperature of 800 K produces a negligible level of ozone [54]. If the rotational temperature is assumed to represent the translational gas temperature in the Tesla coil plasma then ozone levels

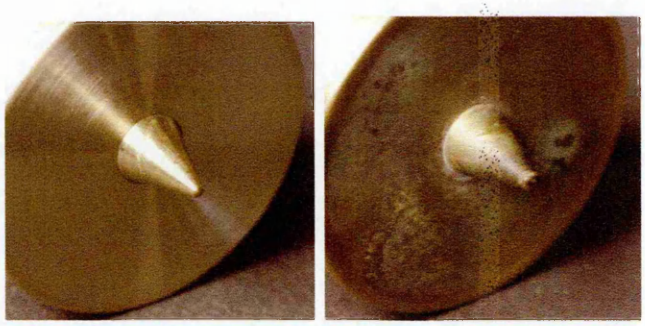

Figure 3.15: The ground electrode (left) and eroded electrode with surface damage around the electrode base (right).

would be negligible. Measurement using an ozone detector shows this to be the case with ozone levels remaining below 0.01 ppm and within workspace exposure limits [57]. The short lived nature of ozone under these conditions leads instead to increased levels of other hazardous species such as the nitrogen oxides (NO_x) identified in the spectral scan; the health implications of NO_x are well documented and further investigation is required to determine the level of generation while the plasma is operational.

One final observation is the changing condition of the electrodes with sustained use. Figure 3.15 shows before and after images of the electrodes taken at a six month interval and with an average weekly plasma operation of around 10 hours. The comparison between the before and after shot shows that the previously sharp electrode has been eroded and flattened due to multiple electrode effects such as melting from thermonic emission and ion bombardment. Although the increased surface area will increase the dimensions of the current channel, the main problems occur with breakdown of the plasma. In practice, electrodes would require regular maintenance or replacement to ensure the plasma can be ignited. During the measurements described in this thesis, the electrodes were re-ground regularly to ensure conditions were consistent throughout.

3.5.1 SPL and plasma dimensions

It was seen in the results presented in section 2.5.4 that the SPL has a dependence on the plasma dimensions. At that point, the non-cylindrical dimensions of the plasma made it difficult to calculate the surface area and relate it to the SPL but the results of the discharge radii in section 3.4.3 now make it possible to calculate this. To do

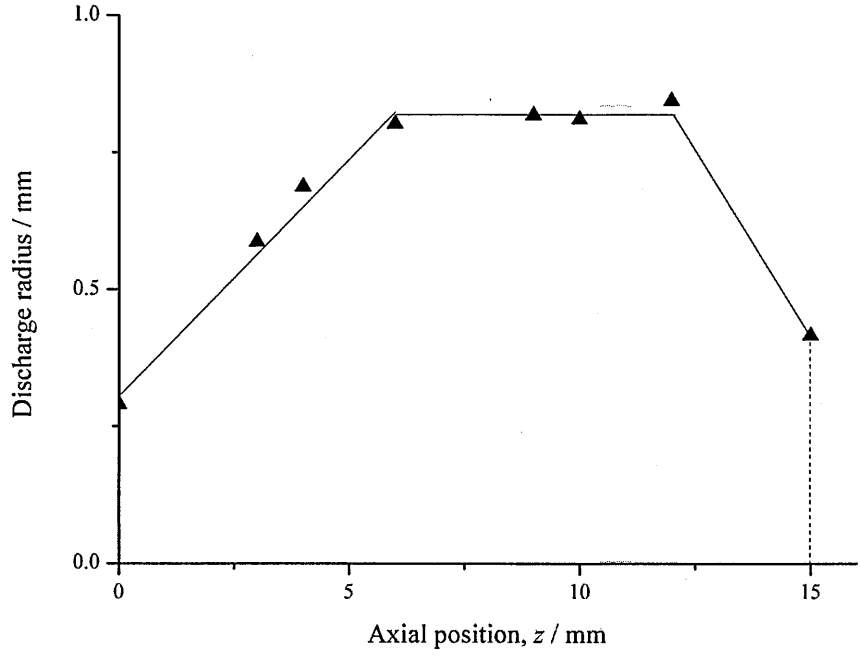

Figure 3.16: Fit to the measured UV discharge radius to calculate surface area of the plasma; $I = 18$ mA$_{rms}$.

this, lines of best fit are applied to the discharge radius profile in figure 3.10 (figure 3.16). This fit models the plasma as a combination of conical and cylindrical regions and the surface area was calculated for each using the area formulae for a cone and a cylinder. Although the discharge radii for the 5 and 10 mm electrode separations were not measured, the results for the axial variation of T_v in figure 3.13 for all three electrode separations show the consistency in the profile around the electrode regions. It has therefore been assumed that this consistency translates to other parameters such as the discharge radius. The equivalent profiles used for calculating the surface area for the 5 and 10 mm electrode separations are given in figure 3.17. The method and calculations are applied to both the UV and visible emission profiles for an rms conduction current of 18 mA, which was used for the initial measurements of electrode separation in section 2.5.4. The calculated surface areas are given in table 3.1. For

	5 mm	10 mm	15 mm
UV	18.9 mm^2	37.6 mm^2	63.3 mm^2
VIS	14.2 mm^2	34.7 mm^2	66.8 mm^2

Table 3.1: The surface area of the plasma calculated from the UV and visible discharge radii results.

the UV region, the increase in surface area that accompanies the increase in electrode

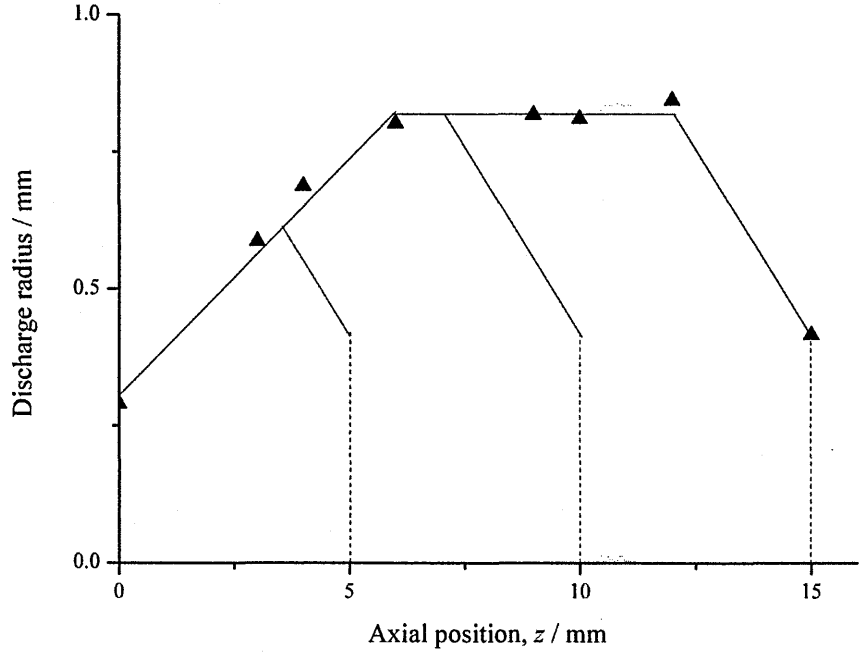

Figure 3.17: The profile used to calculate the plasma surface area for an electrode separation of 5 mm (red) and 10 mm (blue).

separation from 5 to 10 mm would be equivalent to a 6 dB increase in SPL. From 10 to 15 mm, the SPL increases by a further 4.5 dB. The equivalent increases from the visible emission are 7.7 dB for 5 to 10 mm and 5.7 dB for a change of 10 to 15 mm. For comparison, the measured differences presented in figure 2.21 show increases of approximately 10 dB and 7 dB. An additional uncertainty of $\pm$ 0.1 dB and $\pm$ 0.4 dB (based on the uncertainty associated with the discharge radius) can be applied to the UV and visible radii results respectively. The magnitude of the increase is close to the measured SPL with the results determined from the visible emission radius lying within the overall uncertainty of the measured SPL ($\pm$ 3.3 dB). The trend in the SPL differences is consistent with those measured, reflecting the greater increase between a 5 to 10 mm separation compared with a 10 to 15 mm separation as expected. The comparison with the measured SPL implies that the surface area of the plasma, particularly that defined by the visible emission, shows a close correlation with the SPL.

3.6 Summary

The characteristics of the plasma have been determined from a number of non-invasive techniques. The rotational temperature has been shown to vary between 2800-3400 K for a corresponding rms conduction current of 11-30 mA and is significantly above that expected for the cooler, corona-type discharges. The corresponding vibrational temperatures are around 3500-4000 K. Modelling shows that the temperatures, along with the electron number density and conductivity, are comparable with equivalently operated DC discharges and known reference values. The temperatures calculated using the model are comparable with those measured and give confidence that the gas heating is dominated by both joule heating and vibrational-translational relaxation of nitrogen molecules. A reasonably close agreement is seen between the modelled and observed discharge radius as a function of axial position. The spatial variation in the plasma parameters has been measured. Broadly, two regions are evident; around the electrode and in the main column. These regions are reflected in the plasma characteristics with regions of thermal and non-thermal equilibrium as well as the relative intensity changes in the spectral emission. Atomic species (O, N and Ar) and radical species (OH, NO) have been identified though some are limited spatially to the electrode region.

Chapter 4

The plasma under modulation

4.1 Introduction

The steady-state characteristics of the Tesla coil plasma were presented in the previous chapter and next, the behaviour of the plasma under modulation is investigated. The experimental methods used previously are adapted to allow phase-locked measurements to be made of the optical emission, electrical properties and species temperatures. This provides information on the behaviour of the plasma as it varies on a timescale that is slow relative to the driving RF frequency but fast compared with some of the characteristic gas dynamic processes. The correlation of these temporal measurements with each other and with the acoustic waveforms provides the first direct evidence of where the electro-acoustic coupling occurs.

4.2 Background

The results obtained with the plasma operating in its steady-state provided spatial information on the plasma as well as details of some fundamental characteristics that determine its nature. Overall, this enabled regions of thermal and non-thermal equilibrium between the vibrational (T_v) and rotational (T_r) temperatures to be identified, together with a number of molecular and atomic species that were generated through the various processes within the plasma. The close correlation between the measured and modelled results support the view that joule heating and vibrational-translational

relaxation are the dominant forms of gas heating.

While the measurements under steady-state conditions provided spatial information on the plasma characteristics, it is the temporal variation of the plasma parameters relative to the input energy that leads to sound generation. The assumption is that the dominant mechanism for sound generation is through thermally stimulated expansion and contraction of the core of the plasma plume. As with lightning, the plasma undergoes a change in its volume in response to a change in the input energy. Applying modulation on top of a steady-state current leads to additional behaviour of the plasma characteristics being revealed.

Of interest are the variations in the *amplitudes* and *phase differences* of the optical, electrical and dimensional characteristics. The various kinetic processes in the plasma will have their own excitation and relaxation times and the resulting phase differences can be used to interpret the timescales that are involved. For each characteristic, the amplitude of the variation can give insight into the coupling of the initial energy input to the output parameter. For this, the measurement techniques of the previous chapter have to be synchronised to an audio-frequency modulation.

4.3 Time-resolved investigations

For all optical emission measurements, a variable delay pulse generator provides a gated trigger signal of known width, Δt, to the camera. The pulse generator is, in turn, triggered externally by the audio signal source used to apply modulation to the DC supply into the Tesla coil (figure 4.1). The position of the delayed gate signal is adjusted so that it occurs at the time in the modulation period, T, that the acquisition is required. The interval, or step size, at which a measurement is made corresponds to a resolution of around T/10. In the experiments described here, a 3 kHz modulation signal was used. The modulation period was therefore 0.33 ms and measurements were taken at 40 μs intervals. The gate width, Δt was set to half the step size, or 20 μs, so that there was no 'overlap' between adjacent measurement steps. This method of acquisition was applied to all optical emission measurements with the measurement procedures and analysis remaining unchanged.

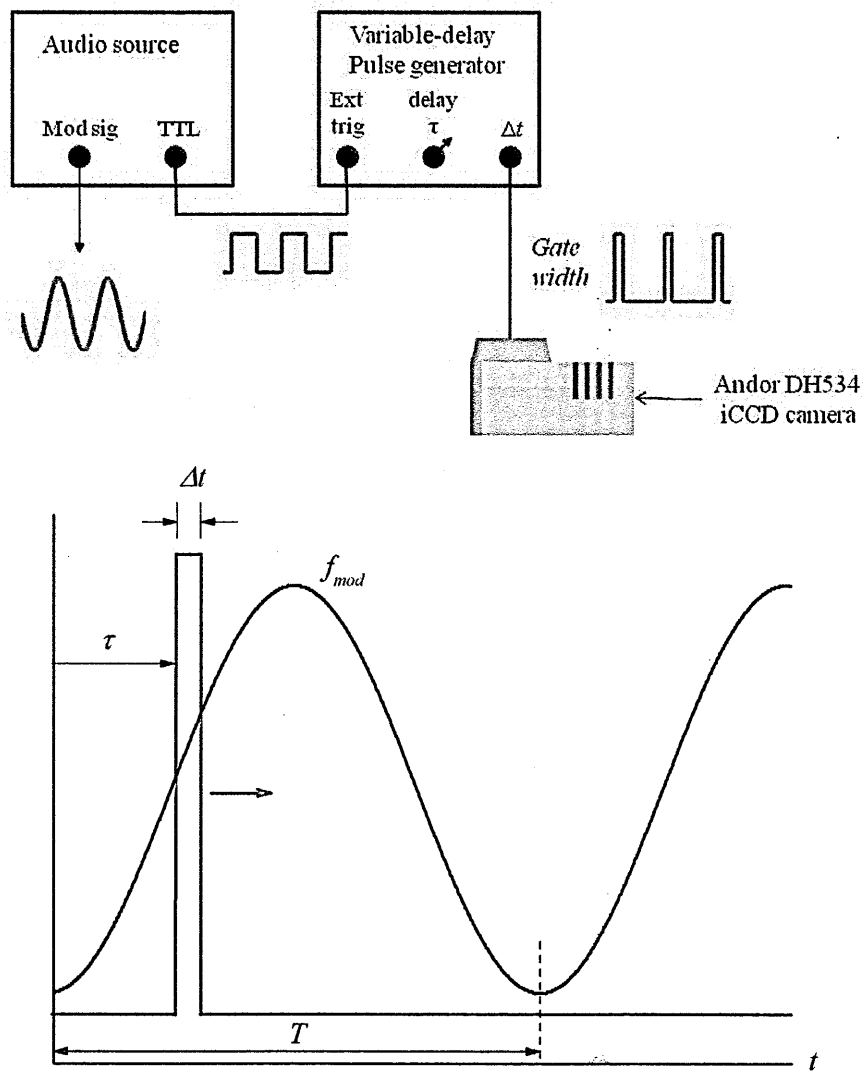

Figure 4.1: The adaptation to the experimental set-up (top) and the triggering for time-resolved measurements (bottom).

4.3.1 Optical intensity and electrical power

The measurement of the optical intensity and instantaneous electrical power are presented in this chapter. The optical intensity was used previously to determine the discharge radius from the HWHM of the line-of-sight profile (figure 3.5). The total intensity represents the light emission from the plasma in the spectral region of interest and the temporal variation shows how the relaxation of excited states varies with respect to the input electrical current. The total intensity is determined by integrating along the line-of-sight intensity profile in the direction of the y-axis for this configuration (figure 4.2). For the total intensity obtained from the UV emission, a spectrum (figure 3.1) was integrated across the entire image. Absolute values for the intensity

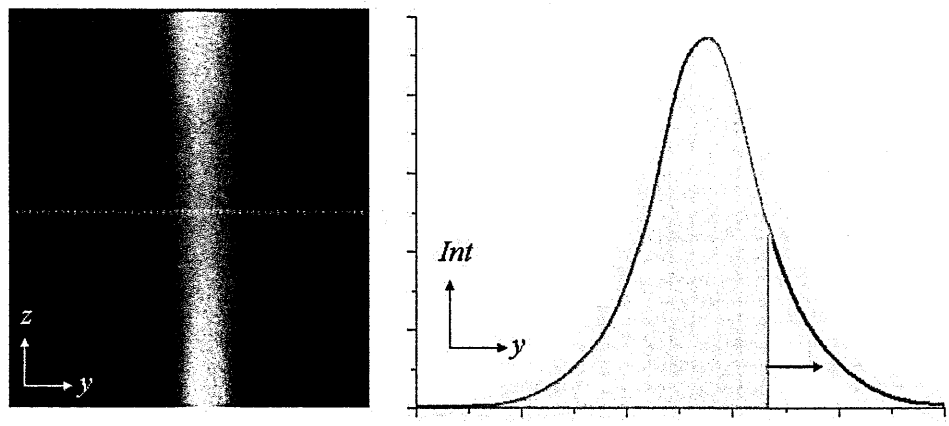

Figure 4.2: The optical intensity integrated over the line of sight intensity cross section (total visible light).

are not used in this case as this is dependent on the acquisition settings used on the Andor camera.

The instantaneous electrical power gives a measure of the energy variation over a modulation period and, just as the efficiency of the Tesla coil was calculated in section 3.4.1, the efficiency in the electric to acoustic energy conversion can also be calculated. The instantaneous power is calculated using the following equation;

$$P(t) = V(t)I(t) \tag{4.1}$$

where $V(t)$ and $I(t)$ are the time-varying amplitude of modulating voltage and conduction current components respectively.

4.3.2 Numerical model adaptations

The modified discharge model is based on the system described in section 3.3.3. It includes non-stationary balance equations for the densities of charged and neutral species written on the assumption that the variation of the densities along the discharge axis is much slower than their variation in the radial direction. Evaluation of the axial gas velocity, governed by natural convection, allows one to relate the variation of the plasma parameters with time and with position along the discharge axis. The kinetic scheme used for evaluation of the kinetic terms in the balance equations is the same

as that used in [43]. The modelling was, again, conducted by Prof. George Naidis in collaboration with the author.

4.4 Results and discussion

Unless stated, the unmodulated, steady-state rms conduction current for all measurements was 18 mA. All parameters are normalised to their mean values with details of the absolute values given in the main text.

4.4.1 Electrical characteristics

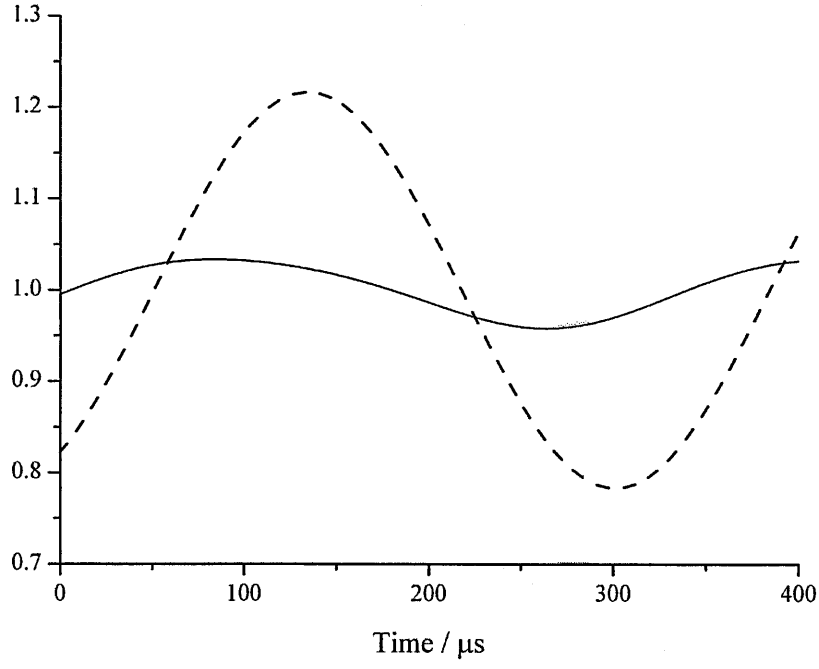

Figure 4.3: The modulating voltage (solid) and conduction current (dashed) at 3 kHz. The modulation depth on the current is 22 %. Note; the actual current and voltage oscillates at 325 kHz.

The modulating voltage and current characteristics were introduced in section 2.3.7. It was shown that relationship between the two followed the perturbations of the V-I curve. There is a delay between the modulation envelopes of current and voltage. To illustrate this, the global electric characteristics for a 3 kHz modulation frequency are given in figure 4.3 which shows the voltage leading the current by 50 μs, equivalent to a

phase delay of 60° at 3 kHz. Additional measurements made at several audio frequen-

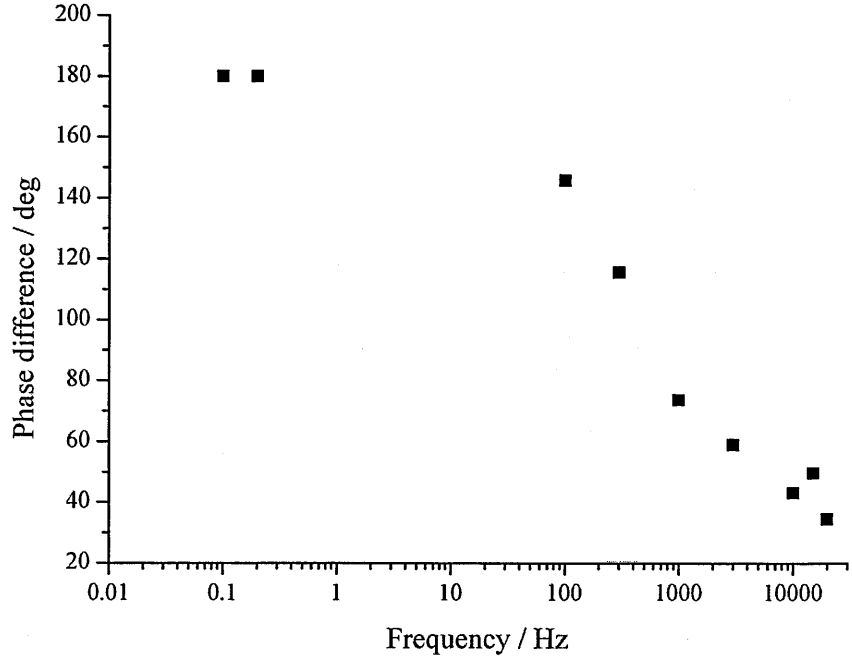

Figure 4.4: The phase difference between the modulating current and voltage.

cies shows this phase delay to be a frequency dependent effect (figure 4.4). Looking again at the V-I curve in figure 2.9 it can be seen that an increase in current would result in a decrease in voltage. This results in a 180° phase difference and this can be seen at the lowest modulation frequency. Delay effects from the external circuitry were accounted for by measuring the modulating signals with no plasma present. For this situation, a consistent 180° delay was observed over the frequency range, implying that the differing delays seen in figure 4.4 must be caused by the plasma itself. Such delays have been reported for other plasma sources and can be attributed to an inductive reactance in the plasma. Modelling the plasma as a circuit with discrete parallel resistive and inductive components allows for a change in impedance with increasing frequency [5]. The delay has no direct effect on the acoustic emission which is closely linked to the current flowing in the plasma.

At higher modulation, distortion is observed in the voltage waveform. Figure 4.5 (top) shows the measured modulating voltage and the conduction current for a frequency of 3 kHz and a modulation depth of 33 %. The equivalent modelled results

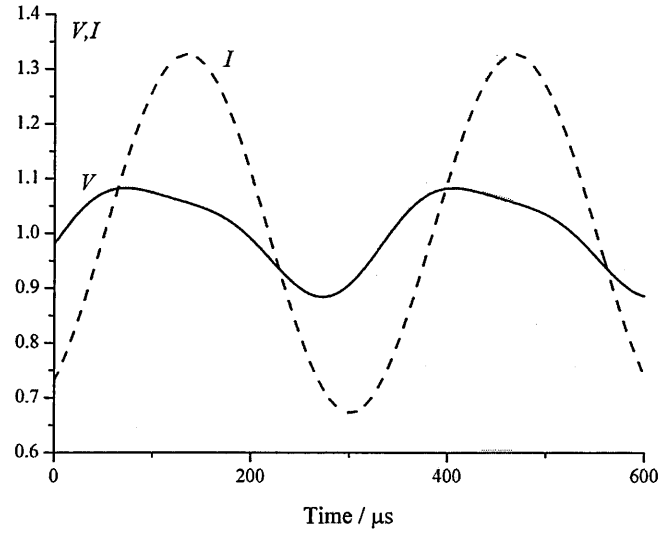

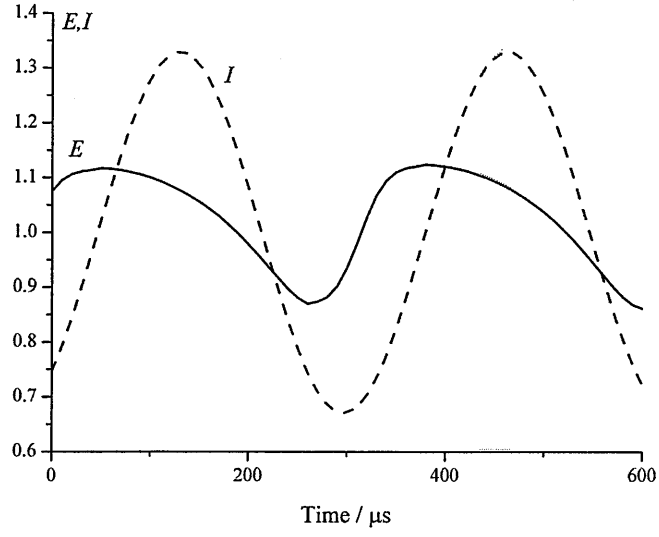

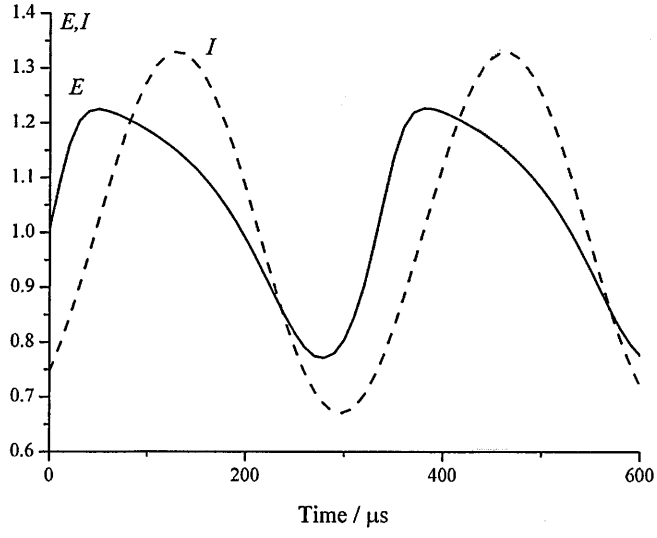

Figure 4.5: The measured electrical characterstics (top) and equivalent model results calculated for $z = 0.5$ mm (middle) and $z = 6$ mm (bottom) for a 33% modulation depth.

present the rms electric field, E, which is used to compare against the voltage variation. A direct comparison between the measured voltage amplitude and modelled electric field amplitude is only qualitative as the global value for the measured results is presented whereas an axially dependent result is obtained from the model. The measured electric field value in an unmodulated plasma (figure 3.7) as a function of conduction current was deduced by neglecting the electrode region and is 89 kV/m for an rms conduction current of 18 mA. The modelled electric field values are 105 and 89 kV/m for $z = 0.5$ and 6 mm respectively.

The model calculates a variation in E in the bulk that is a factor of two greater than that measured. The distortion from the measured results is also seen in the waveform for E. This is a reflection of the large modulation amplitudes along the V-I curve where the behaviour starts to become non-linear in nature. The delay between E and the conduction current in the modelled results, is 65 μs, which is maintained at both axial positions. This is similar to that determined between the modulating voltage and the conduction current in the measured results.

4.4.2 Discharge radius and optical intensity

The relative variations of the intensity and the discharge radius taken from both the UV and the visible emission are given in figure 4.6. For these measurements, it is not possible to make a direct comparison between the two as different modulation depths were used on the conduction current for each spectral region; initially, a 15% modulation depth was used when obtaining results for the visible emission but this level of modulation was found to be insufficient when trying to detect the effects of modulation in the UV region through spectroscopy. Measurements are presented for an axial position of $z = 6$ mm for both emission regions and compared with their respective modulating conduction current, I.

While the intensity variation derived from the visible emission, Int_{VIS}, appears to be broadly in phase with the current, the intensity from the UV emission, Int_{N2C}, appears to fractionally lead the current by around 10 μs (hence, Int_{vis} also). This is likely to be associated with the different excitation and relaxation times associated

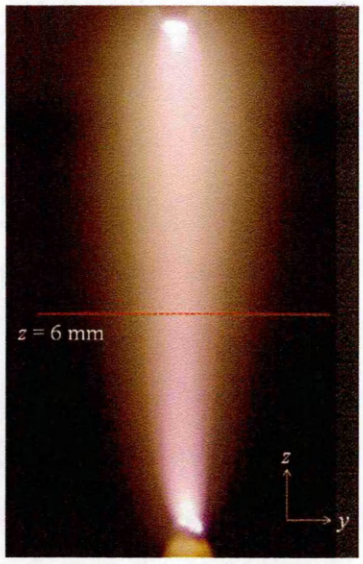

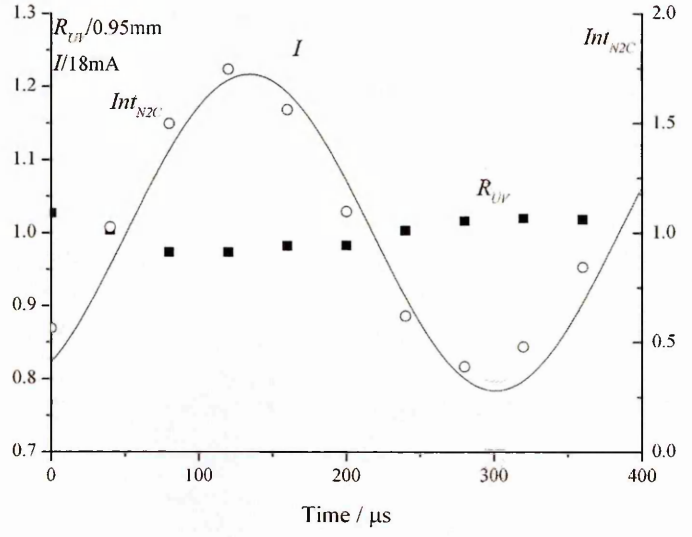

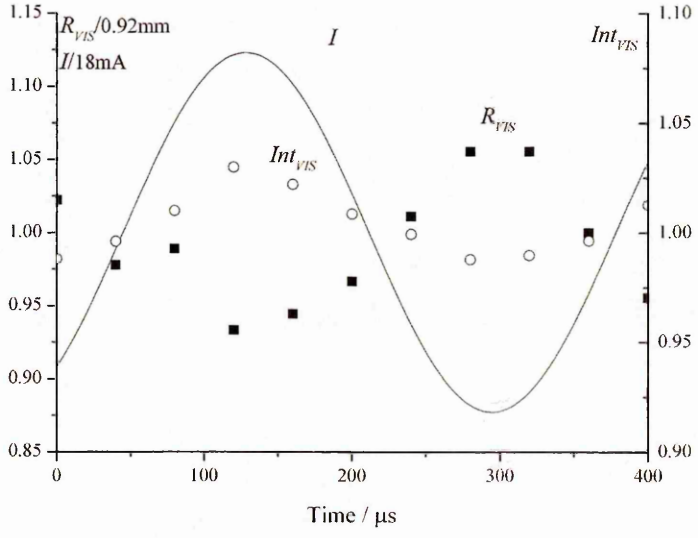

Figure 4.6: Normalised variation of the discharge radius (square), modulating current (solid) and optical intensity (circle) determined from the UV emission (top) and visible emission (bottom); $z = 6$ mm; rms conduction current = 18 mA.

with the different optical emission systems as previously discussed in the evaluation of the steady state discharge radius (section 3.4.3).

For both the UV and visible emission, the derived variation in discharge radius is $\pm 180^{o}$ out of phase with the derived variation in intensities. The radius determined from the visible emission, R_{VIS} varies by $\pm$ 5.6 % in 0.92 mm with a corresponding variation in R_{UV} of $\pm$ 2.6 % in 0.95 mm.

The greater variation in the visible radius may be understood as follows. Figure 4.7 gives the radial intensity profiles measured at the maximum, minimum and average on-axis intensity on the modulating period for both the UV (top) and visible emission regions regions (bottom). The UV radial profile is modulated across the entire radius. In contrast, the variation in the visible profile is confined to within r < 1 mm, coinciding with the central ionised region. Beyond this, a near-static radial profile is sustained. The visible intensity variation results from the visible transitions of N_2SP (350-400 nm), from secondary processes that are instigated by N_2SP excitation and from direct excitation of other visible emission systems (as suggested in section 3.4.2) and from ion-ion recombination. Out of the central ionised channel, the nature of the profiles imply that long-lived species coupled with radial convection results in a steady-state profile being formed that has no instantaneous response to the modulating current.

Similarly, the difference in the level of intensity variation between the two emission regions is a related effect; for the UV intensity in figure 4.6, its modulation is 75 %, reflecting the expected increase in the population of the excited nitrogen state associated with N_2SP emission. While this is significantly greater than the 22 % modulation depth on the current, it occurs because the resulting change in the electron energy distribution function (EEDF) has a highly non-linear effect on the rate constants so the increasing conduction current heats the EEDF providing a proportionately greater percentage of higher energy electrons required for initial excitation. The comparatively modest 3 % change in the visible intensity occurs in the central ionised channel and is shrouded within the constant emission of the wider radial profile.

The relative variations between measurement and the model also compare well as can be seen in figure 4.8 which shows the comparable quantities for the modelled UV

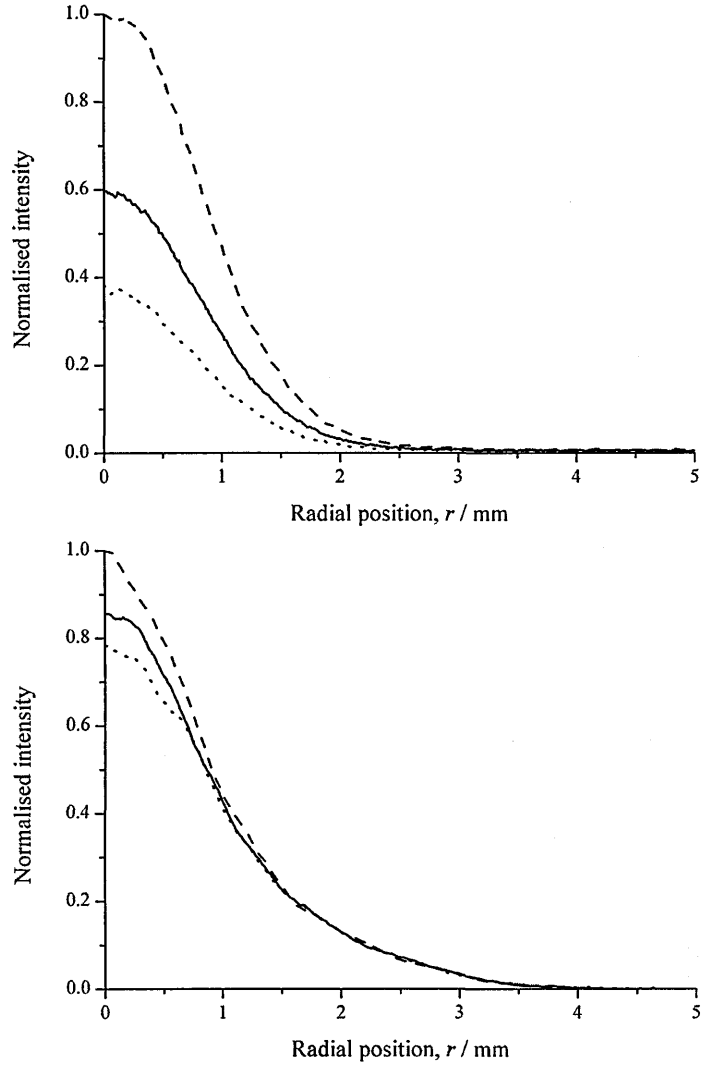

Figure 4.7: The variation in discharge radius measured in the UV (top) and visible (bottom) emission. The three profiles are measured at $t = 40$ μs (solid), 120 μs (dash) and 240 μs (dot) on the modulation cycle.

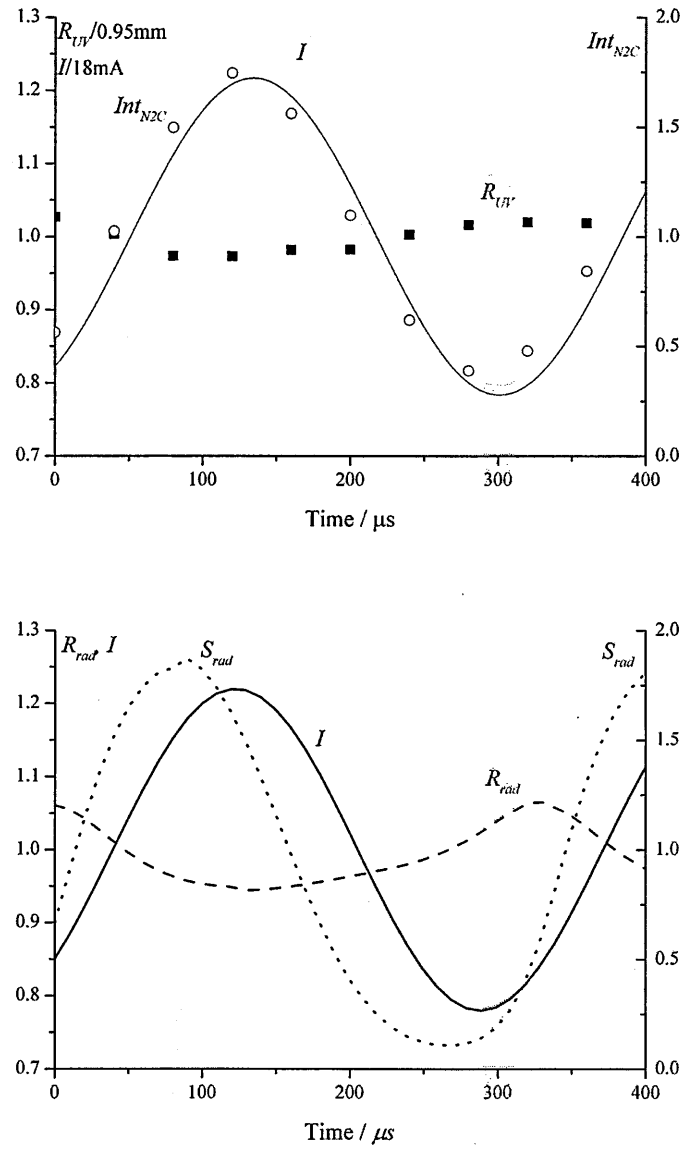

Figure 4.8: Upper graph shows the measured data of the UV emission repeated from figure 4.7. Normalised variation of the disharge radius (dash), modulating current (solid) and optical intensity (dots) for 3 kHz modulation calculated from the model; z = 6 mm, modulation depth = 22 % (lower).

emission with a 22 % modulation depth on the current. The optical emission, S_{rad}, was calculated from the expected excitation by electron impact to the excitated states in N_2SP and utilises the model electron density, n_e and rate constant for excitation to the radiative states. This shows a similar level of variation in the intensity and the radial variation to that measured though there is a slightly greater phase difference between S_{rad} and the current; the delays seen in the modelled and measured parameters are 50 μs and 8 μs respectively.

Another feature of the measurements is the non-linearity in the radius variation over the modulation period as the modulation depth is increased (figure 4.9). Here, the measured radius develops from a near-sinusoidal variation at 22 % modulation depth to a more harmonically-rich cycle at a modulation depth of 33 % on the conduction current. The increased assymetry of the cycle is one which the modelled result closely follows. As with the electrical characteristics under a large modulation, the plasma volume starts to display non-linear changes when the level of displacement starts to be significant relative to the plasma dimensions.

4.4.3 Plasma temperatures

The plasma temperatures, determined by fitting modelled spectra to the measured emission spectra, are given in figure 4.10 at an axial positions of $z = 0.5$ mm and $z = 6$ mm. Evidence of modulation in both the rotational (T_r) and vibrational (T_v) temperatures is seen. The modulation is greatest at the electrodes and reduces by around a factor of two in the main body. This makes the variations in T_r and T_v less clear to follow but it can still be seen that a phase relationship between P, T_r and T_v is maintained between the two axial positions.

At the lower electrode, the variation in T_r around its steady-state value is 2756 K $\pm$ 69 K ($\pm$ 2.5 %) with a corresponding variation in T_v of 3141 K $\pm$ 76 K ($\pm$ 2.4 %). As both T_r and T_v show very similar level of amplitude variation, this indicates that they are well coupled; the uncertainty applied for all temperature measurements is approximately 10% as for the steady-state measurements in the previous chapter. For this to occur, the energy transfer results from V-T relaxation followed by translational-

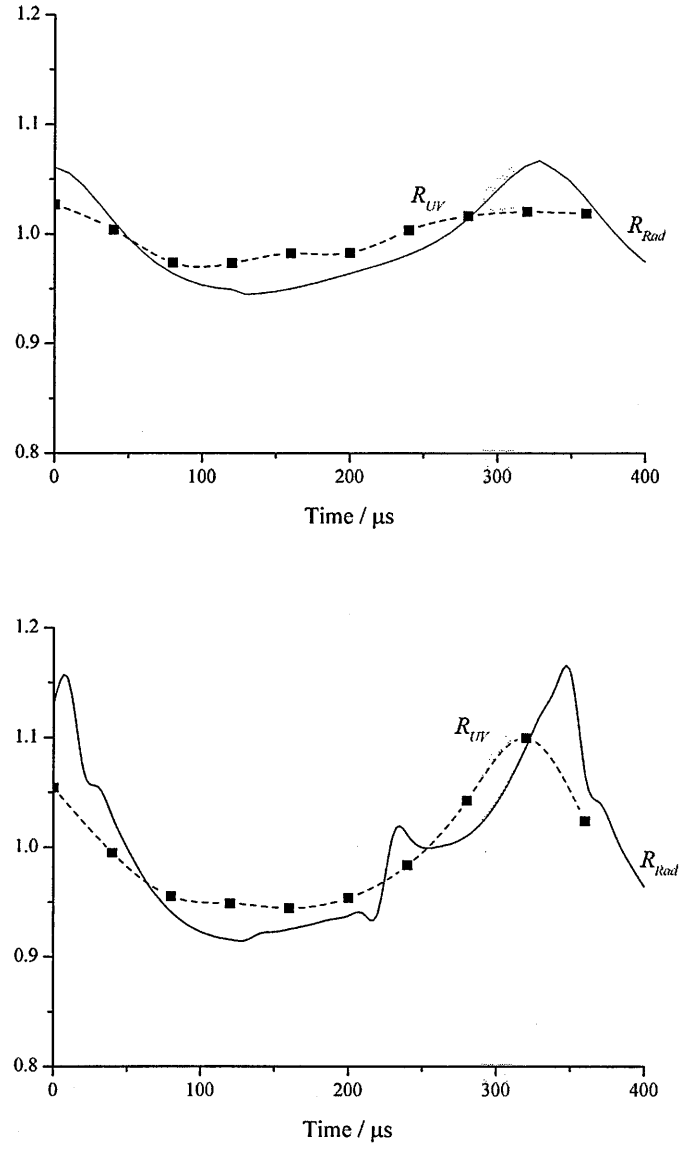

Figure 4.9: A comparison of the normalised radial variation measured from the UV and modelled emission for a modulation depth of 22 % (top) and 33 % (bottom).

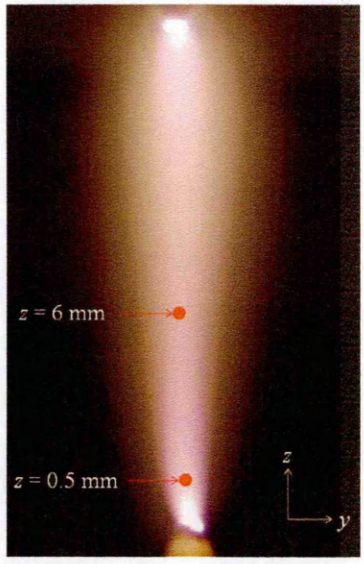

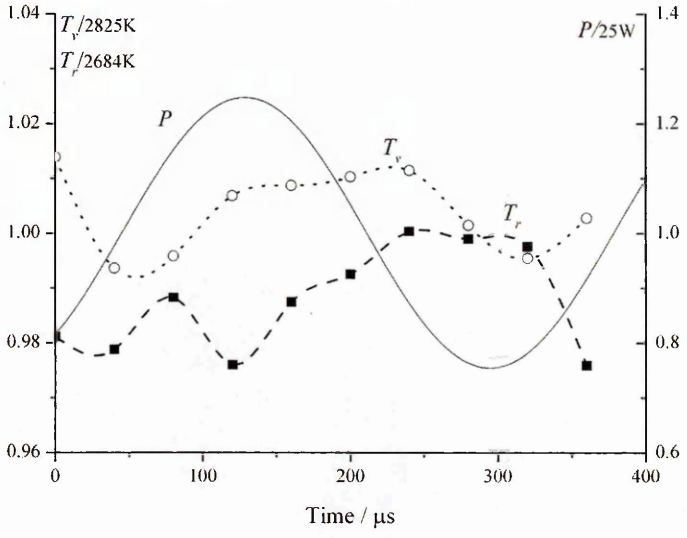

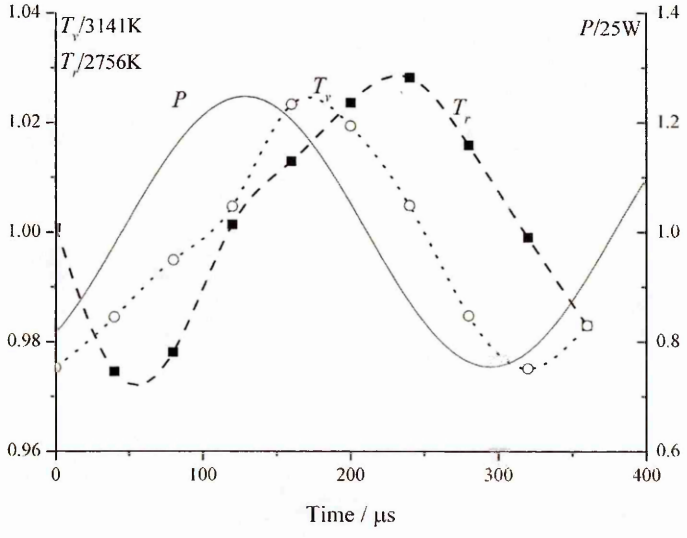

Figure 4.10: Measured temperatures and power for a modulation depth of 22 % at z = 6 mm (top) and z = 0.5 mm (bottom).

rotational (T-R) equilibriation or from vibrational-rotational (V-R) relaxation directly within nitrogen. The power, P, shows a significantly greater level of variation of $\pm$ 25% in 25 W; the difference between this and the amplitude in the two temperature variations indicates that significant energy is lost to other mechanisms in the plasma such as joule heating (translational energy of gas) after which energy is conducted and convected away.

At 3 kHz, P leads T_v by 34 μs, and T_v leads T_r by a further 70 μs. These time differences are an indication of the time constants for the gas heating mechanisms to occur. The energy path of interest in these measurements is electron-vibrational (e-V) excitation followed by V-T relaxation; for V-T relaxation in nitrogen, the typical timescale is 10-100 μs [58] which corresponds to that measured if T_r is taken as representative of the gas temperature. The timescales for e-V excitation can be determined from a simple approach using the electron collision frequency and the vibrational excitation cross-section due to electron collisions. The collision frequency, ν, between electron and the vibrational state in nitrogen is given by,

$$\nu = \bar{v} n_g \sigma \tag{4.2}$$

where $\bar{v}$ is the average electron velocity, n_g is the neutral particle density and σ is taken as the cross-section for vibrational excitation in the nitrogen molecule [47]. Reference values for the vibrational excitation cross-sections are taken for the transition, v = 0-1, which is assumed to be the most populated state during excitation [59]. The neutral gas density is determined from the ideal gas law at atmospheric pressure and with the gas temperature taken as the previously determined steady-state T_r of 2756 K. The average electron velocity is determined from,

$$\bar{v} = \sqrt{\frac{2\epsilon}{m_e}} \tag{4.3}$$

where m_e is the mass of an electron and ϵ is the electron energy. For a typical electron energy of 1 eV [31], σ is around 3x10^{-23} m^2. From this, ν is approximately 5 x 10^7 s^{-1} so the time constant for collisional relaxation is $\sim$ 0.02 μs. The dependence of

the collision frequency on the cross-sectional area and electron velocity means that the excitation time increases with a decrease in these two quantities; for $\epsilon = 0.7$ eV, $\sigma = 2\text{x}10^{-24}$ m^2 and the timescale for e-V excitation increases to $\sim 0.4\mu$s. The opposite occurs for electron energies greater than 1 eV with the excitation time becoming shorter. This analysis implies that the delay between the vibrational temperature, T_v, and the input power, P, (which is representative of the varying conduction current) occurs from vibrational excitation due to the significant number of lower energy electrons within the current. This should be reflected in the electron energy distribution function (EEDF) for the plasma and determination of this would be able to confirm the timescales between the power and T_v variation (though this is not available here).

Figure 4.11 presents the results for an increase in the temperatures and the power with modulation depth. Ideally, a third modulation depth would be required to ascertain the linearity of the temperature variations to the increased power input. But for the two conduction current modulation depths - 22% and 33% - measured at the electrode ($z = 0.5$ mm), the phase relationships remain unchanged. The amplitude of the variation in T_v and T_r increases to around 4-4.5% and the temperatures remain closely coupled.

Modulation in T_r and T_v is also evident off-axis up to a radial distance of $r = 1$ mm. Figure 4.12 gives T_r (top) and T_v (bottom) variation measured as an axial position of $z = 0.5$ mm and in radial increments of 0.5 mm from the on-axis position. Beyond $r = 1$ mm, the signal to noise ratio significantly degrades the quality of the emission spectrum resulting in a loss of measurement accuracy. The steady-state temperatures for each radial position is within $\pm$ 50 K of the on-axis reference temperature values and all measurements remain in phase with a near constant amplitude variation. This indicates that the plasma exhibits near uniform conditions up to $r = 1$ mm.

The comparable results of the modelled plasma temperatures and power variation at the axial positions of $z = 0.5$ and 6 mm and for a 22% modulation depth are presented in figure 4.13. The model includes one vibrational temperature, T_v, and a single gas temperature, T_g - it does not distinguish the rotational temperature on the grounds that this is closely coupled to the gas. The phase differences between the vibrational

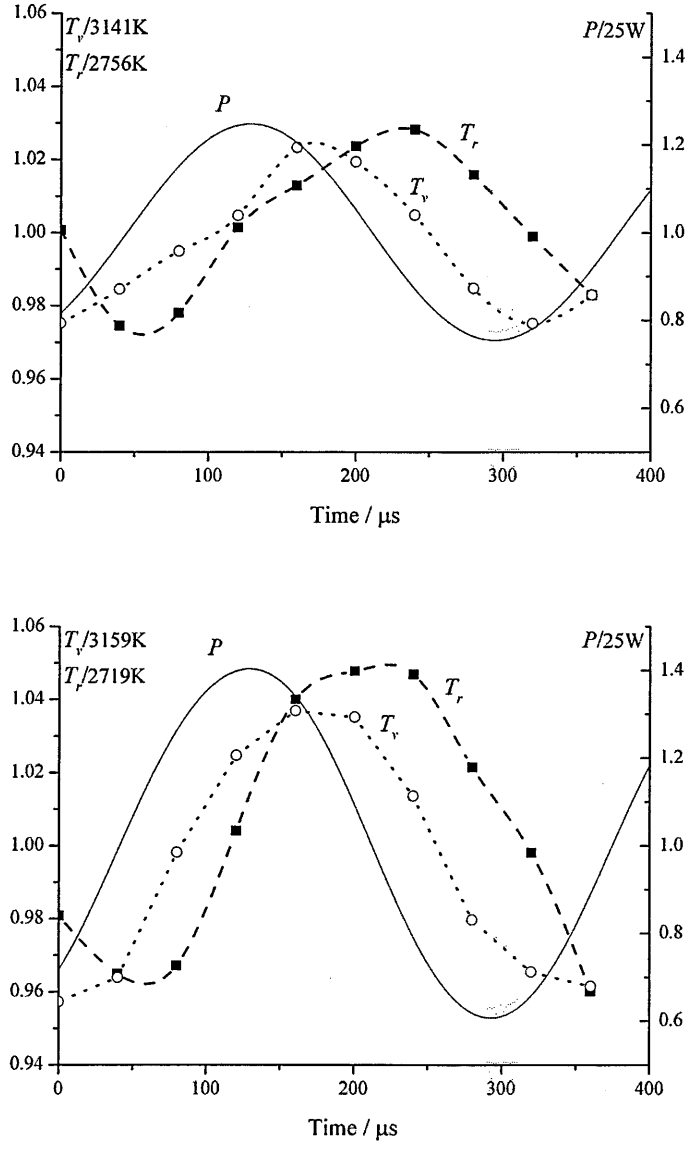

Figure 4.11: Measured temperatures and power for 22% (top) and 33% (bottom) modulation depths at $z = 0.5$ mm.

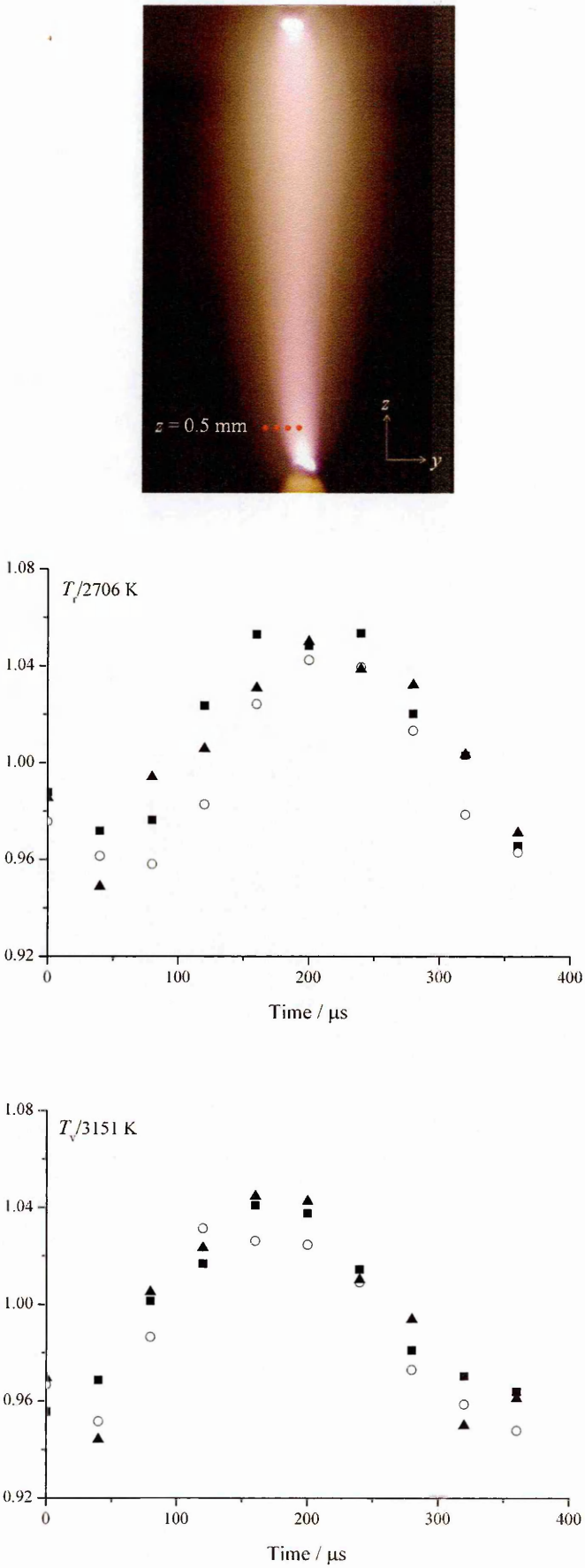

Figure 4.12: T_{r} (top) and T_{v} (bottom) variation at $r = 0$mm (Square), 0.5 mm (circle) and 1 mm (triangle); $z = 0.5$ mm.

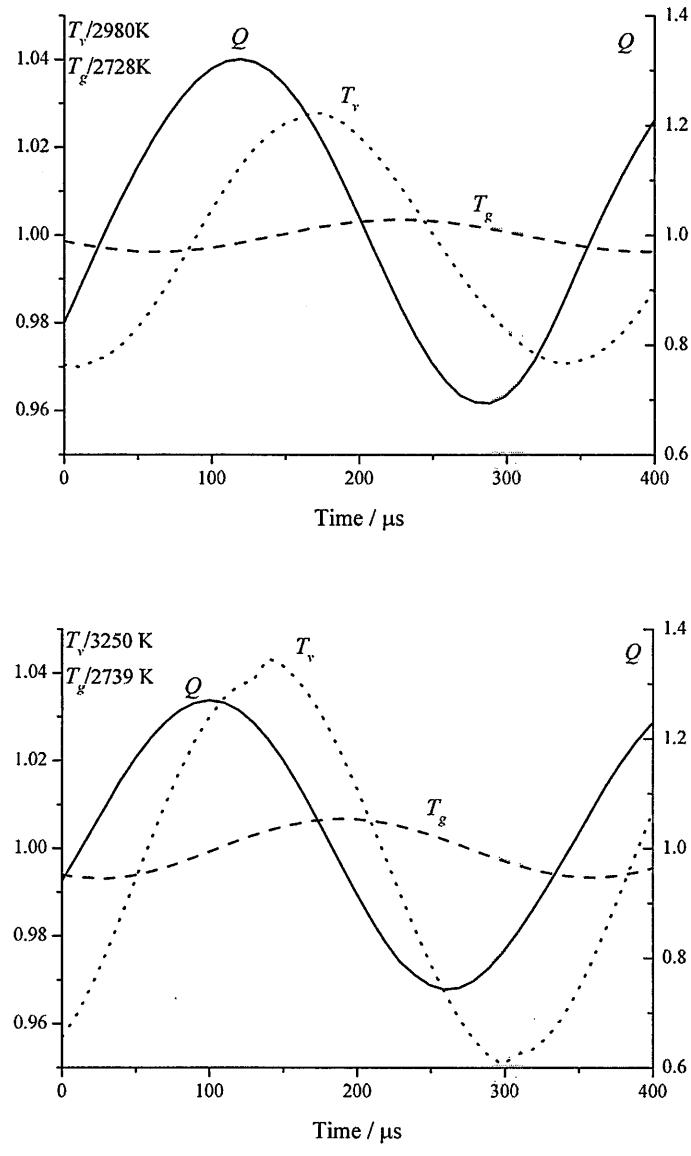

Figure 4.13: Modelled temperatures and power for a modulation depth of 22 % at $z =$ 6 mm (top) and $z = 0.5$ mm (bottom).

temperature T_v, gas temperature T_g and power, Q are consistent with the measured values with Q leading T_v by 40 μs, and T_v leading T_g by 60 μs. This gives confidence that the rate constants used to define the temporal variation between the parameters in the model are correct. While the variation amplitude in Q is comparable to the measured result, the variation in both temperature calculations differ from the measured result. For T_v, the difference is modest with the amplitude up to a factor of two greater than the measured T_v with a variation of 3250 K $\pm$ 137 K (4.2%) and 2980 K $\pm$ 83 K (2.8%) for axial positions of $z = 0.5$ and 6 mm respectively; the decrease in amplitude with increasing axial position is also calculated. However, the variation amplitude in T_g for both axial positions is at around a factor of four less than the equivalent measured variation in T_r. The calculated variation for T_g is 2739 K $\pm$ 16 K (0.6 %) and 2728 K $\pm$ 11 K (0.4 %) at axial positions $z = 0.5$ and 6 mm respectively. T_r and T_g are assumed to be in equilibrium and it is not certain why the modulation amplitudes differ signficantly between the two. The steady-state results for T_r and T_g are close and indicate that, while near-equilibrium conditions exist in the unmodulated plasma, this is not the case when plasma is modulated at 3 kHz; essentially, some of the energy in the excited vibrational state of nitrogen is not transferring to translational energy in nitrogen while under modulation. If this is the case, then the T-R equilibriation, suggested earlier as one path of energy transfer from the V-T relaxation, would not be possible. A direct comparison to the measured results presented in figure 4.11 is given for a 33% modulation depth on the conduction current. T_v shows just over 6% increase in the modulation amplitude whereas the measured result indicates a 3% modulation of vibrational temperature.

4.4.4 Correlation with the acoustic signal

The 3 kHz acoustic signal previously presented in figure 2.24 is re-introduced in figure 4.15 together with the variations in the rotational and vibrational temperatures and the UV derived discharge radius for comparison. The acoustic waveform has been corrected back to the source to account for the time of flight between the acoustic signal being emitted and received at the microphone. A comparison between the signal ampli-

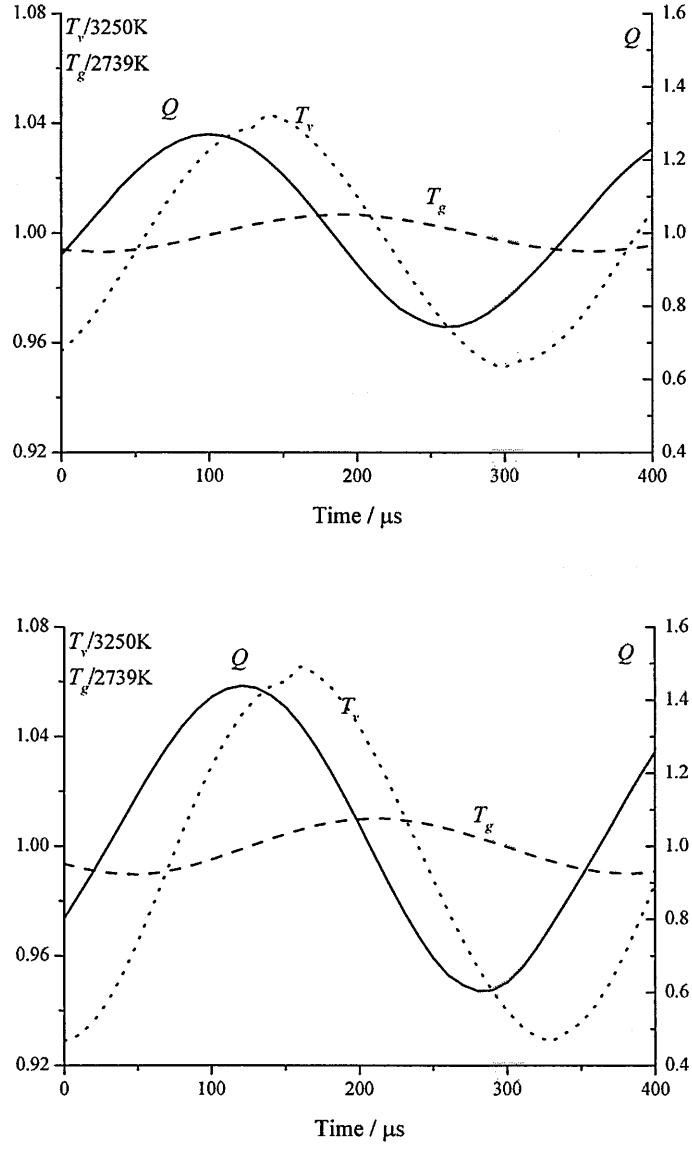

Figure 4.14: Modelled temperatures and power for 22 % (top) and 33 % (bottom) modulation depth at $z = 0.5$ mm.

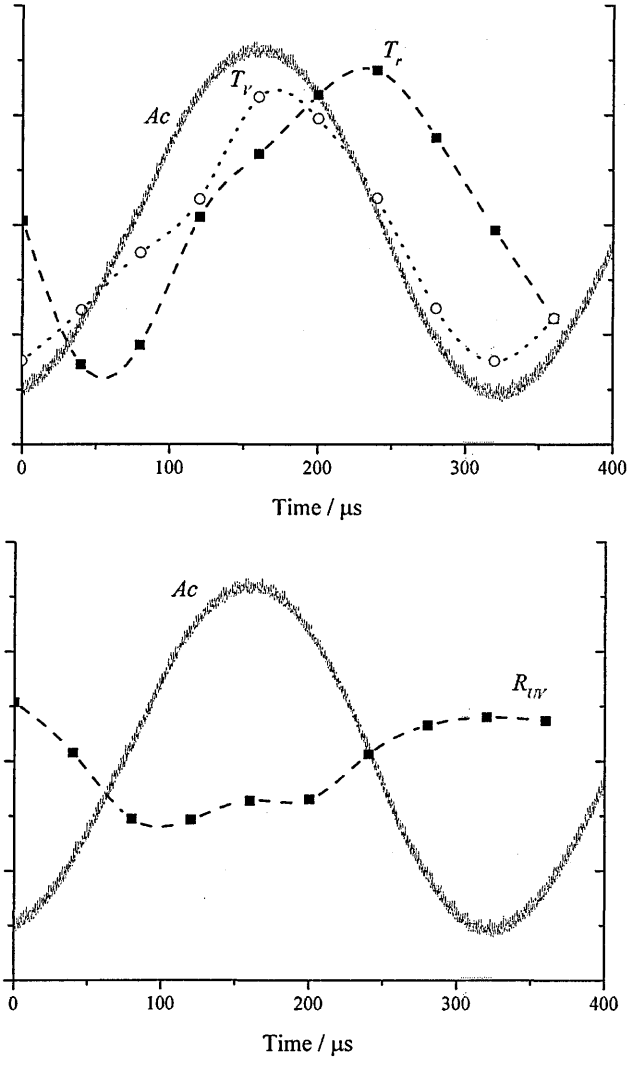

Figure 4.15: Correlation of the plasma temperatures (top) and the discharge radius (bottom) with the 3 kHz acoustic signal. The axis are not labelled as it is the phase relationship that is of interest.

tudes is not possible as the modulation depths are different but the phase relationships between the respective waveforms is valid and emphasis is given to this relationship. The results show that for this frequency, the acoustic pressure wave is closest in phase to the vibrational temperature. This is an unexpected result as it had been assumed that the acoustic signal would be more closely coupled to the gas temperature (or the rotational temperature as its equivalent parameter).

The variation in discharge radius is approximately 180^o out of phase with the variation in acoustic pressure. This behaviour is characteristic of a pulsating surface under specific conditions. For a spherical source, the relationship between a moving surface and the pressure wave generated at that surface is given through the relation,

$$U = \frac{P_{\text{ac}}}{z_s} \tag{4.4}$$

where P_{ac} is the acoustic pressure amplitude, z is the *specific* acoustic impedance of the medium into which the pressure wave propagates and U is the surface speed of the radially vibrating sphere [1]. The surface speed is the differential of the surface displacement (which is directly comparable to the measured radius R_{UV}). To determine the specific acoustic impedance, it is useful to re-introduce the radiation impedance for a sphere previously expressed in section 2.5.3,

$$Z_r = \rho_0 c S \cos\theta_a e^{j\theta_a} \tag{4.5}$$

where ρ_0 is the air density, c is the speed of sound in air, S is the surface area of the sphere and $\cot\theta_a = ka$ [1] with k = wavenumber and a = source radius; to clarify, Z_r is used in respect to the area where the mechanical driver is coupled to the medium whereas z applies to the medium as a whole. The specific acoustic impedance is determined as follows,

$$z_s = \frac{Z_r}{S} \tag{4.6}$$

where S is the surface area of the driver. Substituting the radiation impedance from equation 4.5 into equation 4.6 which in turn is used in equation 4.4 introduces a phase relationship between pressure and speed due to the θ term. If a large value for kr is

used, for example if the size of the source is comparable to the acoustic wavelength, $\theta \rightarrow 0$ and the pressure and surface speed are in phase with each other as for a plane wave. Conversely, small values of kr, typical of when the source size is small relative to the acoustic wavelength, lead to a phase shift between pressure and speed. This is the case for the dimensions and the wavenumber based on the plasma measurements; the pressure leads the surface speed by a phase difference of $\pi/2$ which translates to a phase difference of π between pressure and radial displacement. A similar relationship also occurs if the parameters are determined for a cylindrical source. However, while the relationship holds for the measurements here, it would be necessary to repeat the analysis at additional audio frequencies to have confidence that the relationship is a general one.

4.4.5 Temperature and pressure

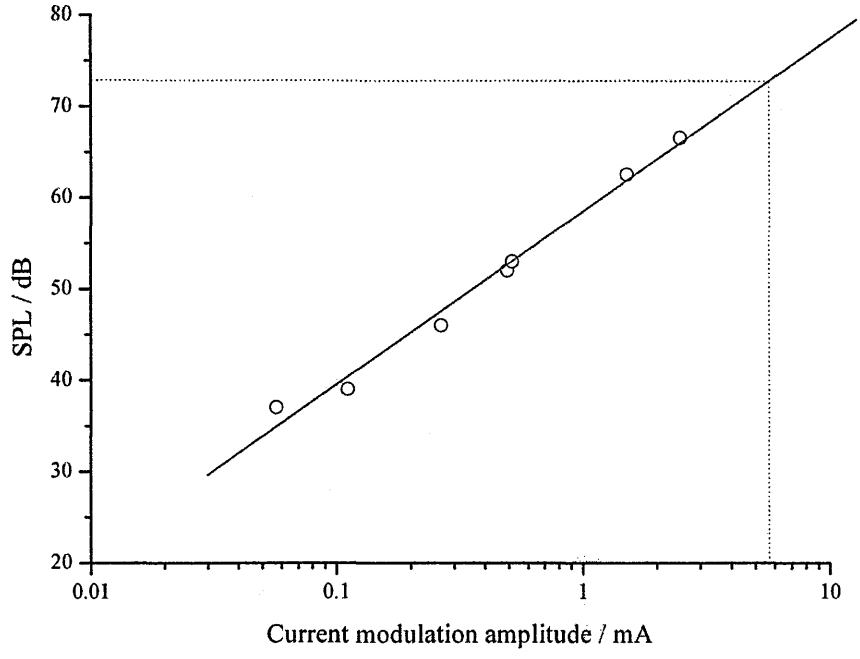

Figure 4.16: The predicted SPL for a modualtion amplitude of 5.6 mA.

It is interesting to compare the SPL in the vicinity of the discharge based on the acoustic measurements with that expected from the spectroscopic temperature measurements. The SPL emitted at the plasma needs to be calculated for a 22 % modulation level applied to the conduction current. Although the SPL was not measured for this modulation depth, the expected SPL can be deduced from the plot in figure 4.16

which shows the SPL as a function modulating current amplitude (as given previously in figure 2.15). A 22 % modulation of the steady-state conduction current translates to a modulating current amplitude of 5.6 mA. Through linear extrapolation the expected SPL for this modulation amplitude is approximately 73 dB at a distance of around 1 m from the electrodes. The SPL is adjusted back to where the acoustic emission orginates within the discharge. If the characteristic decrease of a pulsating sphere is used, the SPL (based on the measurement of the UV emission at the electrode) is approximately 142 dB at 0.3 mm.

With knowledge of the rotational temperature variation, the SPL can also be determined. Mazzolla [5] has descibed a DC glow discharge sustained in air with similar conduction current levels to the Tesla coil RF plasma. The Mazzolla analysis is based on an adiabatic assumption and small modulation depth so that,

$$\frac{\delta p}{p} = \frac{\gamma}{\gamma - 1}\frac{\delta T}{T} \tag{4.7}$$

where p is the ambient pressure, δp is the pressure change, T is the steady-state temperature and δT is the temperature change. The ambient pressure is one atmosphere (101 kPa). The rotational temperature change δT_{r} has been measured as $\pm$ 69 K. The steady-state temperature T_{r} is 2756 K within 0 mm $<$ r $<$ 0.5 mm. The expected change in pressure is then $\pm$ 8.9 kPa. Using equation 2.4, the SPL is approximately 170 dB.

The difference between the SPL derived from the acoustic signal and that from the temperature variation is significant. A related effect is with the differences seen in T_{v} and T_{g} as calculated from the model in section 4.4.3 and results from the plasma not maintaining full adiabatic conditions with this modulation frequency. The frequency response previously given in section 2.5.3 is presented again in figure 4.17 with the 3 kHz frequency highlighted. This lies at a point just into the frequency drop off region which is associated with the plasma operating under non-adiabatic conditions. It is likely that for 3 kHz modulation that thermal conduction becomes significant when compared to the timescales required for heat to be inputted into the discharge. If this assumption is correct, then the rotational temperature variation would not be represen-

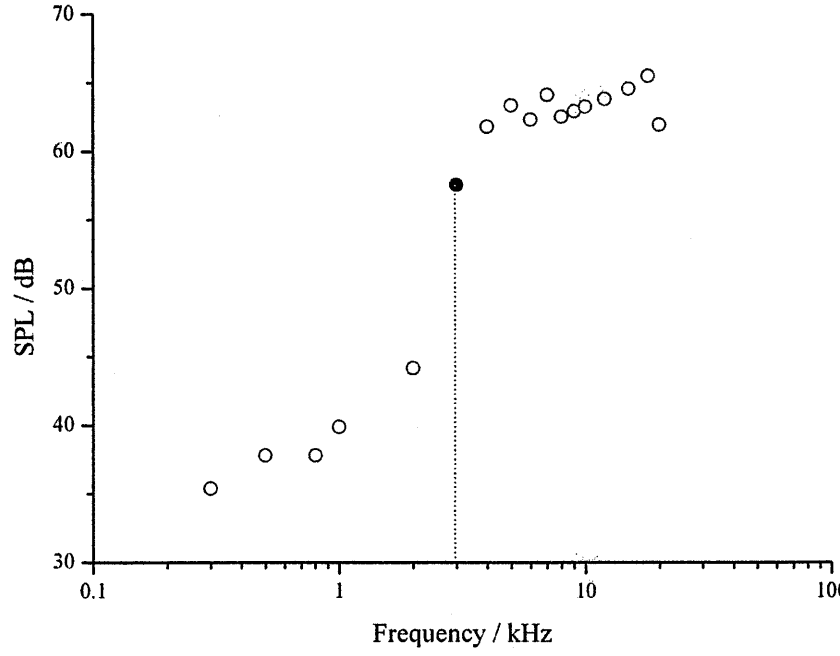

Figure 4.17: The frequency response curve with 3 kHz modulation frequency highlighted.

tative of the gas temperature variation where a discharge is non-adiabatic. To achieve an emission level of 142 dB, the expected rotational temperature change is in the region of ± 3 K on a steady-state temperature of 2756 K would be required. This compares with the modelled temperature change of ± 16 K in 2739 K is used in equation 4.7, the corresponding SPL is 157 dB which, though closer to the expected measured result, still lies significantly outside of the measurement uncertainty.

4.4.6 Electric-acoustic power efficiency

An estimate of the power efficiency can be made by calculating the acoustic power from the SPL and relating it to the electrical power variation determined in this chapter. The analysis, presented in Kinsler [1], gives the relationship between the acoustic pressure and *intensity*, Int_{ac}, for a plane wave propagation as follows,

$$Int_{\mathrm{ac}} = \frac{P_{\mathrm{rms}}^2}{c_{\mathrm{air}}\rho_{\mathrm{air}}} \tag{4.8}$$

where P_{rms} is the rms acoustic pressure, c_{air} and ρ_{air} are the speed of sound in air and the air density respectively. While the plasma source is assumed to be spherical, the

measurement of the acoustic pressure is done at a sufficient distance from the source for the sound waves to be approximately planar in nature. The relationship between sound intensity and the time-averaged power, Π, is calculated as follows,

$$\Pi = I n t_{ac} 4\pi r^2 \tag{4.9}$$

where r is the microphone/electrode separation. This equation uses the surface area of a spherical shell centred on the acoustic source through which the intensity flux propagates. Using the previously calculated value of 75 dB at a distance of 1 m, the amplitude of the acoustic power variation is approximately 400 μW. When compared to the electrical power amplitude of 6.25 W (calculated from $\pm$ 25 % variation around 25 W), the efficiency is around 0.006 %. The only reference to efficiency is given by Mazzolla for a DC glow discharge [5]. Here, an efficiency of 0.003 % is calculated. More generally, the best efficiency that is obtained from a high quality mechanical loudspeaker can be up to 5 % [34] so the efficency calculated for the Tesla coil discharge is very poor in comparison.

4.5 Summary

Measurement of the plasma under modulation provides a good basis for understanding the dynamics of the plasma. The variation in the discharge radius shows that the central ionised channel is the most responsive to the varying input current as seen in the radial profile of the optical emission. The UV discharge radius responds mostly within $r < 1.5$ mm with the wider profile of the visible emission exhibiting steady-state behaviour which is sustained from the radial convection of long lived species originating on axis. This implies that the central channel is responsive to the modulating current and is likely to be the dominant source of acoustic emission.

Modulation is evident on all the variables measured. The relative phase difference between the input power and the temperatures most likely results from the timescales associated with the various kinetic processes in the discharge; this requires further investigation. The adapted Naidis model compares well with the measured characterstics

with many features of the measured waveforms being replicated. The strongest correlation comes from the relative phases between the plasma characteristics which suggests that the influence of modulation on the rate constants used for the calculations is appropriate. Where there is signficant difference in the amplitude of the variation, such as between the rotational and modelled gas temperature, the assumption was made that the non-adiabacity of the discharge is the cause. The difference between the SPL determined directly from acoustic measurement and through the relationship between the varying temperature and pressure suggests that the non-adiabatic nature of the discharge is again responsible. Measurement of the discharge at two or three other modulation frequencies where the discharge exhibits near-adiabatic conditions under modulation would give a fuller understanding of this effect. The techniques for this have been developed in the course of this thesis though there will be additional challenges on time resolution for work at higher frequencies and a full spectral response would also benefit from automated data analysis. The relationship between the acoustic and radial variations follows that expected for a pulsating sphere which was calculated from a simple model using the measured plasma parameters. Ideally, this requires additional measurements at other modulation frequencies to see if the effect is universal.

Chapter 5

Schlieren imaging

5.1 Introduction

The main characteristics of the Tesla coil plasma while under modulation were presented in the previous chapter. This provided a greater understanding of the behaviour of the modulated plasma. However, although spectroscopy enables accurate rotational temperature measurements, the method is limited spatially to the central current-carrying channel of the plasma where there are higher energy electrons required for the excitation and emission processes in nitrogen. Determining the translational (gas) temperature beyond this channel would provide a fuller understanding of the behaviour of the modulated plasma, and its contribution to sound production, but it requires a new approach. The high voltage and temperatures of the plasma source makes invasive methods unattractive and they would anyway perturb the plasma. One method for detecting and measuring gas temperatures 'remotely' is through Schlieren imaging. This chapter describes the Schlieren method and its use as a diagnostic tool, with emphasis on its use with a plasma. The development and validation of a lens-based Schlieren system is described and gas temperature measurements from the plasma, operated both in its steady-state and under modulation, are presented.

5.2 The Schlieren method

In this section, the key developments of schlieren imaging and the theory behind the effect are explained. The deflection of light due to thermally generated refractive index gradients in a homogeneous transparent medium provides an opportunity to measure the temperature profile directly. A lit barbecue provides such a medium. When looking at the coals burning, one supposes that they are hot but by looking at a patch of ground that is illuminated by sunlight which has passed through the air above the coals, an observer is able to 'see' the heat from the coals rising and forming pale turbulent shadows above the barbeque - such distortions are called *shadowgraphs*. The light and dark fronts result from phase changes from the thermally generated refractive index gradients being converted to intensity variations as they are projected onto the ground. The shadowgraph is perhaps the simplest form of imaging resulting from the interaction of light and a refracting medium. Schlieren imaging advances this approach to provide a controlled method for viewing the refracted wavefronts and converting them back to intensity variations when projected from the source that caused them. The deflection angle, ε_y, through which a ray of light is refracted in any small volume is proportional to the local refractive index gradient, n, as follows,

$$\varepsilon_y \propto \frac{\partial n}{\partial y} \tag{5.1}$$

5.2.1 A brief history of Schlieren imaging

A definitive history of Schlieren imaging is given by Settles [60] but a brief summary is given here. The earliest research into the effect was made by Robert Hooke as part of his studies of microscopy and telescopy. His interest in combustion led him to investigate disturbances created by thermal plumes and he developed a single lens system for imaging them (figure 5.1). In this configuration, light from the candle is incident onto the lens and focussed to a point at which position the eye of the observer can act as a detector (figure 5.1 - A). The medium along the optical path is homogeneous with a uniform refractive index and the observer sees a uniform illumination level. When a second candle is placed in the optical path (figure 5.1 - B), the air is heated by

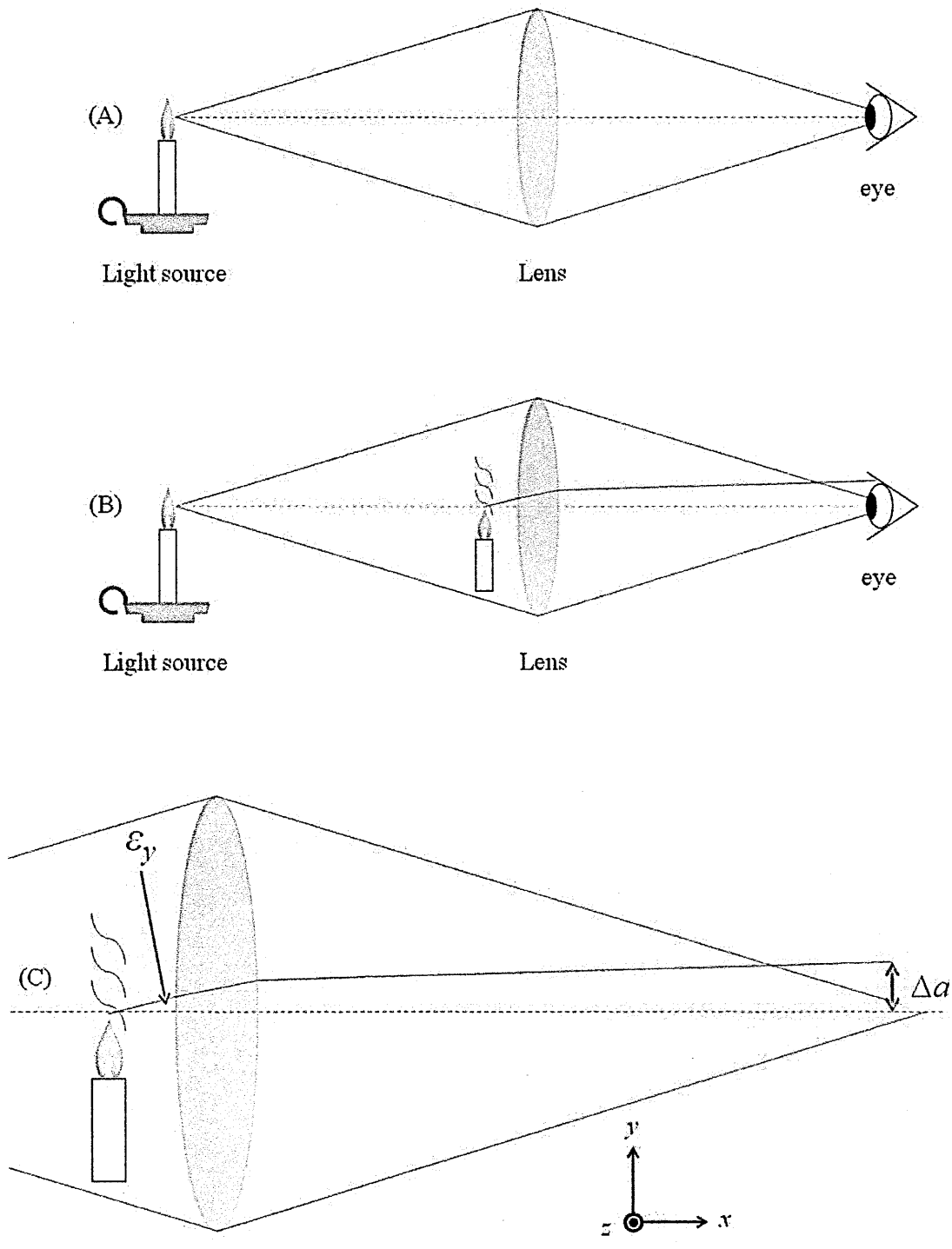

Figure 5.1: Hooke's Schlieren set-up and the geometric relationship.

it causing refractive index gradients resulting in the deflection or 'refraction' of the incident light. To the observer, a *contrast change* is seen where light and dark regions (relative to the reference illumination) result from the deflected beam being displaced away from, or onto, the pupil. The geometrical representation (figure 5.1 - C) shows a beam deflected by an angle, ε_y, causing a proportional displacement, Δa, at the focus and is expressed as follows:

$$\Delta a = f_{\text{foc}}\varepsilon_{\text{y}} \tag{5.2}$$

This highlights one of the key characteristics of a Schlieren system; the contrast changes are dependent on the focal length of the lens that is used for forming the source image. A long focal length lens would be able to detect smaller deflection angles (smaller refractive index changes) in the path. Details of the optical configuration of Hooke's experiment are sketchy but a replica set-up using a lens with $f_{\text{foc}} = 1$ m is sufficient to observe the deflections from the second candle [60]. While this situation had been investigated prior to Hooke's involvement [60], his contribution was to explain the relationship between contrast changes and the source that caused them. His work was left incomplete as the need for its use as a diagnostic tool had yet to arise. But this need was found by Leon Foucault (1819-1868) and, independently, by August Toepler (1836-1912) around a century after Hooke's research. The development of the telescope required higher precision optics for accurate imaging and Foucault developed the *knife edge test* to provide an accurate means of measuring the surface uniformity of telescope mirrors (figure 5.2). The principle of measuring beam deflections is maintained, though the focussing lens from Hooke's configuration is replaced with the telescope mirror under test. A light source combined with a pinhole is positioned slightly off-axis to produce a diverging beam that is incident on the mirror. For a perfect mirror, the reflected beam will focus to a point. If the mirror has surface irregularities, the reflected beam will spread away from the focus. The reflected beam is detected by the eye and Hooke's configuration is extended by adding a knife edge at the mirror focus to *cut off* part of the pinhole image.

The addition of the knife edge is the second important component for the Schlieren effect. Figure 5.3 shows the knife edge positioned at three different points into the

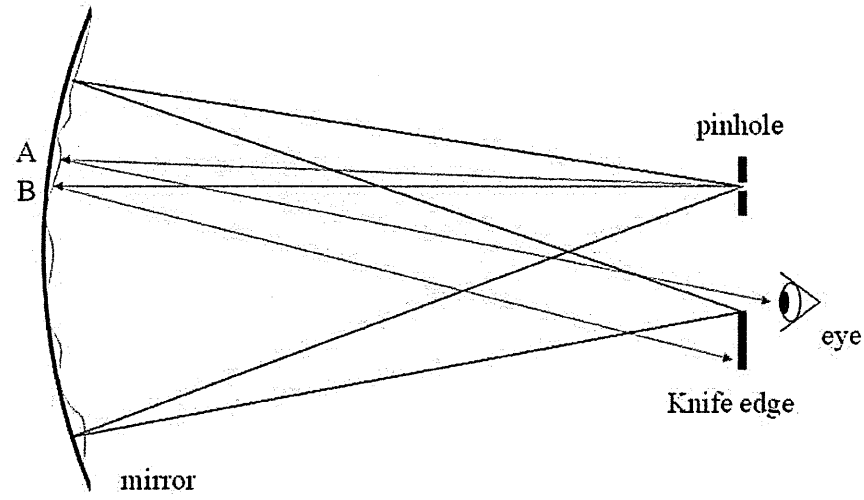

Figure 5.2: The Foucault knife edge test for mirror uniformity.

source image. The uncovered width, a, provides the reference illumination level. When the incident displaced image is moved by a distance, Δa the resulting effect is an increase (or decrease) illumination relative to the reference illumination level. Reducing the uncovered width by applying the knife edge into the source image determines the *contrast sensitivity*, or the rate of change of the image contrast. With no knife edge applied, the reference illumination level of the source image is dominant over the change in illumination from the displaced image and is an identical situation to what Hooke observed in his single lens configuration (figure 5.3 - A). As the knife edge starts to 'cut off' the source image, the uncovered width is reduced and the reference illumination level decreases (figure 5.3 - B). The change in illumination from the displacement becomes significant and results in the contrast change being more 'visible'. With a large region of the image source cut off, the change in illumination is significant relative to the reference illumination and more distinct contrast changes are observed. The uncovered width, a, of the focus defines also the *measuring range* of the system. For a strong deflection, the displaced source image moves entirely onto, or off, the knife edge and the measuring range of the system is exceeded. Under these conditions, no contrast change can occur; this effect is known as *over or under-ranging.*

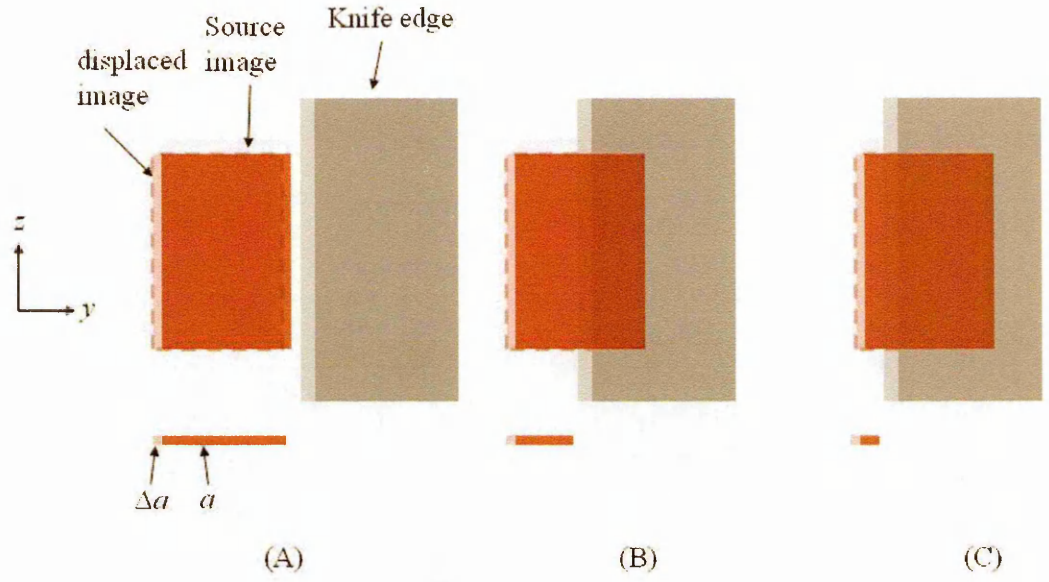

Figure 5.3: The knife edge applied to the source image defines the contrast sensitivity.

5.2.2 Schlieren and plasmas

While temperature changes are the dominant cause of refractive index gradients in a plasma, changes in composition can also be significant. Ionisation, dissociation and recombination within the plasma creates many charged species which, if produced in sufficient densities, will contribute to the overall refractivity. According to current literature, it is common for such conditions to occur mainly in high temperature, high current plasma arcs and, with the appropriate analysis, the density profiles of the individual species can be determined [61, 62, 63, 64]. In such cases, the refractive index is a summation of the individual components, $(n-1) = \sum_i f_i(n_i - 1)$, where n_i and f_i are the refractive index and volume fraction of species, i [65]. The analysis of Prevosto [62] is more specific and gives equations for the individual species as follows,

$$(n-1)_e = -\frac{1}{4\pi\varepsilon_0}\frac{e^2\lambda^2}{2\pi m_e c^2}n_e \tag{5.3}$$

$$(n-1)_{+,N} = \frac{1}{4\pi\varepsilon_0}2\alpha_{+,N}(\lambda)n_{+,N} \tag{5.4}$$

where n_e = electron number density, $n_{+,N}$ = ion/neutral number density, λ = wavelength of light and $\alpha_{+,N}$ is the *polarizability* of the ion/neutral species. The temperature

measurements and electrical properties presented in Chapter 3 indicate that, while the RF cycle of the plasma prevents full arc conditions from occuring, a significant level of ionisation is present based on the calculated electron density. The contribution of the charged species was assessed using equations 5.3 and 5.4 (along with the previously determined values for the discharge radii and a global electron density of 10^{18} m^{-3}) to enable density profiles for the electron, ion and neutral species to be modelled in order to determine their effect on the intensity profile. Reference values were used for the polarizabilities of air, nitrogen and oxygen ions with the discharge radius taken as the profile width. The wavelength of light was taken as 670 nm and the intensity variation calculated through an Abel transform of the summed density profile; this method is described later in section 5.4.2. The reference values used indicate a negligible contribution to the intensity profile from electron and composition profiles and suggest that significant effects start to occur when the densities of the charged species are greater than 10^{23} m^{-3}. Therefore, the calculations for the refractive index (and gas temperature) were based solely on the number densities of neutral components.

5.3 Experimental set up and systematic evaluations

In this section the design and implementation of a Schlieren system is described. Systematic studies of the optical system and the analysis method were carried out with a calibration completed using a known standard to give confidence in the system's response. The studies are described individually and an overall uncertainty is presented.

5.3.1 Experimental set-up

A dual-field lens Schlieren system was constructed (figure 5.4). A 40 W tungsten-halogen bulb (A) combined with a diffuser and 5 mm diameter aperture produced an extended light source with uniform intensity along the optical path; initial measurements with laser sources showed that uniform illumination was difficult to achieve without more complicated optics being implemented. The bulb was enclosed in a metal cylinder to contain stray light. The source was imaged onto an adjustable rectangular slit using the condenser lens, L_{con} (f = 75 mm). During measurement the slit width

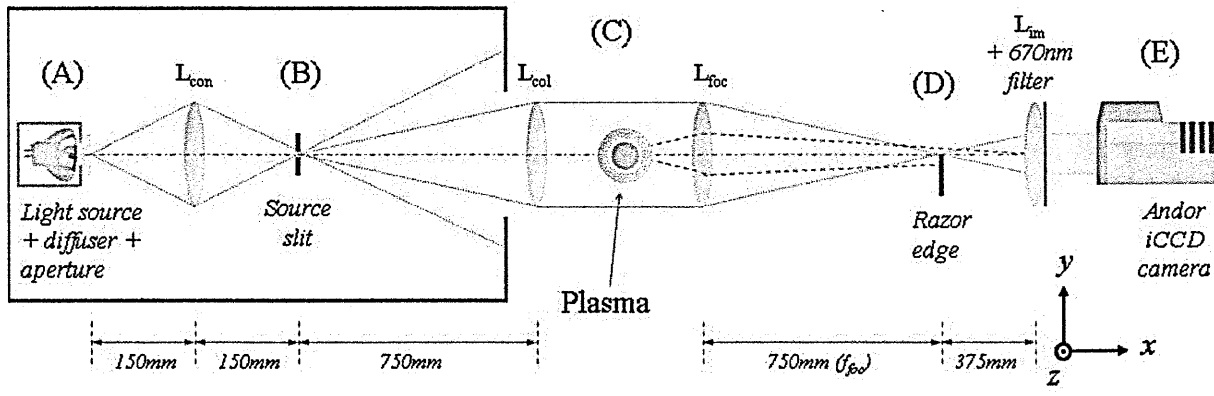

Figure 5.4: A schematic diagram of the dual-field lens Schlieren configuration.

was set to a fixed value between 1.8 - 2 mm and was measured with vernier calipers as the system was set-up. The diverging beam from the slit was captured by a plano-convex lens, L_{col} (f = 750 mm) which collimated the beam through the test area to a focussing lens, L_{foc} (f_{foc} = 750 mm). The source image was focussed and a razor blade was used as the cutoff in the focal plane. The razor blade was mounted on a dual-axis translation stage with movement into the source image (y- dir) and along the optical axis (x- dir). The razor blade was oriented vertically as in figure 5.3 and, therefore, only the refractive index gradients in the radial direction with respect to the plasma plume were measured. A bi-convex lens, L_{im} (f=375 mm), is positioned so that the source image is at its focus and collimated the beam onto the gated Andor i-CCD camera positioned at the image plane. A 670 nm filter, positioned after the imaging lens, filters the white light to produce a near-monochromatic image field and improves the spatial resolution through the elimination of dispersion. The filter also removes the ambient light in the laboratory as well as removing the emission from the plasma. This set-up produced a 2:1 scaled down image of the object under test with a spatial resolution on the CCD of approximately 27 μm/pixel.

5.3.2 Setting up and alignment

The lenses were mounted in holders and fixed to an optical track with alignment carried out using a Class 2 HeNe laser. The background illumination was reduced by covering the camera and the light source with a cardboard surround. External sources of plasma

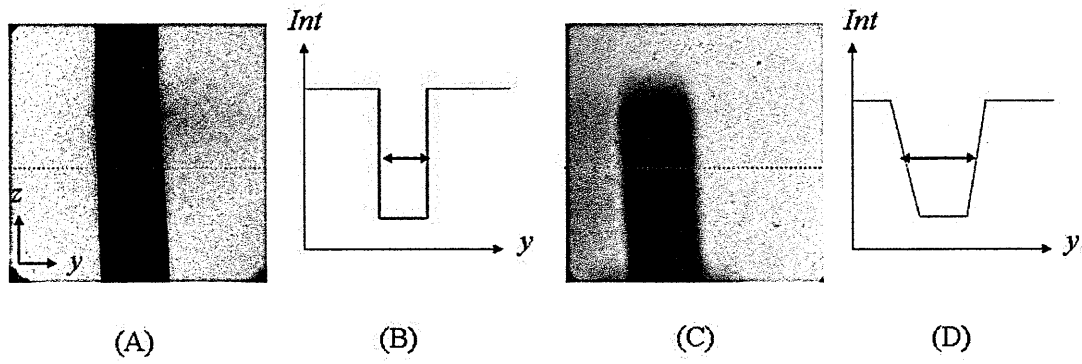

Figure 5.5: Cross sections used to determine the depth of field.

instability, such as unstable natural convection, were reduced by surrounding the Tesla coil with cardboard with two holes cut out at the height of the electrodes to allow the light to propogate through. In addition, the air conditioning in the laboratory was switch off during measurement. For controlled positioning, the camera was mounted on a dual-axis stage and adjusted so that the object was imaged onto the centre of the CCD array. The extended light source leads to small deviations from a truly collimated beam in the test area and adds depth of field to the system with a region along the optical axis being sharply in focus. The length of this region should exceed the plasma dimensions to avoid defocussing at the image plane. The depth of field was assessed by measuring the image sharpness from a test object positioned at several points in the test path (figure 5.5). A cross-section was extracted from the image of the resistor (A). When sharply focussed, the FWHM of the cross-section is at a minimum distance (B). The resistor was then moved along the optical axis to find the distance limits where the cross-section starts to defocus (C). At this point the FWHM starts to increase and an acceptance limit of a nominal 10 pixels was taken as the point where the image would be defocussed (D); for the resistor width of 7.2 mm this is equivalent to an increase in width of 0.27 mm. The results show the region where the resistor is sharply focussed is approximately 35 mm which exceeds the discharge dimensions.

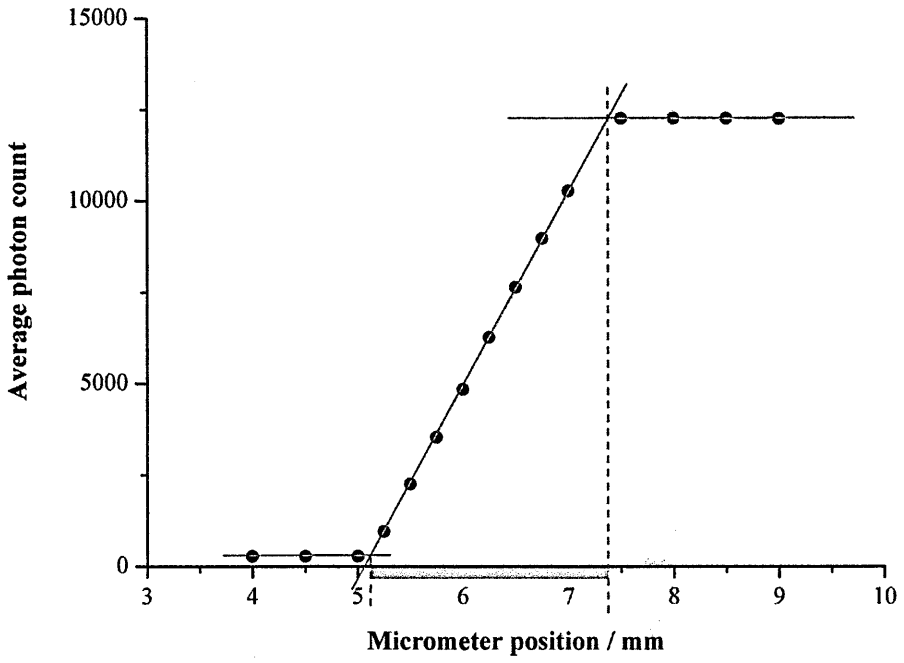

Figure 5.6: The average pixel intensity as a function of the razor's micrometer position for a 2.28 mm source width.

5.3.3 Cutoff level and alignment

The procedure to determine the uncovered image width, a, is described in this section. Equation 5.6 shows this to be a key parameter for the calculation of the deflection angle and good accuracy is required to avoid large disrepancies in the calculated temperature profile. To calculate the image width, the average pixel intensity was measured (without any plasma) as a function of the razor blade edge position as it was moved into the focus. The razor blade was mounted on the travel stage and inserted from a nominal starting position outside the focal plane image of the source. At each position, the average pixel intensity from the CCD was calculated until the source image was completely blocked, at which point a nominal background level was measured. Figure 5.6 gives the resulting average intensity as a function of micrometer position. A linear extrapolation through the slope to the averaged 'open' and 'blocked' intensities gives the image width. Several repeat measurements using this procedure gave an overall accuracy of $\pm$ 0.02 mm for an image width of 2 mm so an uncertainty of $\pm$ 1 % is achieved in the determination of the image width, a.

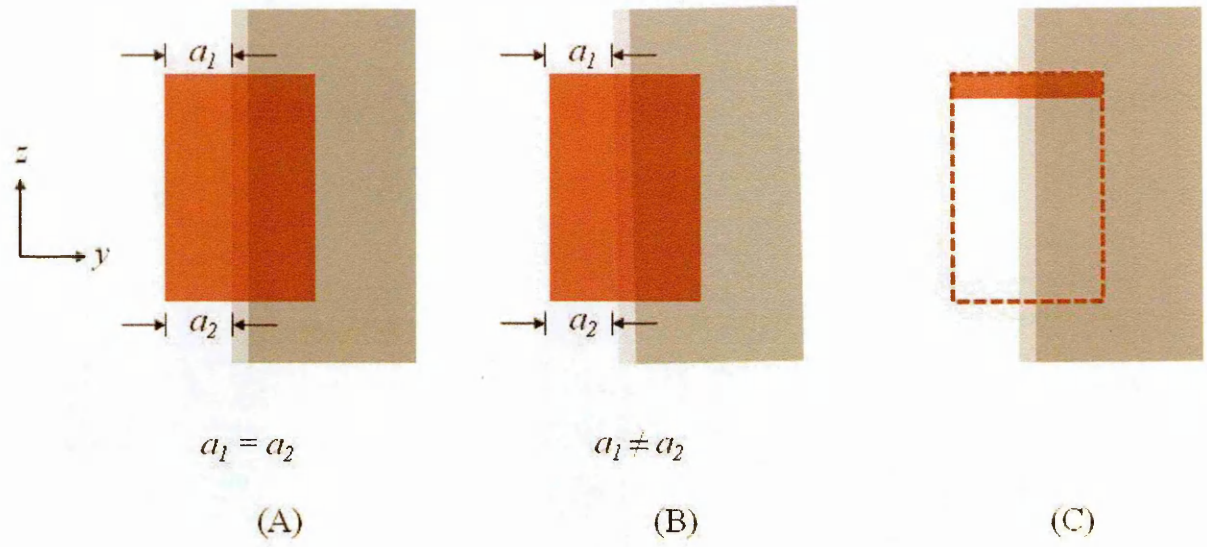

Figure 5.7: The misalignment of the razor edge can lead to inaccuracies in the deflection angle calculation; (A) the razor is aligned with the source image, (B) the razor is misaligned relative to the image and (C) the source image masked to assess the effects of misalignment.

A further measurement was made to assess the alignment between the source image and the razor blade edge. Ideally, the uncovered width should be uniform along the height of the image (figure 5.7 - A). A non-uniform width will result from mis-alignment of the razor or slit (figure 5.7 - B) and, again, leads ultimately to inaccuracies in the radial temperature profile. The source slit was masked to leave a narrow region, at the top (5.7 - C) and then at the bottom. The cutoff procedure was completed for the two configurations and the image width calculated for both regions with one measurement and a repeat completed. The two regions show a difference in the calculated widths of 0.01 mm which can be traced back to the variation along the length of the adjustable slit. This is small compared with the dimensions of the source and, when applied in equation 5.6, translates to a change in the peak temperature of $\pm$ 100 K around an initial value of 2500 K. The position of the razor edge along the optical axis was also explored. A uniform background illuminance depends on the cutoff being positioned correctly along the optical axis (figure 5.8). When the razor edge is positioned before or after the source image (A,B), the projected image shows sharp gradients in intensity whereas when the razor edge is positioned optimally at the focus (C) the projected image shows a uniform background. The effect of this on a calculated temperature pro-

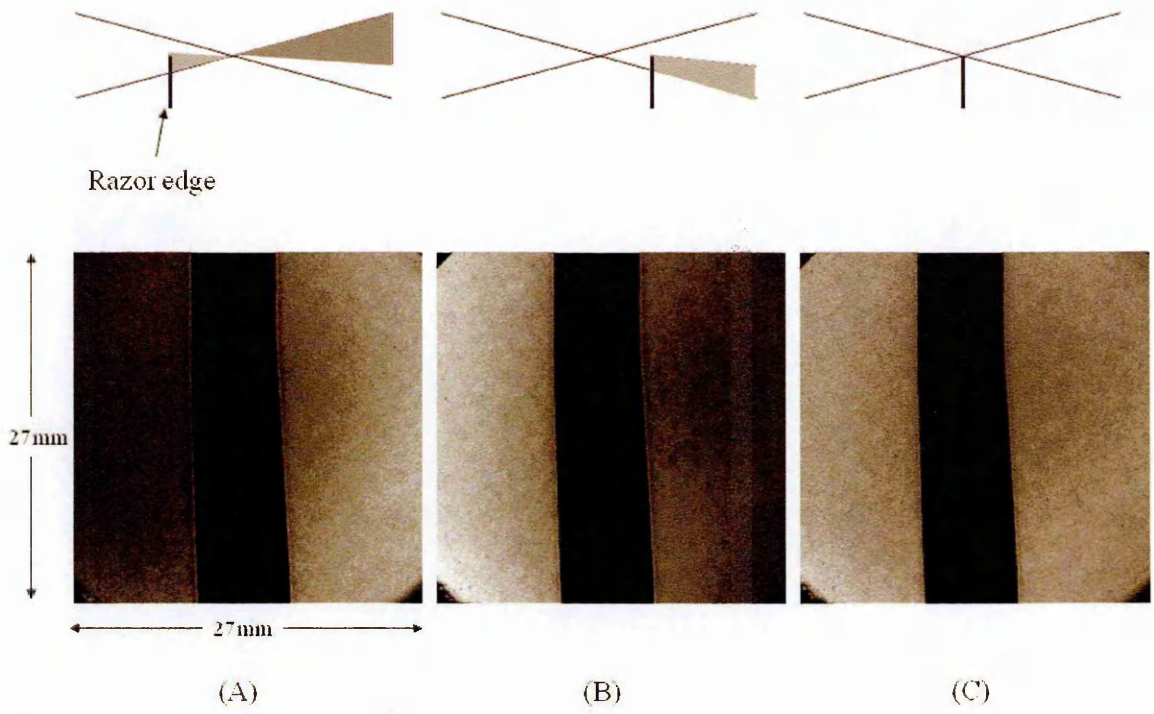

Figure 5.8: Imagess of a resistor with the razor edge at three positions along the optical axis; before the focus (A), after the focus (B) and at the correct position at the focus (C).

file appears minimal due to the background correction compensating for non-uniform illumination; this process will be described in the next section. For reference, the background illumination remains uniform over a 3 mm range when measured by moving the razor along the axis and, for best practice, the razor was positioned in this range prior to measurement.

5.3.4 Cut-off examples

To complement the description of cut-off given in section 5.2.1, results of schlieren imaging of the RF plasma taken for several cutoff levels are shown in figure 5.9. For a 70 % cutoff, the schlier can be observed but becomes more distinct as the cutoff level is increased. At 90 %, the increase in the contrast highlights previously unseen heating around the bottom electrode. When the cutoff is increased to 98 %, the dark region shows no change in contrast and is an example of overranging. For clarification, the dark and light regions in these images corresponds to the insertion of the razor blade being inserted from the right side into the source image as pictured in figure 5.3. If

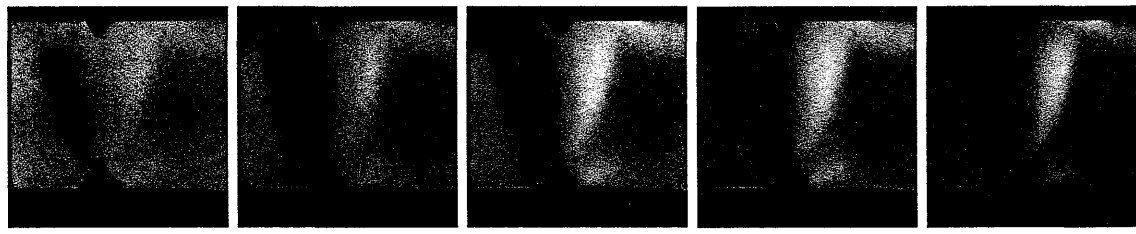

Figure 5.9: Schlieren images of the plasma using increasing cutoff levels shows the increasing contrast changes.

the razor edge is inserted from the left, the dark and light regions in the image would reverse.

5.3.5 Optical component tolerances

The lens quality will influence the ability to distinguish finer detail in a schlieren image and, for the optics in this set-up, a surface quality of $\lambda/4$ was used which exceeds the minimum required for quantitative work [60]. Chromatic abberations were not important owing to the (near-monochromatic) filtering at 670 nm. Similarly, spherical abberations were judged to have a negligible effect. The deflections occur mainly on, or close to, the central axis so the lens edge, where abberations are greatest, contributes little to the imaging. The tolerance of the focusing lens was included in the uncertainty analysis due to the presence of the nominal focal length in equation 5.6. From the manufacturer's specification, this was taken as $\pm$ 1 % which, when applied in equation 5.6, translates to an uncertainty in temperature of $\pm$ 100 K at 2500 K.

5.4 Theory and analysis

In this section the analysis used to convert the image acquired at the CCD array to a radial temperature profile will be explained. The process involves the use of the Abel-transform and is implicitly based on cylindrical symmetry in the test field. A validation of the calculations using known test functions is also presented.

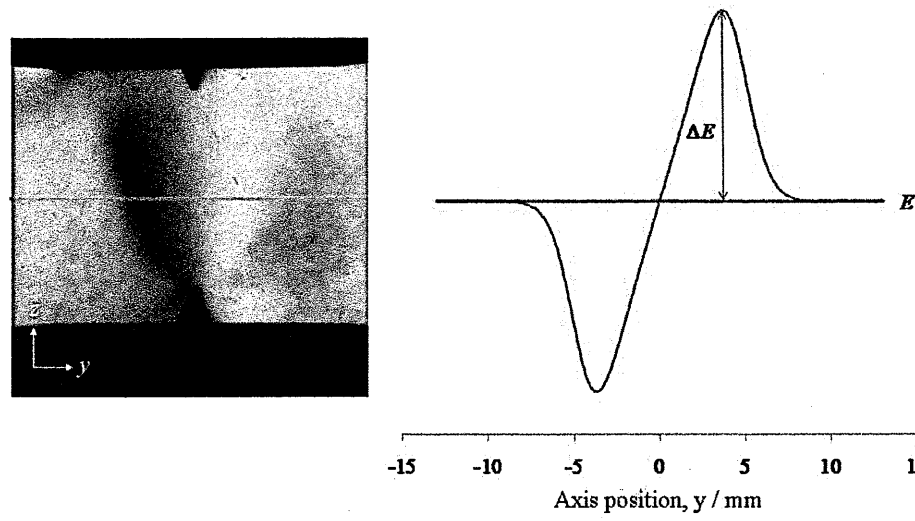

Figure 5.10: A cross-section extracted from the plasma image is used for analysis.

5.4.1 Theory

An intensity profile is taken from the plasma image in figure 5.10 in order to show the difference in illumination, ΔE, caused by the angular deflection, relative to the reference illumination level, E; for reference, the $y = 0$ mm point is always taken as the point along the profile where the intensity, E, is equal to the background at the end points. A negative axial position around this zero point crossing is applied. Just as the uncovered width is proportional to the reference illumination level in an image, the displacement is proportional to the difference in illumination. This can be expressed as follows:

$$\frac{\Delta a}{a} = \frac{\Delta E}{E} \tag{5.5}$$

Using equation 5.2, a direct relationship between the measured intensity profile in figure 5.10 and the deflection angle at the source as a function of axial position can be obtained from:

$$\varepsilon = \frac{a}{f_{\text{foc}}} \frac{\Delta E}{E} \tag{5.6}$$

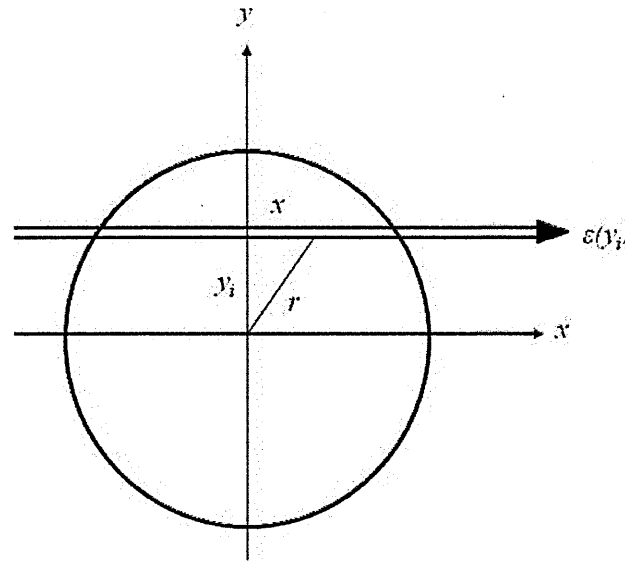

Figure 5.11: The Abel transform showing the line integrated intensity (and deflection angle) obtained along a chord at a distance y_i from the centre

This form of the equation includes all the key parameters in the Schlieren system and has been used for all the calculations of the deflection angle in this chapter.

5.4.2 Abel transform

The cylindrical symmetry of the plasma is compatible with the use of Abel transforms for analysis and has been used in the schlieren analysis for other plasma arc sources [61, 62]. The process involves the use of the Abel transform to take the radial distribution function and calculate the integrated line intensity seen by an observer. Figure 5.11 shows a chord at a distance y_i from the centre through a cross-section of the plasma in the x-y plane. The integration of a finite number of chords builds up the intensity distribution in figure 5.10. The deflection angle and its relation to the refractive index $n(r)$ are related by the following pair of of transforms,

$$\varepsilon(y) = 2y \int_y^\infty \frac{d(n-1)}{dr} \frac{dr}{(r^2 - y^2)^{1/2}} \tag{5.7}$$

$$n(r) - 1 = \frac{-1}{\pi} \int_r^\infty \varepsilon(y) \frac{dy}{(y^2 - r^2)^{1/2}} \tag{5.8}$$

where $n(r)$-1 is the radially dependent change in the refractive index [61].

The refractivity and gas density are related through the empirical Gladstone-Dale relation,

$$n(r) - 1 = \kappa\rho(r) \tag{5.9}$$

where the Gladstone-Dale coefficient for air is $\kappa = 0.23\text{x}10^{-3}$ m^3/kg [60]. This relation is assumed to be linear up to the gas temperatures expected in the plasma; significant deviations could occur from the gas composition but this was estimated to have a negligible effect on the measurement with this plasma. The temperature profile was calculated from the gas density using the ideal gas law,

$$T(r) = \frac{p}{\rho(r)R_s} \tag{5.10}$$

where p = atmospheric pressure, $R_s = R/M$ is the *specific* gas constant, R = universal gas constant and M = molar mass of the gas. This form of the ideal gas law, using the specific gas constant, accommodates the gas density term from the Gladstone-Dale relation. To calculate the molar mass, the atomic weights for the nitrogen, oxygen and argon species were taken from reference data [48]. Two methods of analysis were used; (1) the Abel transform was used to calculate the deflection angle from a model temperature profile then fitted to a measured intensity profile and (2) the measured intensity profile was directly inverted with the Abel transform to calculate the radial temperature profile. Both methods were investigated and are described shortly.

5.4.3 Data conditioning

The Abel transform is susceptible to noise amplification so prior to determining the radial temperature profile directly from the intensity data, the profile was corrected and smoothed. As described previously in section 3.3.1, the raw intensity profile had flat-field and background corrections applied (figure 5.12 - A-B). The profile was then averaged with the adjacent 10 profiles along the z-axis and a 10 point moving average was applied to the data in the y-direction to smooth it further, resulting in the intensity profile under analysis (figure 5.12 - C). Equation 5.6 was then used to determine the

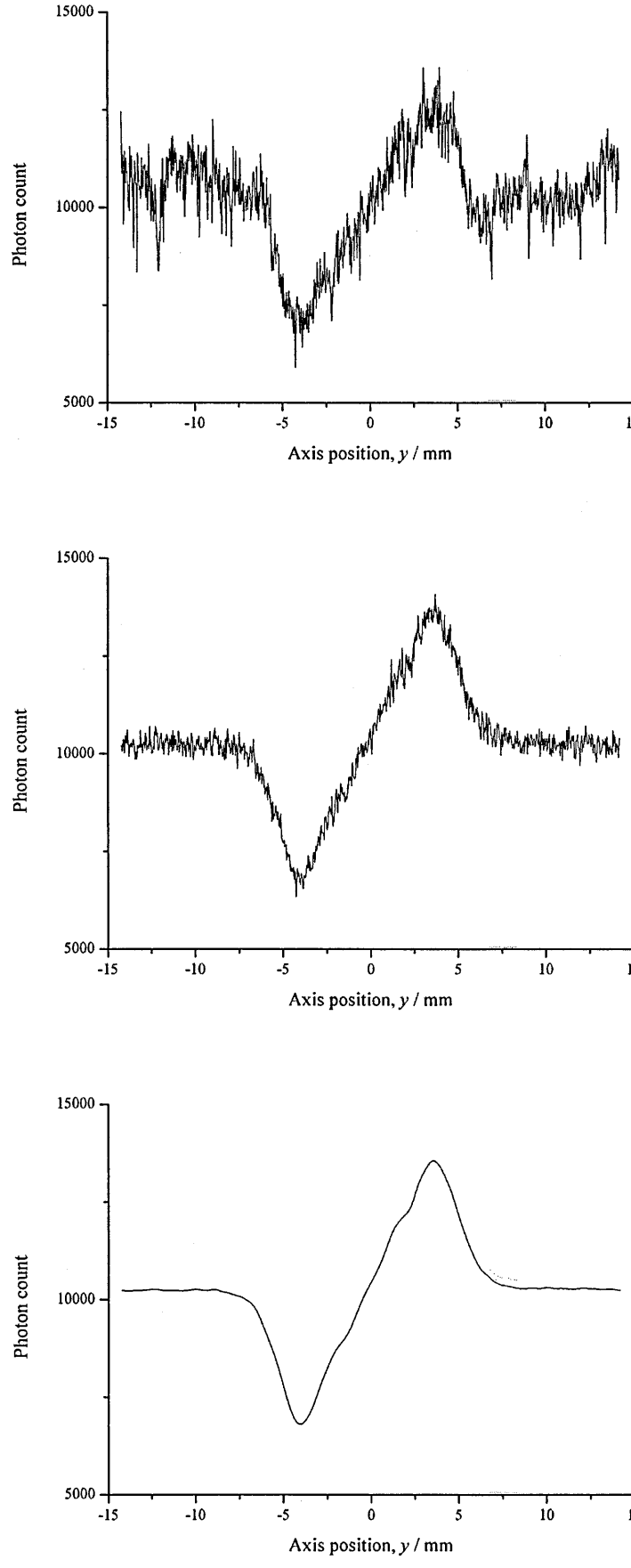

Figure 5.12: The stages of the data treatment; raw data (A), flat-field and background corrected (B) and averaged/smoothed (C)

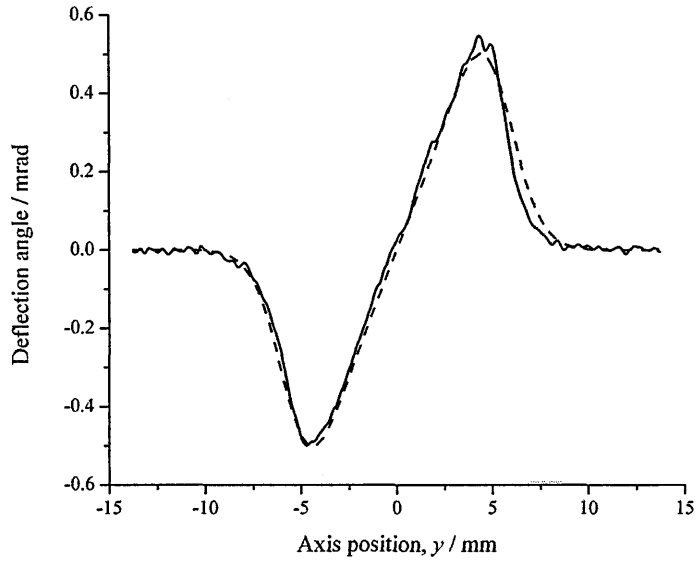

Figure 5.13: An example model fit (dash) to a measured deflection angle profile (solid) at $z = 6$ mm and for an rms conduction current of 18 mA.

deflection angle from the dependent variable (photon count). Due to the averaging, the spatial resolution is limited to approximately 0.30 mm along the z-axis based on the pixel rsesolution calculated in section 5.3.1.

5.4.4 Fitting and inversion methods

For the fitting method, the deflection angle was calculated from a continuous, Gaussian function of the following form:

$$T_g(r) = T_{max} exp(\frac{-(\frac{R}{\sigma})^2}{2}) \tag{5.11}$$

where T_{max} is the on-axis peak temperature and σ defines the profile's radial width; these two variables define the modelled temperature profile. The refractive index term was calculated from the temperature profile using the ideal gas law and the deflection angle was calculated using equation 5.7. The goodness of fit between the two profiles was optimised by adjusting the variable parameters until the rms error was at a minimum (figure 5.13).

For the Abel-transform, a faithful reproduction of a radial temperature profile occurs when a continuous function is used. As the measured profile is a discrete data set,

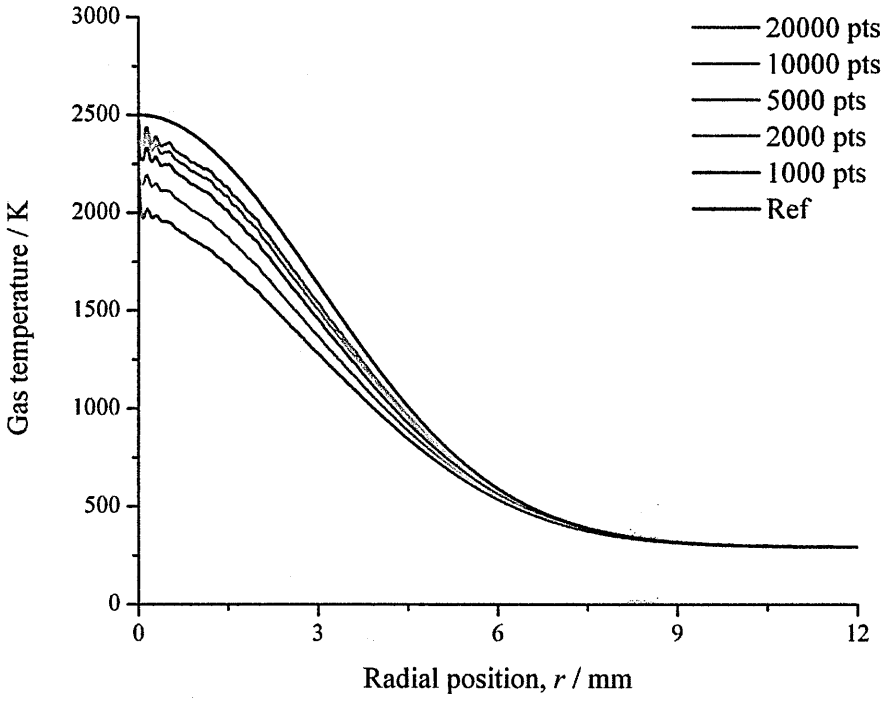

Figure 5.14: The Abel-transformed radial temperature profiles for several points functions compared to the original temeprature profile.

an interpolation function was used to fit cubic splines to the measured profile before inversion. This approach was validated by creating several deflection angle profiles (as for the fitting method), using them in the transform algorithm then comparing the transformed and original temperature profiles. Figure 5.14 shows the temperature profiles approaching the reference profile as the number of points used in the cubic spline fitting is increased, though this improvement is at the expense of the calculation time. The profiles starts to converge as the points are increased further and the fit to the reference profile ceases to improve. The difference in the on-axis temperature between the reference profile and that obtained with the 20000 points reconstruction is 150 K in 2500 K (or around 6 %). Where this transform was used in the analysis, the results were corrected by this percentage to correct for the difference.

The effect of noise on a profile was also investigated. A random number generator was used to create random noise, typical of that on a measured profile after smoothing, which was then applied to the modelled deflection angle before inverting. The comparison between the reference profile (no noise) and with noise applied shown in

comparison between the reference profile (no noise) and with noise applied shown in

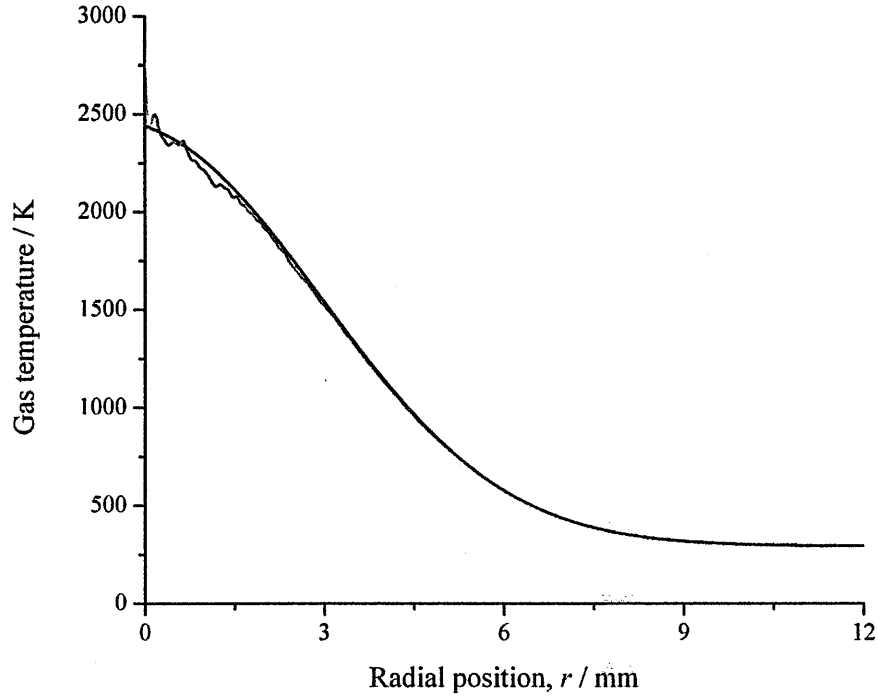

Figure 5.15: The temperature profile obtained through inversion of a test function without noise (black) and with 2% noise level (red).

figure 5.15, reveals that, while there are slight variations of around $\pm$ 25 K on-axis, the temperature profile is maintained.

5.5 Calibration

To give confidence in the results, a 'calibration' of the schlieren system was undertaken. The radial temperature profile of a heated resistor was measured through independent means and reference values obtained for the typical combustion temperature of a propane gas jet. The two sources cover the temperature range that the schlieren system would be expected to measure.

5.5.1 Heated resistor

A 1 Ω/12 W resistor was used as a test heat source and the temperature field it produced was measured using a thermocouple. The resistor was secured vertically and connected to a high current power supply. A type-K thermocouple was mounted on a translation stage (as used also for the razor edge cutoff) and positioned perpendicular

Figure 5.16: A schlieren image of the resistor pre-heating (left) and in steady state heating (right).

to the resistor surface. The resistor was heated with a 6 A direct current from the power supply and after switching on, was left for a period to reach steady state heating. The temperature was measured in the radial direction by moving the thermocouple away in known increments. It is assumed that convection and conduction are the dominant form of heat transfer but radiation was accommodated by altering the orientation of the thermocouple so that the junction was perpendicular to the resistor. The resistor was then placed centrally in the schlieren test path. A 65% cutoff was applied with pre- and post- heating images of resistor heating are given in figure 5.16. A cross-section profile was extracted from the middle of the image, the intensity profile smoothed and the data inverted.

The reference and schlieren profiles are given in figure 5.17. The thermocouple results were calculated from an average of four independent measurements with the uncertainty being a combination of the random measurement uncertainty and a systematic component taken from the manufacturer's specification. The region occupied by the resistor has been included on the plot for reference. The red and blue lines show the temperature profiles calculated from the dark (left) and light (right) regions of a schlieren profile. The grey area indicates a region where diffraction around the resistor causes errors during the data processing and data points within this region were discarded. There is reasonable correlation between the two methods with the schlieren

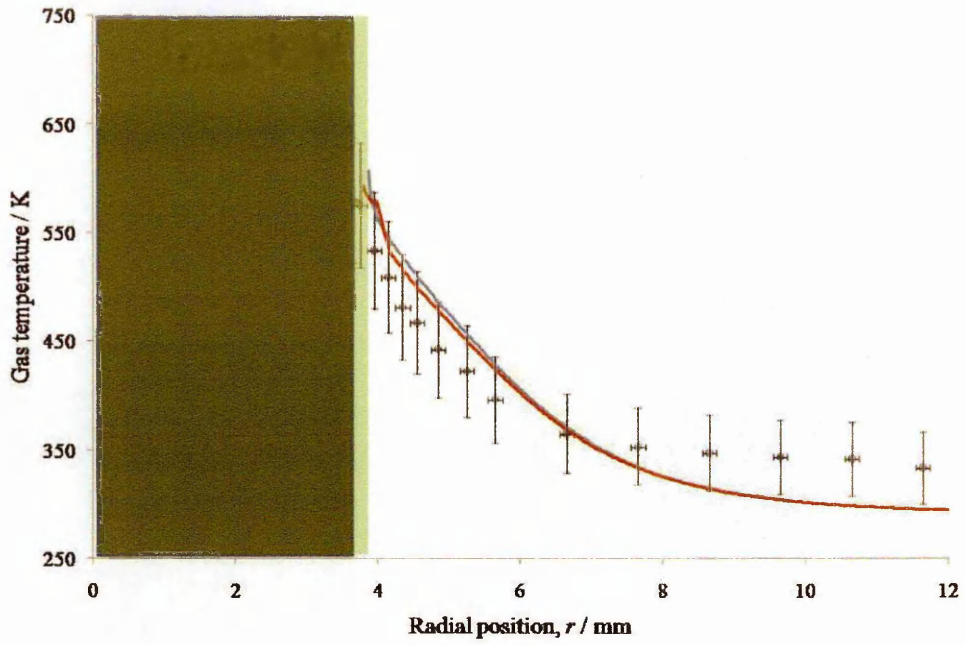

Figure 5.17: The temperature profile from a heated resistor measured using a thermocouple (squares) and determined through Abel inversion of the Schlieren profile (line).

profile lying within the uncertainty of the reference measurements. The surface of the resistor is approximately 600-625 K and an equivalent temperature on the Schlieren profile is around 650 K when extrapolated. While the Schlieren result lies above the reference within $r < 8$ mm, the reverse occurs when $r > 8$ mm. It is unclear why this trend occurs. Accurate temperature measurement using the thermocouple rely on the reference junction remaining at a constant temperature relative to the measuring junction where the heating occurs. Generally, the thermocouple instrumentation is well compensated for this and the differences seen may indicate the minimum detectable temperature in the Schlieren set-up. As a precaution a difference of $\pm$ 50 K was attached to a measured result.

The spatial dependence of a data set was assessed by determining the temperature profile from the line-of-sight intensity profile at 0.5 mm increments in the z-axis direction. Taking a reference point of $r = 4$ mm, the spread in temperature from five profiles was around 80 K. An allowance should be made for the stability of the steady-state gas flow around the resistor during heating. Although all external sources of disruption were eliminated, the convective flow can itself cause inhomogenities in the refracting medium. However, $\pm$ 50 K variation along the length of the axis has been appied as

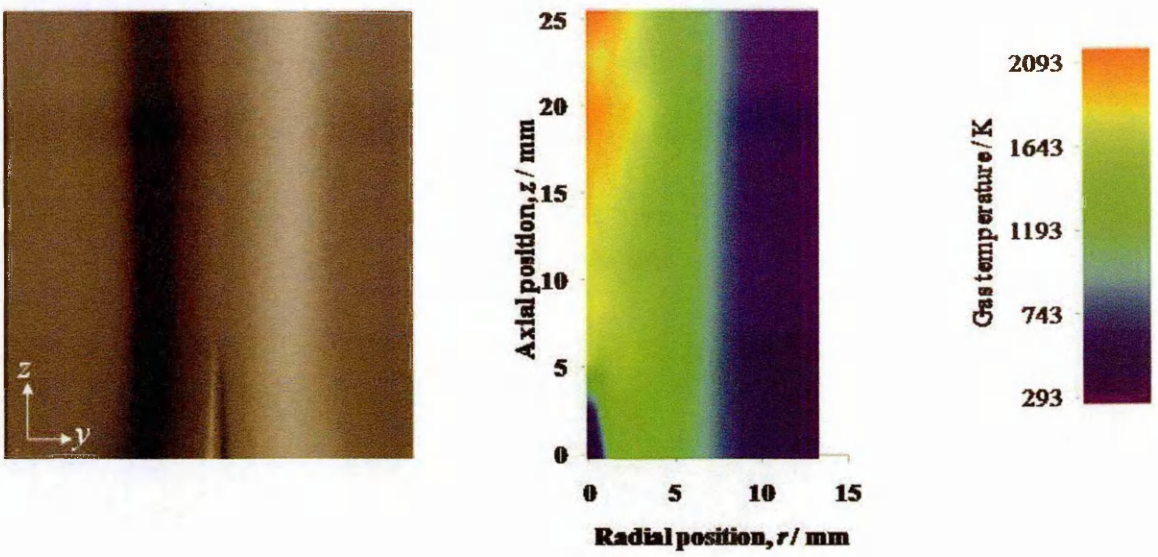

Figure 5.18: A propane gas jet image at a point 5mm above the nozzle (left) and the corresponding surface plot for the radial temperature distribution (right); spatial dimensions, $z = 27$ mm, $r = 13$ mm.

an uncertainty for spatial dependence.

5.5.2 Propane gas jet

The measurement of the resistor was practical up to 650 K and suggests the system is linear up to the predicted high gas temperatures. The rotational measurements show this to be in the region of 2500 K so for further confidence, a propane gas jet was used as a second reference source. The temperature of the jet was measured independently with a thermocouple at a single point in the jet which was judged to be the hottest region. The temperature was in the region of 1690 K; reference values for a combustion of a propane/air mix are around 2250 K [66]. The jet was positioned vertically in the test path and imaged from a few millimetres above the output nozzle (figure 5.18). A surface plot was constructed from the axially-dependent, radial temperature profiles and shows the spread in results ranges from 1700 - 2000 K with the greatest heating lying on axis, 25-30 mm from the nozzle. This lies above that measured through the thermocouple. However, calculation using the Abel reverse transform shows a greater variation in the temperature profile (as will be described shortly). A higher uncertainty in the result would apply and the reference value measured using the thermocouple comes within

the uncertainty of the on-axis temperature values derived through schlieren.

The radial temperature drops off to the ambient background level where $r \geq 10$ mm. Another feature of the image is the narrow region just above the nozzle where a reversal in contrast is seen. This results from a negative refractive index gradient indicating the region is cooler than the surrounding flame here, because sufficient oxygen is unable to enter the central region of the nozzle so the burn front is unable to propogate further and no combustion of the gas mix occurs.

5.5.3 Summary

Measurements of two reference heat sources were made using the Schlieren method and compared to the available reference information. For both the resistor and the propane jet, the results were in reasonable agreement with reference values though an additional uncertainty has been noted based on the differences seen with the resistor results.

5.6 Preliminary results using the plasma

Following from the systematic checks and calibration with the resistor, the response of the system to the plasma was assessed. The preliminary results are designed to identify behavioural characteristics of the plasma that would impact on the measurement accuracy. Understanding these effects identifies appropriate acquisition and setting up procedures so that systematic effects can be minimised.

5.6.1 Repeatability

The plasma was placed centrally in the test region and an assessment made of the repeatability by making several consecutive measurements at one current setting. Deflection angle profiles and the respective temperature profiles were compared. Two shutter times were used 0.1 s and 10 s. The results show the deflection angle profile to be more stable for the longer shutter time though large temperature variations occur when the temperature profile is calculated. Figure 5.19 shows four expanded deflection angle profiles (light region) acquired consecutively with the optical set-up unchanged

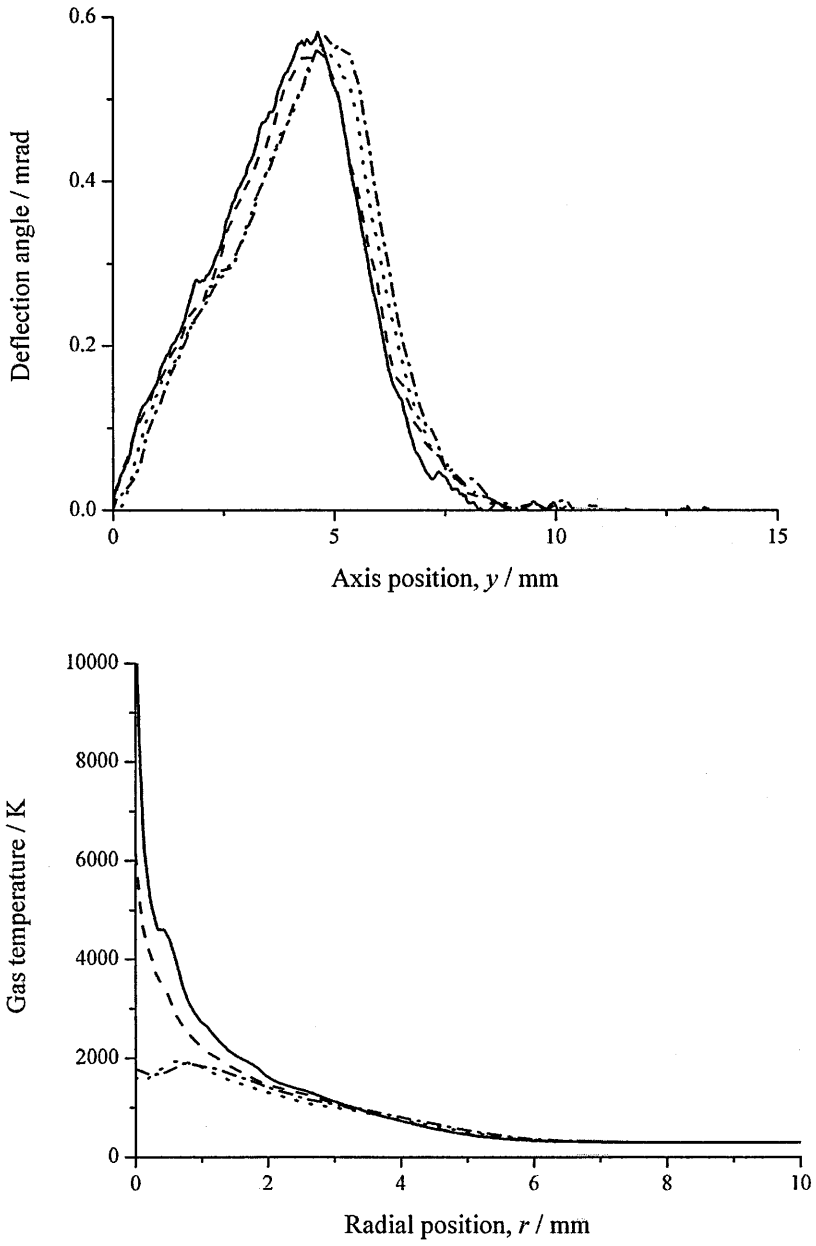

Figure 5.19: Four deflection angle profiles (top) acquired consecutively from a 10 s shutter time and the resulting temperature profile calculated from the Abel transform (bottom).

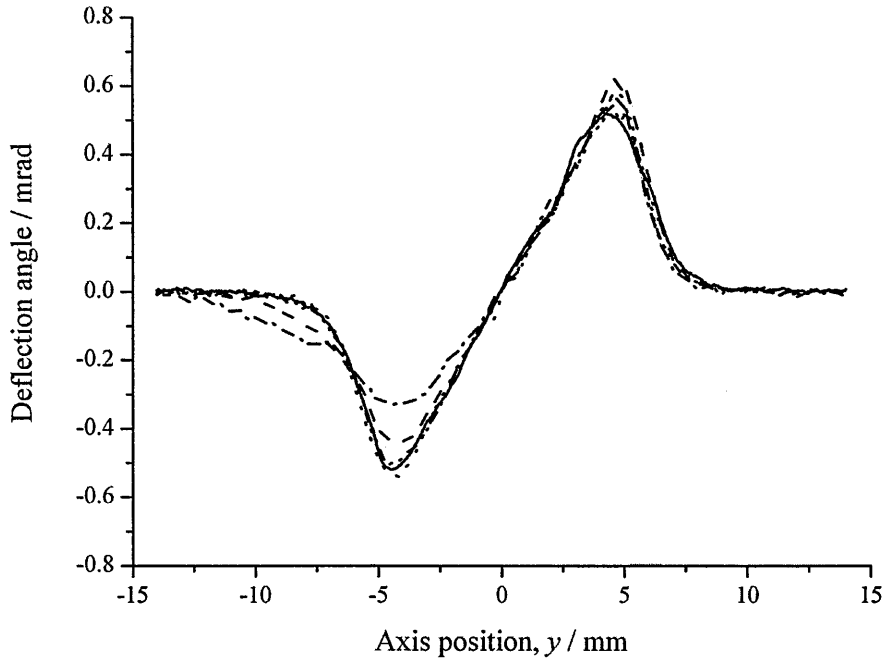

Figure 5.20: Four independent measurements which reflects the variation in the line-of-sight intensity profile.

and using a long shutter time of 10 s. The corresponding radial temperature distribution is given and shows a close spread in results for radial distance in the range, $r > 2$ mm but this spread increases significantly around the central axis for $r < 2$ mm; the spread in the peak temperature is in excess of 5000 K. As the experimental set-up was unchanged, the results appear to reflect the variation from effects within the plasma. To be sure, additional systematic studies were completed, considering the plasma alignment and the optical set-up. Moving the plasma in controlled increments off-axis from a nominal centre position to test the alignment, shows no significant difference from profiles in figure 5.19. The optical components were tested by completing a number of independent repeats where the schlieren system was dismantled and re-assembled prior to measurement. Again, this produced a similar variation to that in figure 5.19. Both of these tests suggest that variations may be a consequence of the plasma's random flickering from convective gas instabilites.

The deflection angle profiles from the independent repeats show two profiles that deviate significantly from symmetry (figure 5.20). The plasma loses its symmetry

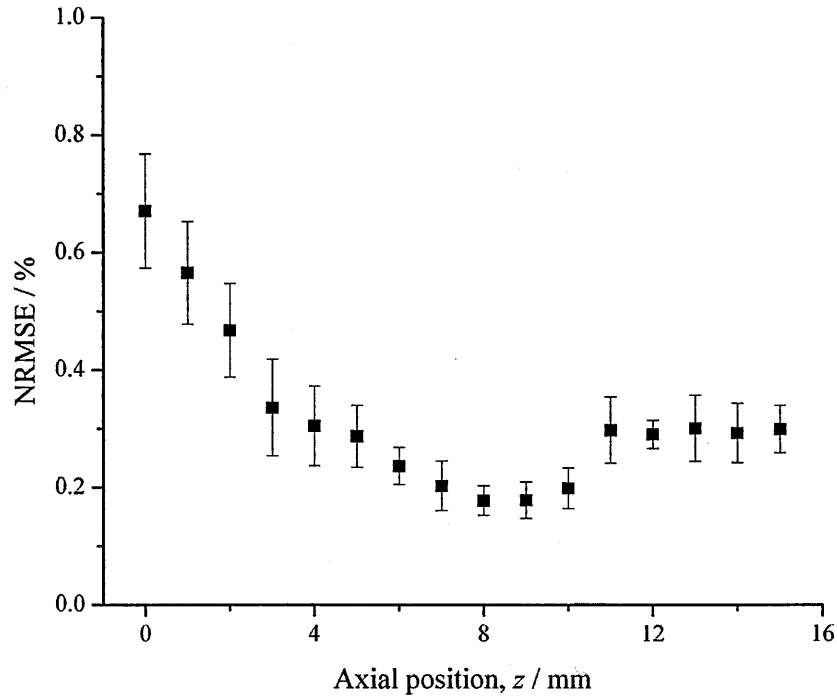

Figure 5.21: The normalised rms error as a function of axial position calculated for I_{rms} = 18 mA with the standard random uncertainty, u_a, at each axial position calculated from 8 independent measurements.

while remaining stable for a long period relative to the shutter time. Observations of the plasma show this state can occur with the plasma rooting itself to one side of the electrode, causing slight curvature while remaining stable. However, attempts to reproduce the effect by deliberately misaligning the electrodes with respect to each other were unsuccessful (it had been thought that this would help to account for aspects of the variability of results for $r < 2$ mm). This leaves convective instability as the likely source of the problem.

Due to the random occurrence of the assymetric profiles, an acceptance criterion was introduced where the profiles of the light and dark regions were compared to each other. The rms error calculated between the two was used to determine the goodness of fit. This test was used on several data sets and the normalised rms error as a function of axial position, z, is given in figure 5.21.

The random uncertainty (u_a) was calculated from 8 independent measurements and shows the relative uncertainty increases toward the electrodes. This reflects the increasing asymmetry that occurs in this region and is illustrated in figure 5.22 taken from z = 0.5 mm. Using the fitting method, the spread in the results is $\pm$ 500 K

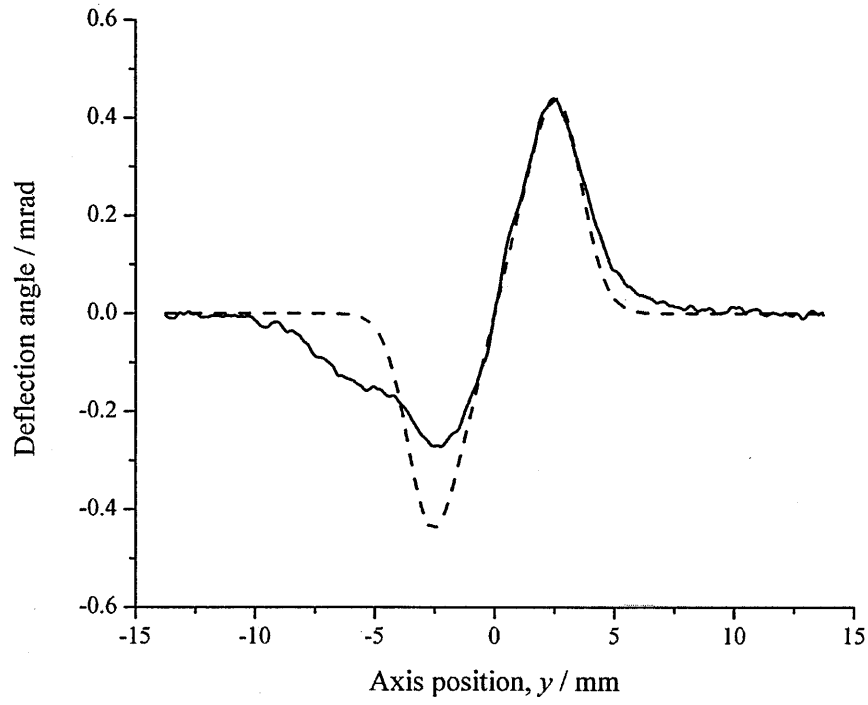

Figure 5.22: The deflection angle profile at $z = 0.5$ mm; measured (solid) and modelled (dash).

around an average peak temperature is 1000 K; this level of uncertainty relative to the measurand is essentially not acceptable and emphasises the need for exact cylindrical symmetry when using the Abel transform.

Aside from the analytical interpretation, the detail in the profile indicates a more turbulent region around the electrode where the previously assumed cylindrical symmetry does not apply. In this region, air is drawn in from a number of directions leading to the circulation and eddies that characterise a turbulent flow. The symmetry test described here excludes profiles such as the example given figure 5.22.

Some profiles (figure 5.23) with a much higher degree of symmetry have been recorded. However, there are still difficulties in finding a close fit at all points across the profile when compared to the near-symmetric example in figure 5.13. This results from the limitations of the gaussian used for the initial temperature profile and an alternative model function, such as a nth order polynomial, may provide a closer fit in this instance.

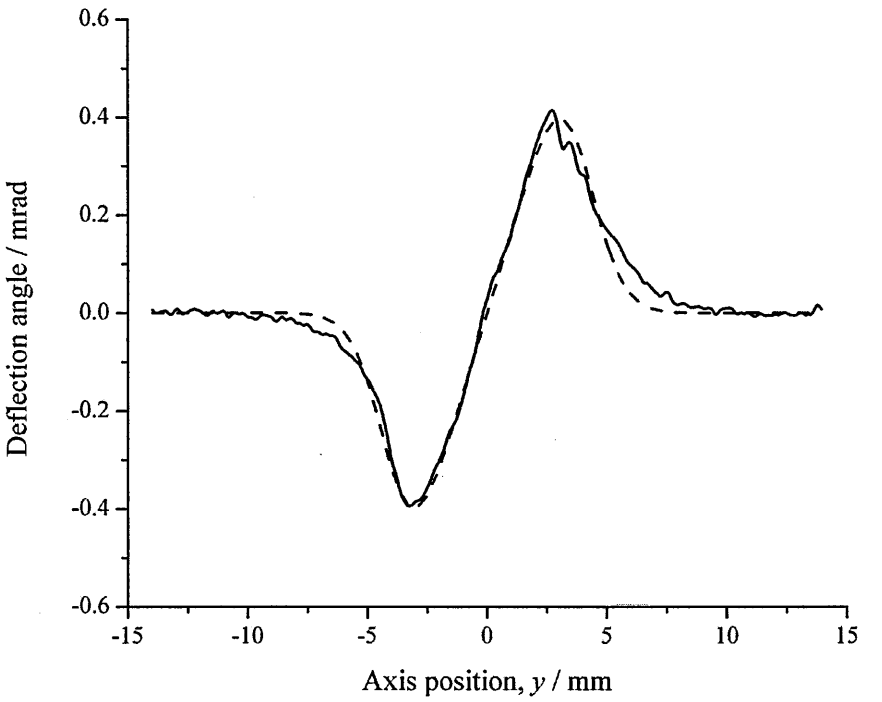

Figure 5.23: A near symmetric profile taken from $z = 0.5$ mm.

5.6.2 Summary

The measured profiles show detail which is most likely caused by instabilities within the plasma. While the variation may show a short term, random occurence within the plasma, the effect leads to a wider spread in the apparent temperatures. This indicates that a temperature profile calculated through transformation of such data is not representative of the long term temperature characteristics. This can be accommodated through fitting of a modelled profile to the measured one. The implementation of acceptance criteria on the intensity profile symmetry, based on the rms error to determine the closeness of fit between the modelled and measured profile, is adequate in ensuring the accuracy of the analysis. But the significance of the finer detail may need further investigation.

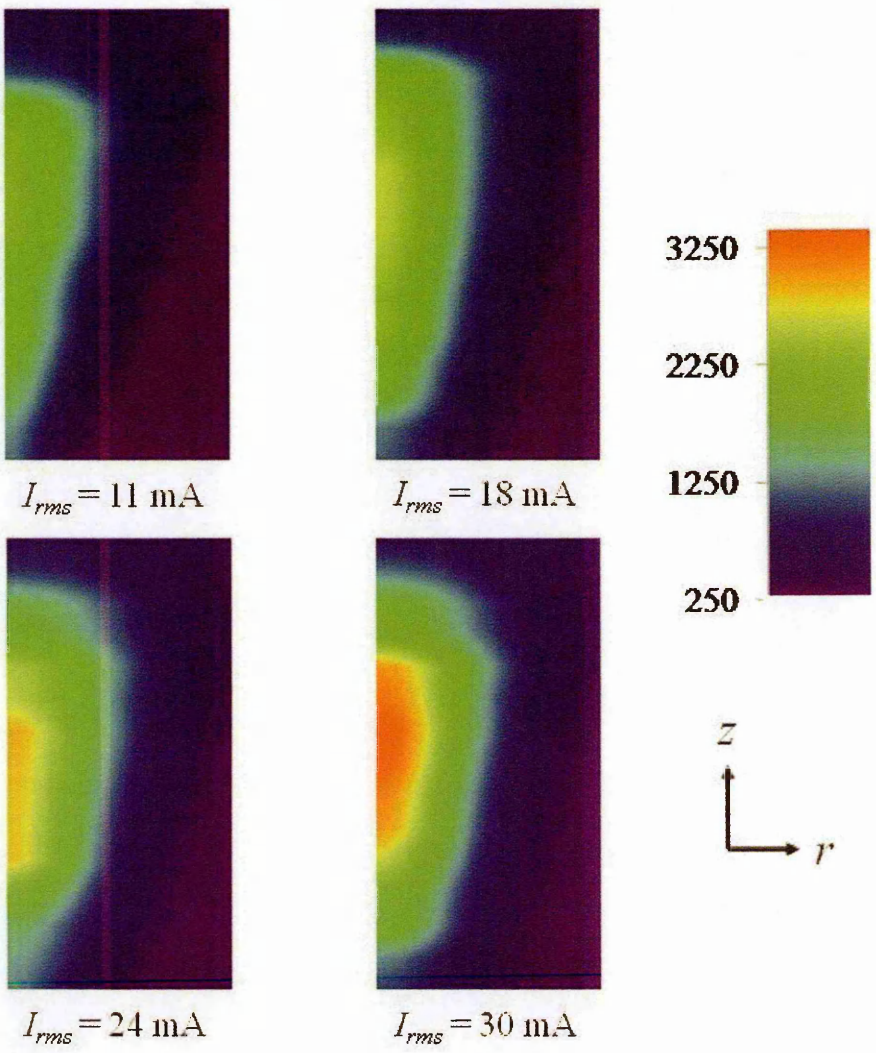

Figure 5.24: Surface plot for radial temperature profiles at four current settings; spatial scale $r = 7.5$ mm, $z = 15$mm.

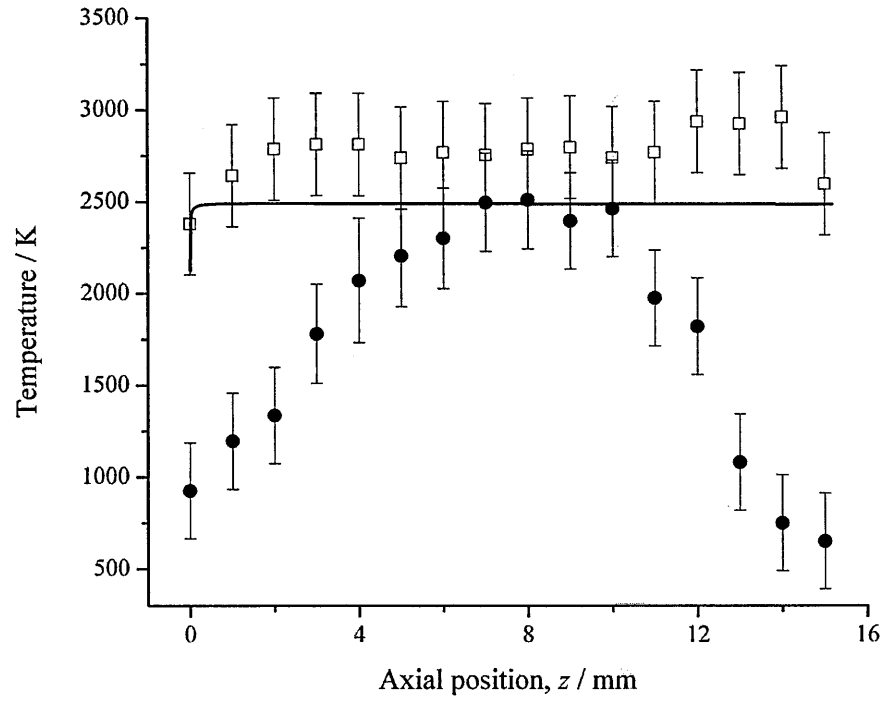

Figure 5.25: Axial gas temperature through Schlieren (circles), rotational temperature through spectroscopy (squares) and numerical model (line) for $I_{\rm rms} = 18$ mA.

.

5.7 Results for the steady-state plasma

The gas temperature plots in figure 5.24 were constructed from the radial temperature profiles determined through the fitting method and measured at 1 mm increment along the z -axis. This direct view of the gas heating around the plasma shows the gas temperature to increase with the conduction current as expected with the heating confined mainly to the central region. This leads to the broadening of the profile due to the increase in convection radially. The vertical asymmetry is detected and complements that previously seen in the optical emission.

The on-axis peak temperatures for $I_{rms} = 18$ mA are presented in figure 5.25 along with the comparable results for the rotational temperature and the gas temperature as calculated from the numerical model (presented previously in section 3.3.3). While the schlieren results are comparable in the central region of the plasma, significant deviations from the spectroscopy and model results occur in the electrode regions. The rms fitting error increases in this region in part due to fitting errors. An example of this is given in figure 5.26 taken for $z = 14$ mm.

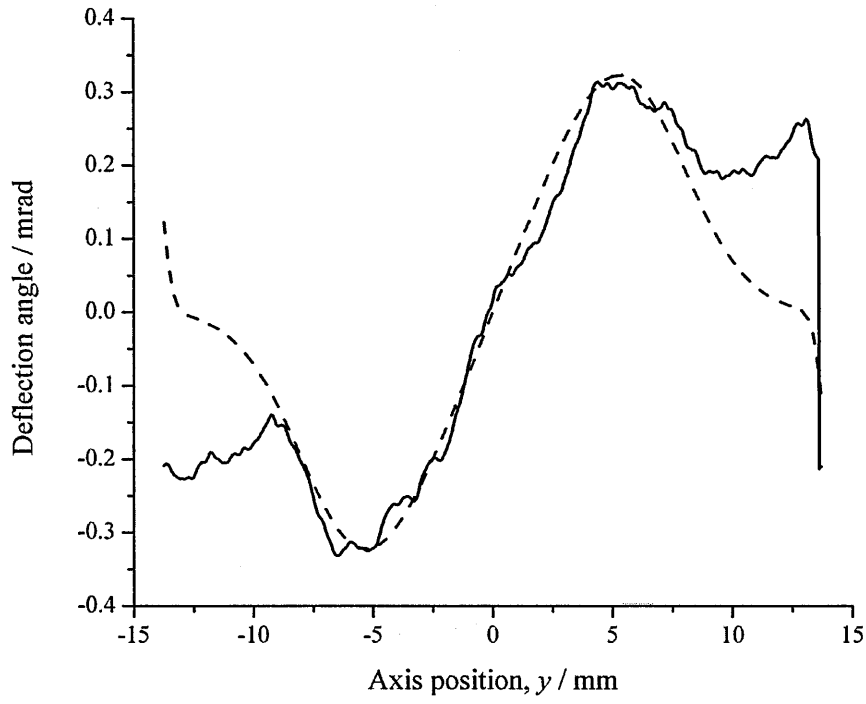

Figure 5.26: The deflection angle profile at $z = 14$ mm; measured (solid) and modelled (dash).

The deviations seen toward the extremes of the profile are a real effect and occur from the heat air deflected across the surface of the top electrode and contributing that results in further refractive index gradients and beam deflection. In this respect the model fits to the main central region, between -7.5 mm $< y <$ 7.5 mm, but is insufficient in its configuration to model the end regions. This leads to significant differences between the respective data points of the modelled and measured profiles from which the rms error is calculated. This is a further limitation of the model but on balance the deviations would have a negligible effect on the on-axis temperature and within a radial distance $r < 2$ mm; an Abel transform on this example profile shows a comparable peak temperature at $z = 14$ mm to that calculated through the fitting method.

Differences are seen when comparing the temperatures as a function of conduction current, I_{rms} as given in figure 5.27 for the results at an axial position, $z = 6$ mm. At higher currents, the gas and rotational temperatures converge within the measurement uncertainties but the opposite occurs for lower current settings with differences of up

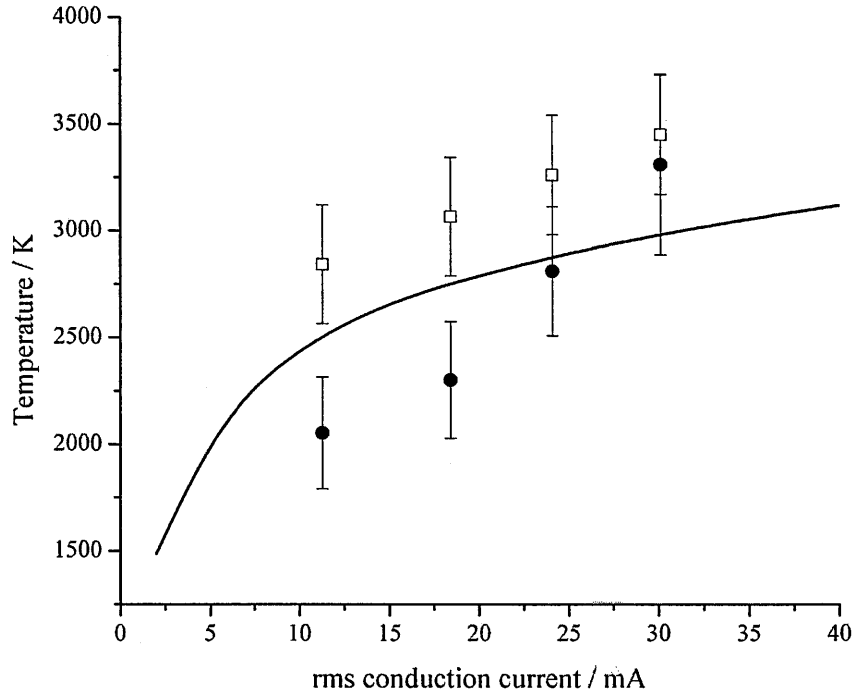

Figure 5.27: The on-axis gas temperature through Schlieren (solid circles), rotational temperature through spectroscopy (open squares) and numerical model (line) as a function of rms conduction current at $z = 6$ mm.

.

to 600 K between the two. Due to the short rotational to translational relaxation in nitrogen, it was assumed that they should be in equilibrium and the source of disequilibrium is not apparent. Confidence in the measurement system is gained from a combination of the systematic investigations and the calibration and indicate it to be unlikely that the difference is caused by factors associated with the experimental technique or the analysis. Disequilibrium could be maintained if there is insufficient time or space for collisions to couple the different energy stores.

When looking at the spatial dimensions, it is useful to recall the discharge radius calculated from the optical emission and presented in section 3.4.3. Figure 5.29 gives the gas temperature measured for conduction $I_{\text{rms}} = 18$ mA with the corresponding discharge radius measured as the half-width, half-maximum of the visible emission profile. A common trend can be seen between the two where the decreasing gas temperature occurs close to decrease in radius. With the length scales around the electrode, gas diffusion may be of significance. An approximate value for gas diffusion time constant,

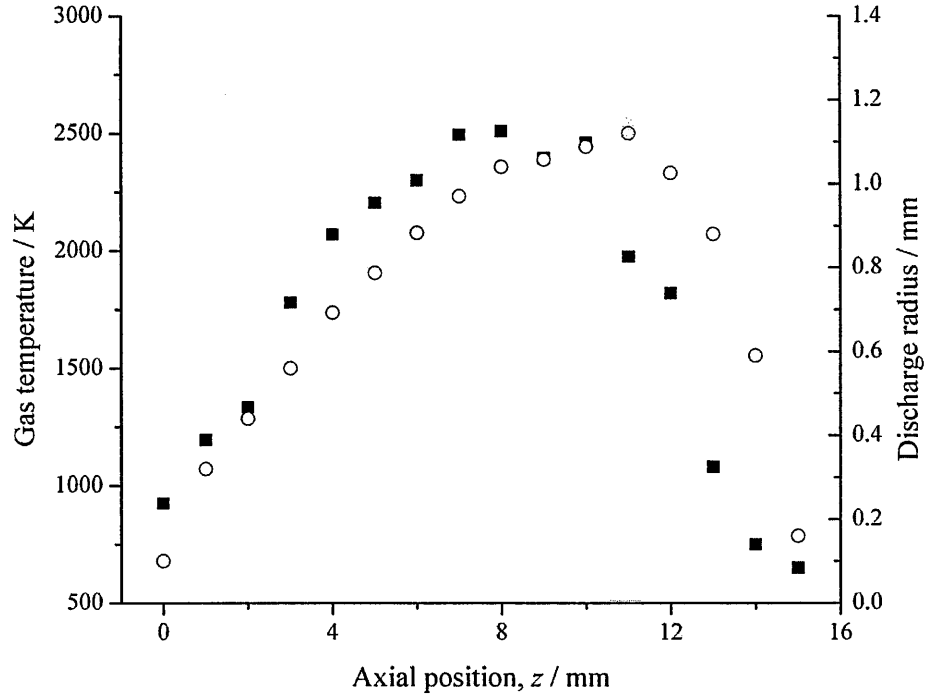

Figure 5.28: The (Schlieren) gas temperature (squares) and the discharge radius (circles) for a conduction current $I_{rms} = 18$ mA, as a function of axial position, z.

τ_{GD}, can be calculated using,

$$\tau_{GD} = \frac{L^2}{D_{N2}} \tag{5.12}$$

where L is the length scale (in this case the discharge radius) and D_{N2} is a gas diffusion coefficient for nitrogen. This is calculated from the analysis of Boulos et al [35] as follows,

$$D_{N2} = \frac{2}{3\sqrt{\pi}} \frac{1}{\sigma_{N2} P_{atm}} \sqrt{\frac{(k_b T_g)^3}{m_{N2}}} \tag{5.13}$$

where the T_g is the gas temperature (taken as 2500 K), P_{atm} is atmospheric pressure and σ_{N2} is the total cross-section for the nitrogen molecule. This gives an approximately value for D_{N2} of 64 m^2s^{-1}. Using this in equation 5.12 and taking the length scale, L, as 0.1 mm (the discharge radius at $z = 0$ mm) the timescale for diffusion is approximately 1x10^{-6} s and is less than that taken for V-T relaxation, typically 10-100μs in the plasma conditions here; the timescale for a 1 mm discharge radius in the plasma's main body is $\sim$ 1x10^{-4} and is a slower process than that for V-T relaxation. This diffusion in regions where the discharge radius narrows results in a lower number density of vibrationally-excited nitrogen molecules with which to transfer energy to the

translational stage. The comparison between the trends in the temperatures and radius as a function of current may be further indication of spatial dependence. In addition to the radius from the visible emission in figure 5.28, the radius calculated from N_2SP emission (and from which the rotational temperature can be related) is given. The respective gradients of the temperatures to the discharge radii indicates that the temperature and dimensions are closely coupled too. Rotational temperature occurs due to V-R relaxation and would mean that the initial assumption presented previously of translational to rotational equilibriation could be challenged. Further work is required to confirm the role of diffusion and if a condition on the spatial dimensions should apply.

5.7.1 Radial variation

Figure 5.30 shows the measured radial temperature profile measured at axial positions of $z = 6$ mm and 10 mm and for an rms conduction current of 18 mA. The expanded measurement uncertainty is included around the measured points (shaded). The *gas* temperature profile, calculated from the numerical model, is included for comparison. Both the measured and modelled temperature profiles show a steady drop off in temperature to an ambient background level beyond $r = 8$ mm and, for the measured profile, provides the fuller profile outside of the spectroscopically determined rotational temperature. The measured profile broadens with increasing axial position as reflects the axial and radial convection within the plasma. This dependence on broadening is reflected in the model results though the gas temperature value over part of the radial range lies marginally outside the measurement uncertainty.

5.8 Results for the plasma under modulation

The results of the plasma while under modulation as measured through schlieren imaging are presented in this section. In the unmodulated plasma, the steady-state condition of the variables that cause the changes in refractivity to occur (gas density) mean that a steady-state refractive index gradient will result. When under modulation, the changing relationship between gas temperature, gas density and refractive index should

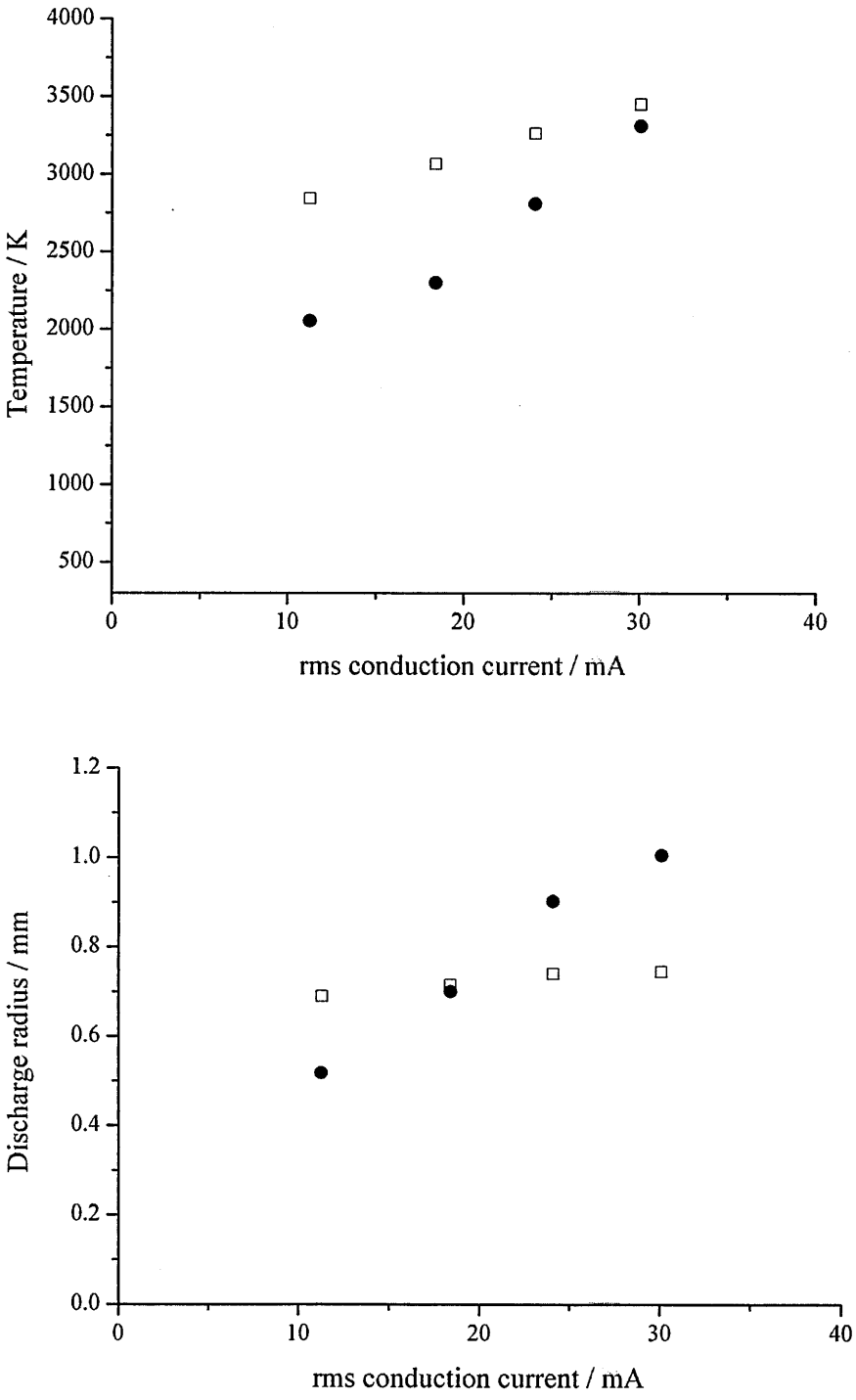

Figure 5.29: The temperature (top) - T_g (circles) and T_r (squares) - and discharge radius (bottom) - visible (circles) and UV radius (square) - as a function of conduction current at $z = 4$ mm.

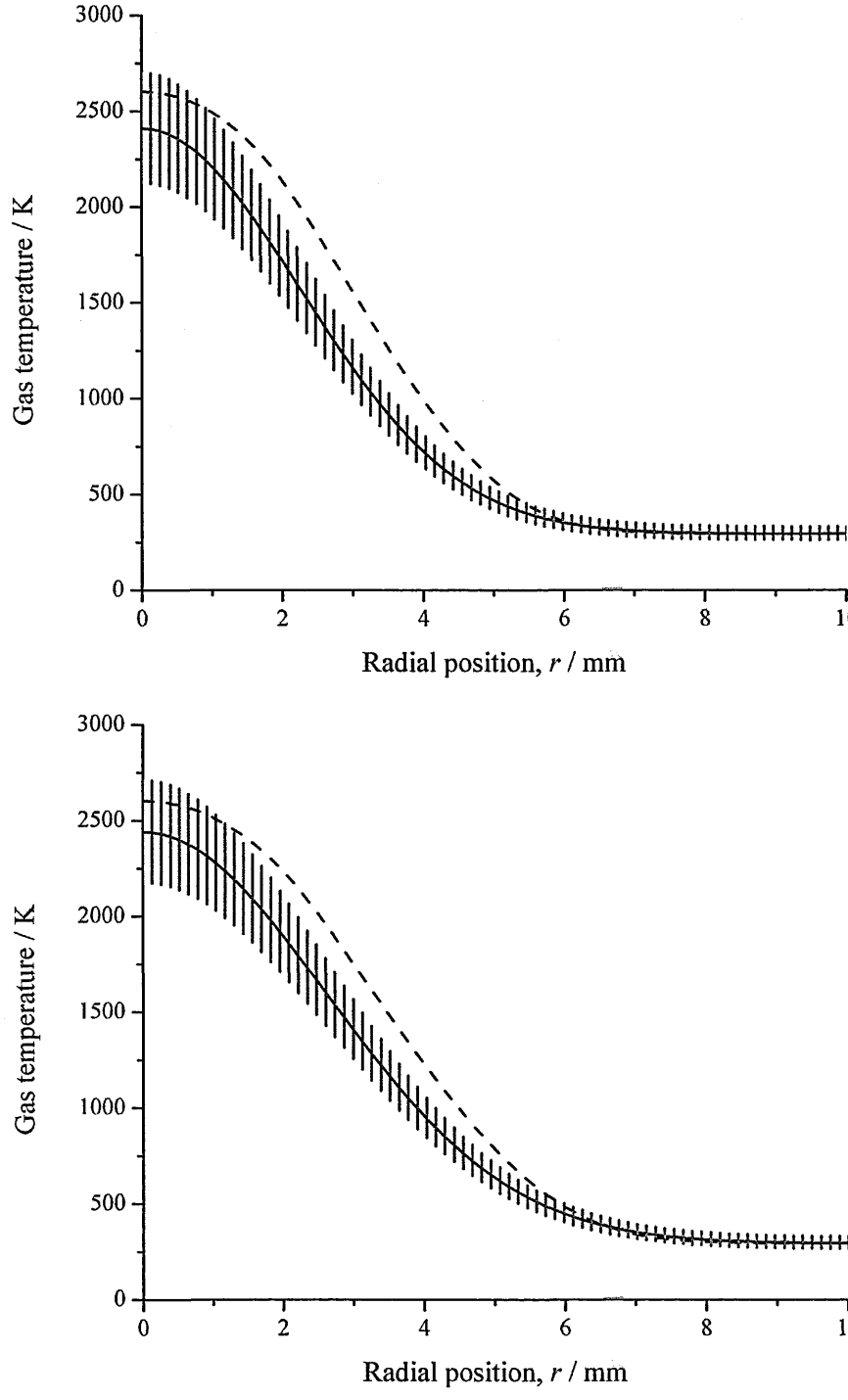

Figure 5.30: Radial (Schlieren) gas temperature (solid) and modelled gas temperature profile (dashed) at axial positions $z = 6$ mm (top) and 10 mm (bottom) and for an rms conduction current of 18 mA.

be approached with caution; a temperature modulation may not result in a proportional modulation in the number density and the gas may not be well modelled by the ideal gas law. What can be said is that changes in the *refractive index* will occur as a result of temperature, density and volume changes, but in a non-linear fashion over the modulating cycle. Hence, the results in the section are expressed in terms of the refractivity, $(n-1)$.

A 3 kHz modulation was applied to the plasma at a modulation depth of 33 % on the conduction current. This deep modulation (increased from 22 %) provides a suitable starting condition with which to determine whether modulation can be detected. Measurements were acquired over two periods relative to the frequency ($T = 0.33$ ms) and in steps of 40 μs. Based on the findings in the preliminary measurements and the potential difficulty in detecting modulation, two changes to the steady state analysis have been incorporated; firstly, the cutoff level was increased from 50 % to 85 % into the source image to increase the contrast sensitivity. This is regarded as a high cut-off level and for this plasma source, resulted in over-ranging where all the deflection angle profiles were assymetric. In these cases, the symmetry criteria used in the steady-state measurements was neglected with the unsaturated side of the profile analysed. Secondly, the fitting procedure has insufficient sensitivity with respect to the predicted refractivity variation. Choosing to use the Abel *reverse* transform accounts for the detailed structure along a deflection angle profile which may contain information regarding the modulation. The surface plots in figure 5.31 show the radial refractivity profile as a function of time for four axial positions. At $z = 0.5$ mm and 1 mm, $(n-1)$ is shown to vary at the axial position but, as presented, becomes less distinct further above the electrode. The contour plots show more clearly that modulation of $(n-1)$ occurs up to $z = 2$ mm. At positions higher up the axis, any distinct modulation of $(n-1)$ is not apparent and reflects the trend in rotational temperature when under modulation (section 4.4.3). In this region, the increased convection and flow processes disrupts or 'masks' the modulation. This should not imply that the modulation isn't there. The acoustic measurements in section 2.5.4 showed the SPL increases with the electrode separation so a contribution is made to the sound production mechanism

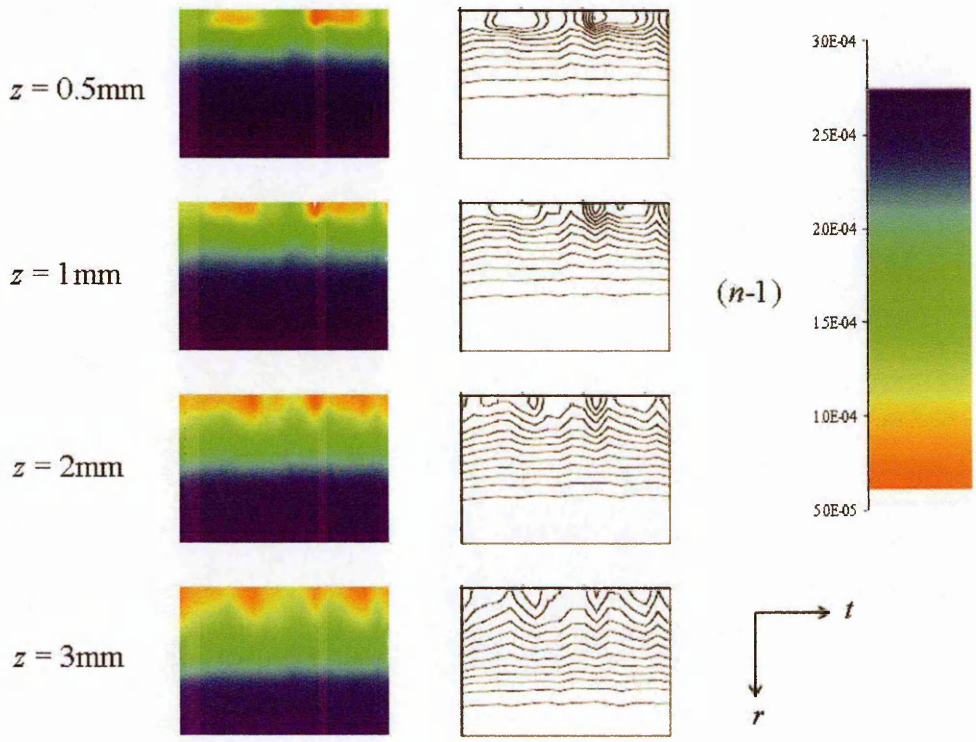

Figure 5.31: The time-varying radial refractivity profile for a 33% modulation depth on an rms conduction current of 18 mA; spatial dimensions, $r = 7.5$ mm, $t = 0.67$ ms.

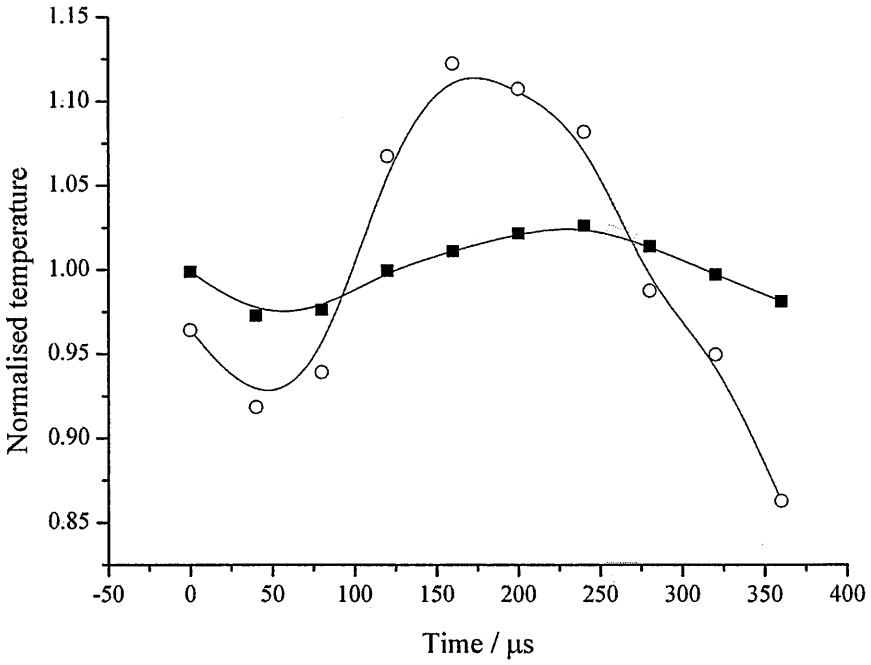

Figure 5.32: A comparison of the normalised rotational temperature (square) and gas temperature (circle) at $z = 0.5$ mm.

from the main body; it is just difficult to detect above the significant gas flow and cooling. The contour plot gives a spatial dimension to the modulation. At $z = 0.5$ mm, modulation of $(n-1)$ occurs within a radial distance of 1.5 mm and is coincident with the ionised channel. Beyond this distance, the constant spacing and position of the contour lines shows a region of steady state heating synonymous with heat conduction away from the central heated column. Hence it can be shown the dominant source of modulation, and hence the acoustic reproduction, lies in the ionised region with little contribution outside of this.

Finally, a qualitative measure of the relationship between the rotational temperature variation (derived through spectroscopy) and the gas temperature variation is made. For this, the on-axis value for the refractivity has been used to determine the gas temperature using the ideal gas law. The phase relationship between the peak gas temperature and the modulated rotational temperature is presented in figure 5.32. Although the gas temperature shows deviation from a sinusoid, many of the features such as the temperature minima show coincidence and that a negligible phase shift

indicates the close coupling between rotational and translational degrees of freedom as expected.

5.9 Summary

The dual-field lens schlieren system was developed to make a direct measurement of the translational gas temperature of the RF plasma. The system was calibrated against two thermal sources of known temperature. For the analysis, acceptance criteria were introduced to accomodate the assymetry in a deflection angle profile caused by variation of the plasma during measurement. The reliability of the algorithm used for the analysis was determined through known test functions. Overall, the system was found to be accurate to within $\pm$ 300 K. The peak rotational and gas temperature show significant deviations along the vertical axis. This is contrary to the expected close coupling between the two parameters. The gas temperature is closely coupled to the discharge radius both as a function of axial position, z, and of conduction current. This makes it likely that gas diffusion effects need to be accomodated in the previous assumption of R-T relaxation. The measured and modelled radial temperature profile follow each other closely and show the gas temperature to drop off to ambient at a distance $r >$ 6 mm. Under a 3 kHz modulation, the refractivity varies within a radial distance of 1.5 mm, around the central ionised channel. The modulation is evident around the electrode but is disrupted or masked further up the column due to convective flow within the plasma. The modulated rotational and gas temperatures are approximately in phase though the amplitudes of the variation differ by a factor of three.

Chapter 6

Overall conclusions and further work

The overall aim of this project was to understand the mechanism within a RF atmospheric pressure plasma that leads to acoustic emission. This was explored through a number of methods as reported in the experimental results chapters and their significance was discussed. The way in which the work progressed can be broken down into the following areas,

- establishing the plasma's capability as an acoustic emitter
- determining the characteristics of the steady plasma
- understanding the effects of modulating the plasma

In this chapter an overall summary and some final conclusions will be drawn based on the findings in these areas. In addition, ideas for extending the work further are suggested.

6.1 Acoustic characteristics

Initial investigations for this project were concerned with establishing the acoustic characteristics of the plasma. As discussed in the introductory chapter, there are difficulties in making comparisons of the SPL with other sources mainly due to the differences in the driving conditions used. What can be said is that the maximum measured SPL of 67 dB provides a sufficiently high level for use in a domestic environment. This is best compared to the sound emitted from a television which, when operated at an

average volume, has an SPL of approximately 55-60 dB at a distance of 1 m. The dependence of the SPL on the modulation depth of the current may provide one path to manipulating the level of emission of the source. However, the evaluation of the harmonic distortion presented in section 2.5.2 and the close coupling of the acoustic and current THD levels means this is likely to lead to increased distortion and loss of signal quality. An alternative method of increasing the level of sound would be manipulating the plasma size. Varying the electrode separation was also shown to influence the SPL as has been seen in other plasma sources and the development of larger area discharges may lead to a novel approach in design. In theory, applying modulation to an electrically generated discharge would produce acoustic emission to some degree and this need not be restricted to the sharp point electrode arrangements that have been explored previously. Microplasma arrays [67] may provide an alternative large area discharge source for use in sound generation. The construction of a large area array where a series of microplasmas act in phase may be the modern version of the multiple point electrodes array of Matzusawa and Bequin [6, 21]. Large area sources have the ability to extend the low frequency range. Similarly, the development of an optimised mechanical structure around the electrodes may enhance the low frequency emission.

A path that was not explored during this project but would benefit from further investigation is the higher frequency response, greater than 20 kHz and which would readily find an application in acoustic testing. A cost-effective method for testing the acoustics of a structure (such as a hall or arena) is to build a scale down model for testing in a laboratory. Scaling down of the structure's size would require the wavelength of the sound emitted by a source to also be scaled. The desired frequency range for an audio source would change to 200 Hz-200 kHz thus the low frequency limit asscoiated with the plasma source is less of an issue.

6.2 Measurement of the plasma

The main aim of the experimental work were to make direct measurements of the plasma itself, both spatially and temporally. This was achieved through a combina-

tion of spectroscopy, close-up imaging and schlieren imaging. The configuration of the monochromator allowed discrete measurements of the plasma temperatures (rotational and vibrational) to be obtained as a function of axial and radial position. The close-up imaging system complemented the spectroscopy by measuring the plasma characteristics in the visible range while extending the spatial range over which the plasma could be measured. A comparison of the spectroscopic and total light imaging highlights the differences in the plasma characteristics that were dependent on the spectral region used and would benefit from further investigation. Both spectroscopy and close-up imaging were able to identify spatial variations and builds on the work reported previously by Bequin [6] which provides the only other available reference.

The development of the schlieren system, which extends the spatial measurement range further still, showed potential in providing a simple method for determining of the refractive index changes in a plasma. The main issue during the development was the instability of the plasma. This led to large variations in the calculated temperature profiles from seemingly small instabilities in the original line-of-sight intensity profile from which it was calculated. This could be improved through further development to make the system capable of full tomographic imaging. An example of 3D schlieren imaging is given in Kaiser [68] where the constrictions and modes of a high pressure gas under modulation are imaged with a two camera system, oriented at 90^o to each other. Modifications can be made to the system used in this project to produce a similar effect. The simplest arrangement is leaving the optical system static and rotating the plasma which is equivalent to imaging at multiple orientations. A 3D tomographic image can be formed from rendering the acquired data and may improve on the errors generated through instability seen in the single axis measurements.

The schlieren imaging also highlighted the differences between the rotational and gas temperatures in the steady-state plasma, the cause of which should be addressed. It is generally assumed that the two parameters are in equilibrium for an atmospheric pressure, air plasma. However, in the studies where this has been reported, direct measurement of the gas temperature has not been completed and the equilbrium argument remains an assumption. The results for the schlieren system validation do not indicate

that the differences result from uncertainty in the instrumentation or the analysis. Similarly, there is no frame of reference available in the form of published literature with which to corroborate these results. Because of this, further investigation is required to confirm these source of these differences, either through an alternative measurement method or in re-evaluation of the nature of the plasma through wider discussion.

The main focus for this work was investigation of the nitrogen second positive system. Further investigations could look at other other features of the nitrogen spectrum including molecular bands and electronic states. Equally, the significance of other atomic and molecular species should be investigated. The spectral scans in figure 3.9 show multiple species being generated, the rates of which are strongly dependent on the conduction current and the target volume. Reference was made to the impact that changes in the rate constants for the vibrationally and rotationally excited nitrogen species has on the respective temperatures (section 3.4.4). The densities of other molecular species are dependent on all the rate constants and it would be useful to investigate to what extent these species are coupled with nitrogen.

Appropriate gating of the imaging device, in this case the Andor CCD camera used for all three optical measurement systems, provided a simple, controllable means of measuring temporal variation. The delays between the response of the species temperatures, optical intensities and discharge radii relative to the input electrical characteristics showed the dynamics of the plasma under modulation. While the delays are a strong indication of the time constants associated with various processes within the plasma, data presented here are currently limited to one frequency and a fuller understanding would be obtained through measurement at additional modulation frequencies. Discrepancies in the amplitude of the temperature variation exist which require more thorough investigation. For example, the modelled gas temperature shows significantly lower amplitude variation than the rotational temperature measured through spectroscopy. Similarly, the gas temperature modulation measured through schlieren is three times greater in amplitude than the rotational temperature. The differences between the model may at this stage be down to the model parameters themselves. It should be accepted that the Naidis model is in an early (but promising) stage of its

development and further work is required in conjunction with measurements to develop it more fully. The differences seen in the amplitudes between the schlieren and spectroscopic measurement systems are unexpected and imply more complicated behaviour in the nature of the energy transfer mechanism that would need to be more clearly defined.

However, temporal measurements provide some useful information on the dynamics of the plasma and could readily be incorporated into other measurement systems. For this work, one ready application would be the monitoring of the spectral emission. The steady-state spectral emission for two current settings was presented in section 3.4.2 was suggested in the reporting of the discharge radius that the species in lower UV wavelength region contributed to the visible emission. Monitoring the temporal variation over this wider spectral wavelength range will elucidate the interactions between plasma species. Further investigations into the relative phases between the input power and the species temperatures would confirm if the summary made regarding the significance of the time constants of the various plasma processes is correct.

Although spatial measurements of the plasma were achieved through optical emission, only global values for the electrical characteristics were obtained. Arguably, the most important of these are the electric field, E, and the electron number density, n_e, because of their dominant role in defining how the plasma is sustained. One method for localised electrical measurements was suggested in along with the section 3.4.4 based on the dependence of the vibrational temperature and the rate of excitation from electron impact.

6.3 Modelling

The comparison of the results from a numerical model with the experiments reported here have added an extra dimension in understanding the plasma behaviour. Previous attempts at modelling acoustically modulated plasmas have used a macroscopic approach with a number of assumptions for determining how the neutral gas molecules are heated. The Naidis model allowed a greater number of kinetic processes within the plasma to be included thus giving a more complete picture of the discharge behaviour

including N_2/O_2 chemistry. The main gas mechanism is joule heating leading to vibrational excitation of the dominant molecular nitrogen species. The close correlation between the modelled and measured species temperatures and discharge dimensions, for the steady-state and for the modulating plasma, indicates that these paths are the main drivers in gas heating. More work is required to account for the differences seen in the amplitude of the temperature modulations. The numerical model as it stands provides a reasonable starting point for development but the optimum goal would be coupling of the plasma variation to the acoustic signal directly.

Appendix A

Summary of the RF plasma characteristics

A summary of the plasma characteristics obtained through experiment is given in table A and apply to the discharge with a 15 mm electrode separation. Reference to other configurations (if available) can be found in the relevant section as given in the reference column.

Characteristic	Ref	Value	Detail
Driving frequency	2.2	325 kHz	
Breakdown voltage	2.3.1	25 kV_{p-p}	
Sustaining voltage	2.3.1	4-5 kV_{p-p}	
rms conduction current	2.3.1	11-30 mA	
capacitance between electrode	2.3.6	5 pF $\pm$ 0.2 pF	
SPL	2.5.2	67 dB @ 1m	f = 3 kHz, I_{rms} = 18 mA, mod. amplitude = 2.6 mA
Electron number density, n_e	3.4.1	2.4x$10^{17}m^3$	I_{rms} = 11mA
Discharge radius			
UV	3.4.3	0.75/0.8 mm	z = 6 mm
Visible		0.65/1.2 mm	I_{rms} = 11/27 mA
Vibrational temperature, T_v	3.4.4	4000K/2300K	z=0mm/6mm I_{rms} = 11mA,
Rotational temperature, T_r	3.4.4	2300K/3000K	z=0 mm/6mm I_{rms} = 11mA
Kinetic (gas) temperature	5.7	925K/2300K	z = 0 mm/6 mm I_{rms} = 18mA
Modulation efficiency	4.4.6	0.006 %	f = 3 kHz SPL = 75 dB

Table A.1: Summary of the plasma characteristics.

Appendix B

Andor DH534 iCCD camera corrections

The Andor DH534 iCCD camera used for all optical emission measurements in chapter 3-5 has a sensitivity that is dependent on the wavelength of light being imaged. This is most critical for the spectroscopic measurements where the light being imaged is wavelength specific and a correction is applied based on the response of the CCD using a light source of known emission. This response was assessed using an Ocean Optics LS-1 tungsten-halogen light source over the wavelength range 300-850 nm. The calibration of the light source is traceable to the National Institute for Science and Technology (NIST) and the calibration curve for the spectral output emission is given in figure B.1.

To measure the response of the Andor camera, the monochromator was set-up with the UV lens and mirror combination as described in section 3.3.1. The light source was positioned at a distance of 150 mm from the focussing lens in order to have a 1:1 image onto the monochromator entrance slit. The convolution of the calibration curve and the measured data produces the correction curve in figure B.2.

A correction was applied to all spectra acquired over the wavelength range of 362-382 nm that was used for determining the gas temperatures. For the wider spectral emission measurements given in section 3.4.2 the wavelength range extends down to 200 nm. For a correction in this region, the correction factor determined at 300 nm has been applied. While this does not reflect the absolute intensity, a relative assessment can still be made of the plasma species below 300 nm.

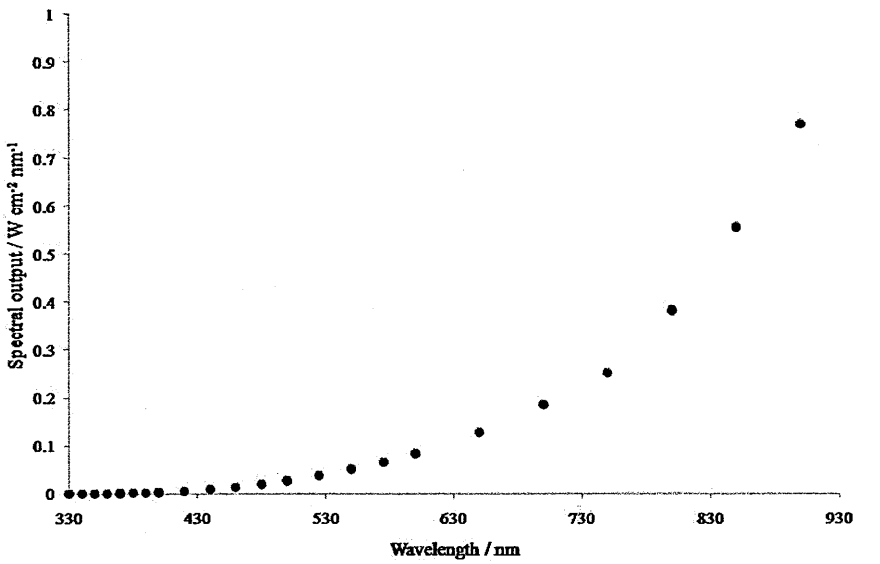

Figure B.1: Spectral response curve for the LS-1 light source.

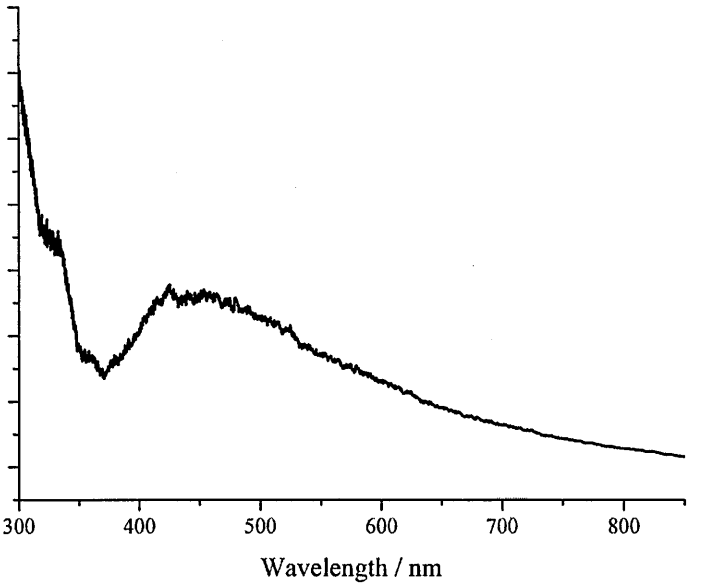

Figure B.2: The correction factor for the Andor camera

Appendix C

Systematic uncertainties budgets

The uncertainties derived from the measurements are presented in this appendix. To recall, the type B (systematic) uncertainty was derived from a combination of manufacturer's specifications, evaluation of the instrumentation and the methods used for data analysis. Unless stated, a rectangular probability distribution has been assumed with the combined, expanded uncertainty calculated to a 95 % confidence level [2].

C.1 Acoustic measurements

The acoustic uncertainties were evaluated in chapter 2 and the components are summarised in table C.1.

Source of uncertainty	Ref	value / ± dB	u_b / dB
Microphone/preamplifier response	2.4.3	1	0.58
Environmental effects	2.4.3	1	0.58
Calibration of source	2.4.3	1	0.58
Reflections/inteference effects	2.4.4	3	1.73
Combined standard uncertainty, u_c			2
Expanded uncertainty, U ($k = 1.65$)			3.3

Table C.1: Acoustic measurement uncertainty budget

C.2 Electrical characteristics

The electrical characteristics were presented in chapter 2 and a description and evaluation of the measurement uncertainties is given here.

C.2.1 Resistor tolerances

The total current (which includes both displacement and conduction current components) was determined from the voltage drop across a 100 Ω resistor connected in series to ground. The resistor had a tolerance of ± 1 % and was measured using a multimeter to be actually 99.8 Ω. The determination of the conduction current for the steady-state measurements requires the subtraction of the displacement current from the total current as described in section 2.3.1. Therefore, both measurement of the total and displacement current components will contribute to the uncertainty of the conduction current and adding the components in quadrature gives an uncertainty of ± 1.4 % of the current. For simplicity, the maximum current amplitude measured is 45 mA and a single uncertainty of 0.63 mA has been applied to all measurements.

C.2.2 Probe and oscilloscope uncertainty

The oscilloscope probe (used for the current), high voltage probe and the oscilloscope will all have a tolerance that is associated with the accuracy of their performance during measurement which can be determined from the manufacturer's specification. For the probes, the signficant effect is in teh accuracy of the attenuation which will affect how the amplitude of a voltage waveform is replicated. For the oscilloscope probe used for current measurement, an uncertainty of ± 2% is given and for the high voltage probe with a 1000:1 attenuation the uncertainty is ±3%.

The manufacturer's specification of the Tektronix 2014B oscilloscope is dependent on the range settings used on the oscilloscope. For a DC coupled input, the following tolerance is used; ± 3% of reading + 0.1 x division + 1 mV. Breaking this down, the range of driving voltages measured covers 4-5 kV_{p-p}. To encompass all the measurements, 3% of the maximum range value has been used an applied for all measurements and calculated to an uncertainty component of 150 V. For the voltage range measured,

a 1 kV/div provides sufficient resolution for measurement and an uncertainty of 100 V is also applied. Similarly, for the measured voltage used to derive the current, 2 V/div was the range used for acquisition. Based on a maximum rms conduction current of 30 mA, an uncerainty based on 3% of this value has been applied to all measurements along with and equivalent value of 2 mA for the oscilloscope resolution has been applied.

C.2.3 Overall budget

Source of uncertainty	Ref	value / ± unit	u_b / V	u_b / mA
Resistor tolerance	C.2.1	0.6 mA		0.4 mA
Probe accuracy	Spec	150 V 1.6 mA	87 V	0.9 mA
Oscilloscope accuracy	Spec	250 V 2.9 mA	144 V	1.7 mA
Combined standard uncertainty, u_c			168 V	2.0 mA
Expanded uncertainty, U (k = 1.65)			278 V	3.2 mA

Table C.2: Electrical uncertainty budget

Spec - Manufacturer's specification

C.3 Spectroscopy

The main source of uncertainty for the rotational and vibrational temperature results results from the analysis carried out using the MathCad algorithm. The description of the variable parameters of the algorithm and their impact on the temperature values is given in this section.

C.3.1 Upper and lower wavelength range

One of the user input parameters is the wavelength range over which the modelled spectrum is to be compared to that measured. Variations in the upper and lower wavelength limits that are defined required evaluation to assess the impact on the temperature results. A test spectrum obtained from measurement of the 0-2 band sequence was analysed and the values for the upper and lower wavelength limits varied;

the upper limit was kept constant at 382 nm and the lower limit varied between 362-376 nm. The standard random uncertainty (u_a) in the rotational and vibrational temperatures based on five sample data sets was ± 27 K and 6 K respectively and such a low value implies that the wavelength limits used for the 0-2 sequence have a negligible impact on the temperature. During analysis, the lower and upper limits were fixed at 362 and 382 nm respectively so as to maintain consistency in the analysis.

C.3.2 Wavelength region dependence

Accurate fitting to a measured spectrum requires low background levels from emission systems other than N_2SP. The 0-2 band transition was used for all measurements as this sequence was in a wavelength region where the interference from other emission systems is lowest. In practice, additional transition systems outside of N_2SP would require modelling in the same way as the N_2SP which was outside the scope of this project. To assess the calculation of the 0-2 band transition, a comparison was made of the rotational and vibrational temperatures evaluated from the 0-1 (around 357 nm) and 0-3 (around 400 nm) sequences to ensure consistency in the results with the 0-2 region used for measurement. The spread in the rotational temperature is approximately 340 K with the the average temperature for 0-2 sequence being 2895 K based on 5 sample measurements. The full extent of other transitions requires complete modelling of the band systems but as a precaution, the uncertainty has been derived from the results spread determined here.

C.3.3 Overall budget

Source of uncertainty	Ref	value / ± K	u_b / K
Upper/lower wavelength limit	C.3.1	27	16
Wavelength region	C.3.2	170	98
Differences to known algorithm (based on Tr=3000 K)	3.3.1	210	121
Combined standard uncertainty, u_c			157
Expanded uncertainty, U (k = 1.65)			258

Table C.3: Spectroscopy uncertainty budget

C.4 Schlieren imaging

The evaluation of the schlieren imaging was presented in chapter 5. A summary of the evaluated uncertainty are referenced and presented in table C.4.

Source of uncertainty	Ref	value/± K	u_b / K (FT)	u_b / K (RT)
Determination of cut-off width	5.3.3	100	58	58
Non-uniform cut-off	5.3.3	100	58	58
Optical component tolerances	5.3.5	100	58	58
Noisy data	5.4.4	25	14	14
Abel Inverse transform	5.4.4	150	-	87
Calibration differences (background)	5.5.1	50	29	29
Calibration differences (spatial)	5.5.1	50	29	29
Combined standard uncertainty, u_c			109	140
Expanded uncertainty, U ($k = 1.65$)			180	231

Table C.4: Schlieren uncertainty budget

FT - Abel forward transform

RT - Abel reverse transform

Appendix D

Description of the numerical model

The model validated against the experimental measurement was developed by Prof. George Naidis of the Institute for High Temperature, Moscow. A full description of the model is given here. The model describing stationary RF discharges stabilised by natural convection is analogous to that previously developed in [43, 44] for DC discharges. It is assumed that the discharge is vertical and axially symmetrical. Non-equilibrium effects, essential at low discharge current range considered in this work, are accounted for: deviation of the electron energy distribution from the Maxwellian one with the gas temperature, deviation of the vibrational distributions of molecules from the Boltzmann one with the gas temperature, and diffusion of plasma species. The distributions of plasma parameters along the radial (r) and axial (z) coordinates are governed by the system of equations involving Ohm's law, mass continuity equation and the axial and radial momentum balance equations as follows;

$$E(x) = \frac{I}{2\pi \int_0^R \sigma(x,r) r dr}, \tag{D.1}$$

$$\frac{\partial}{\partial x}(\rho u) + \frac{1}{r}\frac{\partial}{\partial r}(r\rho v) = 0, \tag{D.2}$$

$$\rho u \frac{\partial u}{\partial z} + \rho v \frac{\partial u}{\partial r} = -\frac{\partial p}{\partial z} - \rho g, \tag{D.3}$$

$$\rho u \frac{\partial v}{\partial z} + \rho v \frac{\partial v}{\partial r} = 0. \tag{D.4}$$

where $E(x)$ is the axial component of electric field at the distance, z, from the

bottom electrode, I is the conduction current, σ is the electrical conductivity (evaluated as $\sigma = en_e\mu_e$, where n_e and μ_e are the number density and mobility of electrons and e is the electron charge (it is assumed that the electrical conductivity does not change significantly over the RF cycle), ρ is the gas density, u and v are the axial and radial components of the gas velocity, p is the gas pressure, g is the gravitational acceleration. The model includes also the balance equations for the gas temperature, T, and for the mean vibrational energy of nitrogen molecules, $\varepsilon_{\rm V}$,

$$\rho u C_{\rm p}^* \frac{\partial T}{\partial z} + \rho v C_{\rm p}^* \frac{\partial T}{\partial r} = \eta_{\rm T}\sigma E^2 + Q_{\rm VT} + \frac{1}{r}\frac{\partial}{\partial r}\left(\chi^* r \frac{\partial T}{\partial r}\right), \tag{D.5}$$

$$n_{\rm N2} u \frac{\partial \varepsilon_{\rm V}}{\partial z} + n_{\rm N2} v \frac{\partial \varepsilon_{\rm V}}{\partial r} = \eta_{\rm V}\sigma E^2 - Q_{\rm VT} + \frac{1}{r}\frac{\partial}{\partial r}\left(n_{\rm N2} D_{\rm V} r \frac{\partial \varepsilon_{\rm V}}{\partial r}\right), \tag{D.6}$$

and the balance equations for the number densities, n_k, of various plasma components,

$$\frac{\partial}{\partial z}(n_{\rm k} u) + \frac{1}{r}\frac{\partial}{\partial r}(r n_{\rm k} v) = \frac{1}{r}\frac{\partial}{\partial r}\left(D_{\rm k} r \frac{\partial n_{\rm k}}{\partial r}\right) + F_{\rm k}. \tag{D.7}$$

Cp* andχ*are the corrected values of the specific heat and of the thermal conductivity, n_{N2} is the number density of nitrogen molecules, D_V is the diffusion coefficient of vibrationally excited N_2 molecules, η_T and η_V are the fractions of energy input transferred to gas heating and to vibrational excitation of N_2 molecules, D_k is the diffusion coefficient for species k (the ambipolar diffusion coefficient D_e is taken for electrons), the source term F_k describes the net rate of generation of species of kind k in the kinetic processes of ionization, dissociation, recombination, etc. The term Q_{VT} describes the vibrational-translational (V-T) relaxation of nitrogen molecules. Note that the mean vibrational energies of other molecular air components, O_2 and NO, are close to their equilibrium values at the gas temperature, due to fast V-T relaxation of these species. Thermal conduction and diffusion in axial direction is neglected owing to aspect ratio of the discharge column. No account is taken of heat losses to the electrodes and radiation losses are also neglected, as their role at low currents is small. The scheme and rate constants of kinetic processes (excluding those involving electrons), the diffusion coefficients, the factors η_T and η_V, and the rate of V-T relaxation are taken the same

as in [43]. The kinetic scheme includes processes with participation of N_2, O_2, N, O, NO, NO^+, O^-, O_2^-, O_3^-, and electrons. Balance equations are solved for the densities of N, O, NO and electrons. The densities of negative ions are evaluated in a local approximation (such approach is justified, because the times of destruction of negative ions in detachment processes are much less than the times of diffusion), the density of positive ions is obtained from the condition of conservation of charge, the densities of N_2 and O_2 are given by the condition of conservation of N and O nuclei. The rate constants of reactions with participation of electrons are obtained by averaging corresponding cross sections with the electron energy distribution function (EEDF). Note that for considered parameters of RF discharge the relation $\omega\delta\nu$ between the angular wave frequency, ω, and the collision frequency, ν, takes place, where ν is the mean fraction of electron energy lost in a collision of an electron with a heavy particle. In such conditions, the EEDF follows the periodic change of the electromagnetic field, and the averaging of the rate constants of reactions involving electrons over the wave period is required. Assuming that the dependence of a rate constant, K, on the instant value of the reduced electric field, E/n (here n is the gas number density) may be taken in the form $Kexp(-Bn/E)$ typical for processes with high energy thresholds (ionization, electronic excitation, dissociation), one obtains approximate expression for the time-averaged rate constant $<K> = K_{amp}(2E_{amp}/\pi Bn)^{1/2}$ [45], where E_{amp} is the amplitude of electric field and K_{amp} is the corresponding value of the rate constant.

Bibliography

[1] A.B.Coppens L.E.Kinsler, A.R.Frey and J.V.Sanders. *Fundamentals of Acoustics.* John Wiley and Sons Inc., 4th edition, 2000.

[2] Joint Committee for Guides in Metrology – Working group 1 (JCGM/WG1). *Evaluation of measurement data - A guide to the expression of uncertainty in measurement (GUM).* JCGM 100:2008.

[3] G. Shirley. The Corona wind loudspeaker. *Journal of the Audio Engineering Society*, 5(1):23–31, 1957.

[4] M.K. Lim. A Corona-type point source for model studies in acoustics. *Applied Acoustics*, 14(4):245–252, 1981.

[5] M.S. Mazzolla and G.M. Molen. Modeling of a DC glow plasma loudspeaker. *Journal of the Acoustical Society of America*, 81(6):1972–1978, 1987.

[6] P. Bequin and P. Herzog. Model of acoustic sources related to negative point-to-plane discharges in ambient air. *Acustica*, 83(2):359–366, 1997.

[7] William Du Bois Duddell. Improvements in oscillographs or apparatus for indicating, or recording, rapidly varying electric current of potential differences. *The Patent Office, London*, (Application no. GB189805449), 1898.

[8] William Du Bois Duddell. A new or improved instrument for measuring direct of alternating electric currents and potential differences. *The Patent Office, London*, (Application no. GB190017642), 1901.

[9] W. Duddell. Some experimentals on the direct current arc. *Nature*, 63(1625):182–183, 1900.

[10] S. Klein. Un nouveau traducteur electroacoustique: l'Ionophone. *Acustica*, 4:77–79, 1954.

[11] S. Klein. Improvements in and relating to transducers. *The Patent Office, London*, Patent specification: 756546, 1952.

[12] S. Klein. Sound emitter. *United States Patent office*, Patent specification: 4,306,120, 1981.

[13] S. Klein. Corona-effect sound emitter. *United States Patent office*, Patent specification: 4,464,544, 1984.

[14] S. Klein. Transducers for the transformation of electrical modulations into vibratory modulations. *United States Patent office*, Patent specification: 4,482,788, 1984.

[15] Villanova University. The Corona-phone - a solid state, FET based Ion Tweeter. *www.ee.vill.edu/ion/index.html*, 2002.

[16] A.E. Hill. Plasma loudspeaker. *United Kingdom patent application*, Patent specification: GB2023373, 1979.

[17] Acapella. Ionic tweeter T1WS. *http://www.acapella.de*, 2011.

[18] F. Bastien. Acoustics and gas discharges: applications to loudspeakers. *Journal of Physics D: Applied Physics*, 20(12):1547–1557, 1987.

[19] D.M. Tombs. Corona wind loudspeaker. *Nature*, 176:923, 1955.

[20] A. Anthony E. Ackerman and F. Oda. Corona-type loudspeaker for animal studies. *Journal of the Acoustical Society of America*, 33(12):1708–1712, 1961.

[21] K. Matsuzawa. Sound sources with corona discharges. *Journal of the Acoustical Society of America*, 54(2):494–498, 1973.

[22] V. Montembault P. Bequin and P. Herzog. Modelling of a negative point-to-plane corona loudspeaker. *European Physical journal: Applied Physics*, 15(1):57–67, 2001.

[23] P. Herzog P. Bequin, K. Castor and V. Montembault. Modeling plasma loudspeakers. *Journal of the Acoustic Society of America*, 121(4):1960–1970, 2007.

[24] F.J. Fransson and E.V. Jansson. The STL-Ionophone: Transducer properties and construction. *Journal of the Acoustical Society of America*, 58(4):910–915, 1975.

[25] K.L. Baker W.R. Babcock and A.G. Cattaneo. Musical flames. *Journal of the Acoustical Society of America*, 43(6):1465–1466, 1968.

[26] J.K. Burchard. Preliminary investigation of the electrothermal loudspeaker. *Combustion and flame*, 13(1):82–86, 1969.

[27] M. Fitaire and D. Sinitean. Acoustic wave excitation in a flame. *Czech Journal of Physics B*, 22(5):394–397, 1971.

[28] U. Ingard. Acoustic wave generation and amplification in a plasma. *Physical Review*, 145(1):45, 1966.

[29] P. Morse and U. Ingard. *Theoretical Acoustics.* Princeton University Press, 1st edition, 1987.

[30] Richie Burnett. Solid-state Tesla coil. *www.richieburnett.co.uk/tesla.shtml.*

[31] E.E. Kunhardt. Generation of large volume, atmospheric pressure, non-equilibirum plasmas. *IEEE Trans. Plasma Science*, 28(1):189–200, 2000.

[32] Y. Raizer. *Gas discharge physics.* Springer-Verlag, 2nd edition, 1987.

[33] P. Horowitz and W. Hill. *The Art of Electronics.* Cambridge University Press, 3rd edition, 1989.

[34] Correspondence with Bowers & Wilkins ltd.

[35] P. Fauchais M.I. Boulos and E. Pfender. *Thermal Plasmas: Fundamentals and applications*, volume 1. Springer, 1st edition, 1994.

[36] G. Billing and L. Wang. Semi-classical calculations of transport coefficients and rotational relaxation of nitrogen at high temperatures. *J. Phys. Chem.*, 96(6):2572–2575, 1992.

[37] D.M. Packan L. Yu, C.O. Laux and C.H. Kruger. Direct-current glow discharges in atmospheric pressure air plasmas. *Journal of applied physics*, 91(5):2678–2686, 2001.

[38] G. Herzberg. *Molecular spectra and molecular structure*, volume 1. Krieger Publishing Company, 2nd edition, 1989.

[39] A. Lofthus and P. H. Krupenie. Spectrum of molecular nitrogen. *Journal of Physical Chemistry*, 6(1):113–307, 1977.

[40] G. Hartmann and P.C. Johnson. Measurements of relative transition probabilities and variation of electronic transition moment for nitrogen second positive system. *Journal of Physics B - Molecular and Optical Physics*, 11(9):1597, 1978.

[41] J Andreasson C.O. Laux and J. Risberg. Specair v2.2. *www.specair-radiation.net.*

[42] Correspondence with K. Niemi, Queens University, Belfast.

[43] G.V. Naidis. Simulation of convection-stabilized low-current glow and arc discharges in atmospheric-pressure air. *Plasma Sources, Science and Technology*, 16(2):297, 2007.

[44] M.S. Benilov and G.V. Naidis. Modelling of low-current discharges in atmospheric-pressure air taking account of non-equilibrium effects. *Journal of Physics D: Applied Physics*, 36(15):1834, 2003.

[45] A.Kh. Mnatsakanyan and G.V. Naidis. Charged particle production and loss processes in nitrogen-oxygen plasmas. *Reviews of Plasma Chemistry Vol. 1*, 1:259, 1991.

[46] SMT359 Course team. *Electromagnetism - an introduction to Maxwell's equations*, volume Book 1 of *SMT359*. The Open University, 2006.

[47] N.S. Braithwaite. Introduction to gas discharges. *Plasma Sources, Science and Technology*, 9(4):517–527, 2000.

[48] Nist Atomic Spectra database v4. *National Institute for Standards and Technology*, 2010.

[49] C.O. Laux Z. Machala, E. Marode and C.H. Kruger. DC glow discharges in atmospheric pressure air. *J. Adv. Oxid. Technol.*, 7(2):133–137, 2004.

[50] A. Gutsol D. Staack, B. Farouk and A.A. Fridman. DC normal glow discharges in atmospheric pressure atomic and molecular gases. *Plasma Sources, Science and Technology*, 17(2):1–13, 2008.

[51] C.H. Kruger C.O. Laux, T.G. Spence and R.N. Zare. Optical diagnostics of atmospheric pressure air plasmas. *Plasma Sources, Science and Technology*, 12(2):125–138, 2003.

[52] A.N. Wright and C.A. Winkler. *Active Nitrogen.* Academic Press, 1968.

[53] X. Duten D.M. Packan L. Yu Z. Machala, C.O. Laux and C.H. Kruger. Scaled up non-equilibirum, air plasmas. *41st Aerospace Sciences meeting and exhibit, Reno, Nevada*, AIAA 2003:874, 2003.

[54] A. Fridman. *Plasma Chemistry.* Cambridge University press, 1st edition.

[55] A.F. Gutsol D. Staack, B. Farouk and A.A. Fridman. Spectroscopic studies and rotational and vibrational temperature measurements of atmospheric pressure normal glow plasma discharges in air. *Plasma Sources, Science and Technology*, 15(4):818–827, 2006.

[56] S.K. Pogrebnya I.K. Dmitrieva and P.I. Porshnev. V-T and V-V rate constants for energy transfer in diatomics. An accurate analytical approximation. *Chemical Physics*, 142(1):25–33, 1990.

[57] Health and Safety Executive. *Workplace Exposure limits.* Number Document EH40/2005. Health and Safety executive, 2005.

[58] K. Hensel I. Jedlovsky L. Lestinska V. Foltin V. Matinsovits Z. Machala, M. Janda and M. Morvova. Emission spectroscopy of atmospheric pressure plasmas for bio-medical and environmental applications. *Journal of Molecular Spectroscopy*, 243:194–201, 2007.

[59] A. Ichimura K. Onda K. Sakimoto K. Takayanagi M. Nakamura H. Nishimura Y. Itikawa, M. Hayashi and T. Takayanagi. Cross-sections for collisions of electrons and photons with nitrogen molecules. *Journal ofPhysical Chemistry*, 15(3):985–1010, 1986.

[60] G.S. Settles. *Schlieren and shadowgraph techniques: Visualising phenomena in transparent media.* Springer-Verlag, 1st edition, 2006.

[61] D.A.Feikama. Quantitative rainbow Schlieren deflectometry as a temperature diagnostic for nonsooting spherical flames. *Applied Optics*, 20(20):4826–4832, 2006.

[62] B. Mancinelli L. Prevosto, G. Artana and H. Kelly. Schlieren technique applied to the arc temperature measurement in a high energy density cutting torch. *Journal of Applied Physics*, 107(2), 2010.

[63] B. W. Albers and A. K. Agrawal. Schlieren analysis of an oscillating gas-jet diffusion flame. *Combustion and flame*, 119(1-2):84–94, 1999.

[64] R. Viladrosa J. Glasser and J. Chapelle. Diagnostic of dense plasmas by infrared schlieren and absorption techniques. *Journal of applied physics D: Applied physics*, 11(12):1703–1707, 1978.

[65] F.J. Weinberg. *Optics of flames.* Butterworths and Co., 1st edition, 1963.

[66] Adiabatic flame temperature. *Wikipedia*, 2011.

[67] K.H. Schoenbach K.H. Becker and J.G. Eden. Microplasmas and applications. *Journal of Physics D: Applied Physics*, 39(3):R55–R70, 2006.

[68] R.P. Marques W. Kaiser and A.F. Correa. An alternative optical method for acoustic resonance detection in hid lamps. *IEEE transactions on industry applications*, 47(3):1142–1148, 2011.